UNIVERSITY OF BIRMINGHAM

Nanostructured Graphite/Li-N-H based Composite Materials for Hydrogen Storage

by

Yinghui Li

A thesis submitted to the University of Birmingham for the degree of Master of Research (MRes)

School of Metallurgy and Materials

College of Engineering and Physical Science

University of Birmingham

United Kingdom

September 2014

Abstract

Ball-milled hydrogenated graphite and $LiNH_2$+LiH are considered potential materials for solid state hydrogen storage. The aim of this thesis was to investigate the use of ball-milled graphite+$LiNH_2$+LiH composites as a potential hydrogen storage material. This work investigates the structural and dehydrogenation properties of ball-milled graphite and composites of 2graphite+$LiNH_2$, $LiNH_2$+1.2LiH and 2graphite+$LiNH_2$+1.2LiH. Graphite was ball-milled under 3 bar H_2 for 8 h (180 rpm and 280 rpm were performed) and 10 h (280 rpm). 8 h-milled graphite was further milled with $LiNH_2$ at a molar ratio of 2:1 (graphite: $LiNH_2$) for 2 h. $LiNH_2$ and LiH were milled under 1 bar Ar for 3 h and 5 h, followed by the addition of graphite at a molar ratio of 2:1 (graphite: as-milled powder) and milled for a further 2 h. Characterization of the as-milled materials showed the formation of a nanocrystalline/amorphous mixture in the composites. A higher ball-milling rotation speed led to a smaller crystallite size for graphite.

Decomposition of the as-milled graphite was performed by heating to 950 °C at 2 ° C /min. Graphite milled for 10 h released 2.2 wt. % H_2 at onset temperature of 350 °C, indicates the presence of C-H bond in the hydrogenated graphite. A large amount of H_2 was released during the heating of graphite+$LiNH_2$, as opposed to the release of NH_3 during the decomposition of as-received $LiNH_2$. A sharp endothermic DSC peak at 365 °C indicates a reaction between graphite and $LiNH_2$. $LiNH_2$+1.2LiH was heated to 400 °C at 2 °C /min, and only H_2 was detected, with no NH_3 or NH_2. In-situ XRD shows that Li_2NH formed during the decomposition of the composite, but the detailed reactions are unclear.

Dehydrogenation of 2graphite+$LiNH_2$+1.2LiH was performed by heating to 500 °C at 2 °C /min. The onset temperature of hydrogen decomposition was reduced to 80 °C-95 °C. Four hydrogen decomposition peaks appeared at 150 °C, 240 °C, 350 °C and 450 °C, four broad endothermic DSC peaks were also observed. In-situ XRD shows the presence of Li_2NCN above 350 °C, with no Li_2C_2 or Li_2NH detected. The formation pathway of this new phase is not clear, but it presumably must involve a reaction between graphite and a Li-N-H compound. The reactions below 350 °C are believed to be due to $LiNH_2$ and LiH, but those above 350 °C are still unclear. As the toxic compound Li_2NCN forms after the dehydrogenation of graphite+$LiNH_2$+LiH, its use as a potential hydrogen storage material should be carefully considered.

Acknowledgments

I would like to give my sincere thanks to my parents for their endless love and support. Their understanding encouraged me a lot when I decided to study abroad, which is a big change in my life.

Many thanks to Sheng Guo, Joshua Vines, Luke Hughes, Naser Al-Mufachi, Shahrouz Nayebossadri and Simon Cannon, I have learned a lot and spent a nice time by their generous and kind-hearted help during my study in Hydrogen Storage Materials Research Group.

I would also like to give my thanks to Dr Daniel Reed, for his advice and help with equipment during my project.

Finally, I am particularly grateful to my supervisor Prof David Book, for his valuable guidance and advice to my research. Whenever I got problems in project or personal life, he was always ready to provide support and help.

Contents

1 Introduction

1.1 Hydrogen as a fuel in future energy economy

Hydrogen is the most abundant element in the universe, and there is a significant amount of hydrogen on the earth's surface in the form of water and various hydrocarbons. Hydrogen can be produced from water by electrolysis, but a significant energy input is required. The reformation of hydrocarbons (Inc. fossil fuels) can generate hydrogen; however the output gases often include CO_2.

Hydrogen can be an efficient and clean energy alternative in the future energy market for it goes through a reaction with oxygen without any greenhouse gas emissions (2 H_2 (g) +O_2 (g) =2 H_2O (g)). In terms of hydrogen as a fuel, hydrogen production, hydrogen storage and hydrogen distribution are three main fields to develop and research (Edwards, Kuznetsov et al. 2007). And the biggest technical challenge for transportation applications is hydrogen storage (Graetz 2009).

1.2 Hydrogen storage

1.2.1 Gaseous storage

Compressed hydrogen storage is one of the conventional ways in current hydrogen industry. High pressure (700 bar) is required for storing hydrogen as a gas (O'Malley, Ordaz et al. 2014). This requires the materials of the tanks to have a very high tensile strength, a low density and to not react with hydrogen or let hydrogen diffuse into it (Nellis 2006). In terms of the hydrogen density, for compressed hydrogen, the volumetric hydrogen density increases with pressure, while the gravimetric hydrogen

density decreases with increasing pressure. That means the increase of volumetric density is sacrificed with the reduction of gravimetric density in compressed gas systems. The gravimetric density decreases with increasing pressure due to the increasing thickness of the walls of the cylinder. And the equation (cylinder capped with two hemispheres) is as

follows (Züttel 2004):

$$\frac{d_w}{d_o} = \frac{\Delta p}{2\ _v + \Delta p}$$

Where d_w is the wall thickness, d_o is the outer diameter of the cylinder, Δp is the overpressure and $_v$ is the tensile strength of the material.

In future investment, material with higher tensile strength is to be developed. And these days, a new kind of high pressure vessel is developed which may store 110 kg at 70 MPa with a gravimetric density of 6 wt. % and 30 kg/m^3 volumetric densities. This kind of high pressure vessel contains three layers: an inner polymer liner (a hydrogen gas permeation barrier), over-wrapped with carbon-fiber composite (the gas pressure load-bearing component of the tank), and an outer layer of an aramid material capable of impact and damage resistance (Züttel 2004).

As reported, the costs for a 700 bar compressed H_2 systems are $17 /kWh, carbon fiber and components of the equipment accounting for over 90% of the cost (Ahluwalia 2013). This is much higher than the ultimate cost target of DOE ($8 /kWh) (Ordaz 2013).

1.2.2 Liquid storage

The energy density of hydrogen can be improved by storing hydrogen in a liquid state. The volumetric capacity of liquid hydrogen is 0.070 kg/L, compared to 0.030 kg/L for 70 MPa gas tanks (Felderhoff, Weidenthaler et al. 2007). Liquid hydrogen is stored in cryogenic tanks at 21.2 K at ambient pressure (Zuttel 2004). The simplest liquefaction cycle is the Joule-Thompson cycle (Linde cycle). During this liquefaction cycle, the LH_2 is produced by circulatory processes of cooling and compression. An isenthalpic Joule-Thomson expansion occurs when the gas passes through a throttle valve, and some liquid can be produced (Züttel 2003).

However, the energy requirement for hydrogen liquefaction is very high; typically, 35% of the heating value of hydrogen is required for liquefaction (Durbin and Malardier-Jugroot 2013). Boil-off is also a problem which would lead to cost losses. It is very easy for LH_2 to evaporate when it absorbs heat from the environment during delivery and refueling (Zuttel 2004, Durbin and Malardier-Jugroot 2013).

Recently, cryocompressed hydrogen was considered to be a potential hydrogen storage technology. Some practicable pressure vessels were produced in labs. The one made by Toyota Prius reported that it may store 5.5 wt. % of hydrogen with a volumetric capacity of 41.8 g-H_2/L (Ahluwalia, Hua et al. 2010). However, $12/kWh for manufacturing is quite expensive for large-scale production. The efficiency of this tank (41.4%) is also lower than the DOE target of 60%.

1.2.3 Materials-based hydrogen storage

1.2.3.1 Metal hydrides

Hydrogen can react with many transition metals and their related alloys to form hydrides at relatively high temperature. There are two possible methods to form metal hydrides: direct dissociative chemisorption and electrochemical splitting of water (Sakintuna, Lamari-Darkrim et al. 2007). Compare with compressed hydrogen and liquid hydrogen storage methods, metal hydrides can be a very effective way to store large amounts of hydrogen in a safe and compact way. Because the formation process of metal hydrides is under moderate temperature and pressure.

MgH_2 is one of the most popular metal hydrides in research. Its theoretical gravimetric density of hydrogen storage can be over 7 wt. % with the benefit of low cost and good reversibility (Zaluska, Zaluski et al. 2001, Grochala and Edwards 2004). But there are also some disadvantages of MgH_2, such as high temperature of dehydrogenation process, slow desorption kinetics and sensitive with air and O_2 (Grochala and Edwards 2004, Imamura, Masanari et al. 2005).

1.2.3.2 Complex hydrides

The main difference between complex hydrides and metal hydrides is the transition to an ionic or covalent compound upon hydrogen absorption (Züttel 2003). The light weight group 1, 2 and 3 metals such as Li, Mg, B, Al give rise to a large variety of metal-hydrogen complexes (Shashikala 2012). Hydrogen in complex hydrides is often located at the corners of a tetrahedron with B or Al in the centre (Züttel 2003).

Hydrides complexes of borane, $M(BH_4)$, and $M(AlH_4)$ are found to be stable and can decompose at elevated temperature (often above the melting point of the complex) (Züttel 2004). $NaAlH_4$ is one of the most popular material, which can reversibly absorb and desorbs up to 4.2 wt. % hydrogen when it was mixed with 8 mol% CNT (Pukazhselvan, Gupta et al. 2005). The highest gravimetric hydrogen density at RT today is $LiBH_4$ (18 wt. %), which desorbs 3 of the 4 hydrogens in the compound upon melting at 280 $^{\circ}$C, to form LiH and B (Orimo, Nakamori et al. 2007, Shashikala 2012).

Due to their high gravimetric hydrogen density and volumetric hydrogen density, the borohydrides will attract more focus in future research.

1.2.3.3 Storage via chemical reactions

Hydrogen can be generated by reaction of metals and chemical compounds with water. For example, Zn can react with H_2O to form H_2 and ZnO. However, the poor reversibility is a big challenge of this method (Steinfeld 2002).

1.2.3.4 Nanostructured materials

It is found that the carbon-based media is a kind of potentially inexpensive hydrogen storage material. Substantial amounts of hydrogen can be stored on high surface area (up to 3000 m^2/g) activated carbons via physisorption, however, low temperatures (~ 77 K) are required for this to take place. Graphite with a typical interlayer distance of around 0.34 nm is believed to be too short to absorb hydrogen

molecules. However, nanostructured graphite with 0.6-0.75 nm interlayer spacing has been proposed, via simulations, to potentially absorb up to 6 wt. % hydrogen (200 K, 500 bar) (Patchkovskii, Tse et al. 2005). Ball milling was reported to be an effective method of producing nanostructured hydrogenated graphite: ball-milling under 10 bar hydrogen for 80 h resulted in the absorption of 7.4 wt. % hydrogen (Orimo, Majer et al. 1999).

2 Literature Review

2.1 Carbon as a hydrogen storage material

Due to the increasing demand for fuel cells, the development of hydrogen storage materials is now necessary. The current hydrogen storage materials such as Al-H or Mg-H have quite high hydrogen storage capacity, but they all have their own barriers (such as difficult synthesis process or high temperature for dehydrogenation), may be not suitable for the practical manufacture and application. Carbon which is light and can be supplied by industrial production was found to be a potential hydrogen storage material (Dillon and Heben 2001). However, carbon on its own can only store hydrogen by a physisorption mechanism, and consequently the storage capacity is limited under practical conditions (such as temperature and pressure). There are four kinds of carbon materials which are activated carbon, graphene, carbon nanostructures and graphite.

2.1.1 Mechanisms

i. Physisorption

Physisorption is an interaction between the substrate and the sorbate based on van der Waals effects. During the process, the gas molecules are attracted to the substrate surface by van der Waals attractive forces, but there is also a minimum distance due to the van der Waals repulsive force. The minimum energy required to keep the equilibrium of gas attraction and repulsion is 1-10 kJ mol^{-1}(Ströbel, Garche et al. 2006).

Due to the weak van der Waals attractive forces, there is a limit on the ratio of C to H atoms. To estimate the maximum quantity of hydrogen adsorbed on the surface of a

solid, hydrogen molecules can be considered as adsorbing as a monolayer(Züttel 2003), the theoretical surface area of carbon to adsorb 6 wt. % hydrogen (2010 DOE target) is over 2600 m^2 g^{-1} (Ströbel, Garche et al. 2006).

ii. Chemisorption

Chemisorbed hydrogen with a strong C-H covalent bonding may increase the density of packed hydrogen (Niemann, Srinivasan et al. 2008). It was found that hydrogen molecules can react with graphite to form the dangling carbon bond by ball milling under hydrogen atmosphere (Orimo, Majer et al. 1999). In chemisorption, each carbon atom can be a site for one hydrogen atom to form a C-H bonding (Henderson, McMichael Rohlfing et al. 1993).

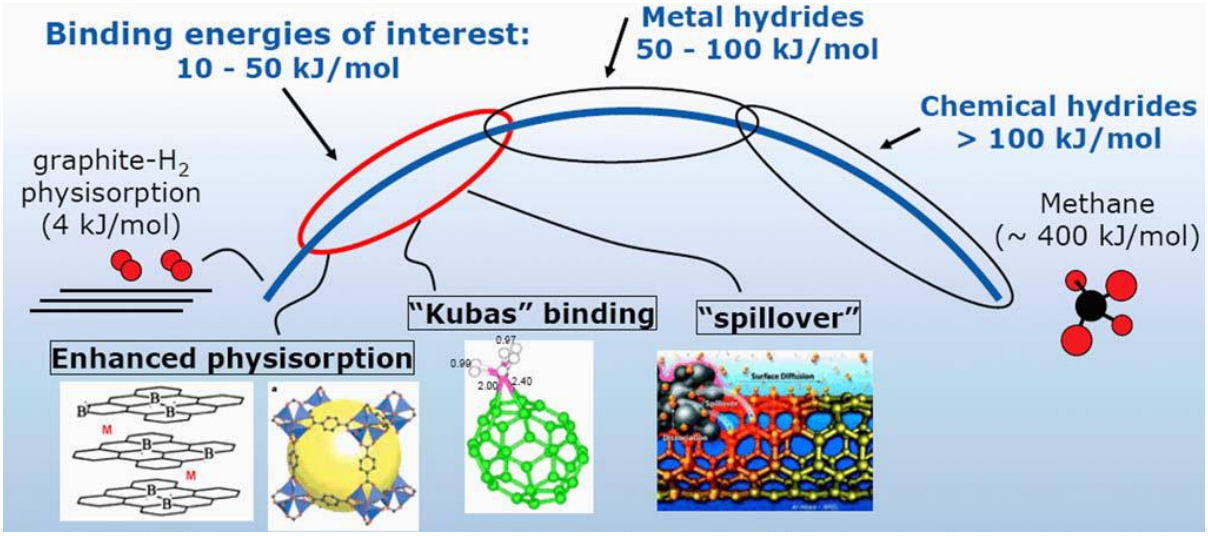

Figure 2.1 Different binding energies of different hydrogen storage materials (Ströbel, Garche et al. 2006).

The C-H covalent bonding formed as a result of chemisorption is much stronger than van der Waals forces from physisorption, which means that a higher temperature is needed to release the chemisorbed hydrogen. Figure 2.1 gives a summary of the binding energies of different hydrogen storage methods. It can be seen that chemical

hydrides (>100 kJ mol^{-1}) and methane (400 kJ mol^{-1}) have high enthalpies, which require higher temperatures for hydrogen desorption

2.1.2 Activated carbon

Activated carbon is a kind of carbon material which contains graphite crystallites and amorphous carbon, modified from synthetic carbon (Ströbel, Garche et al. 2006). The precursors of activated carbon are carbonized organic precursors which are treated by dry distillation, and then activated by a thermal method (700-1000 $^{\circ}C$ in oxygen-rich gases) or chemical method (500-800 $^{\circ}C$ with the existence of dehydrated material, e.g. NaOH, KOH) (H. Marsh 2005, Ströbel, Garche et al. 2006).

Physisorption is the main hydrogen storage mechanism for activated carbon. This indicates that the hydrogen storage capacity of activated carbon is related to the micropore volume of the material. However, only a small amount of hydrogen was found to be stored in activated carbon at room temperature and moderate pressure. (Ströbel, Garche et al. 2006)

2.1.3 Carbon nanotubes (CNTs)

Carbon nanotubes were discovered by (Iijima. 1991), and are believed to have applications for electronic, catalytic action, hydrogen storage (Tan, Tan et al. 2012). Single-wall nanotubes (SWNT) can be considered as a rolled-up single layer of graphene (Fig 2.2) while multi-wall nanotubes (MWNT) are formed from rolling-up multiple layers. Normally, the diameter of a SWNT is around 2-5 nm (Roy 2012), and

MWNT have inner and outer diameters which are around 1.5-15 nm and 2.5-30 nm, respectively (Ströbel, Garche et al. 2006).

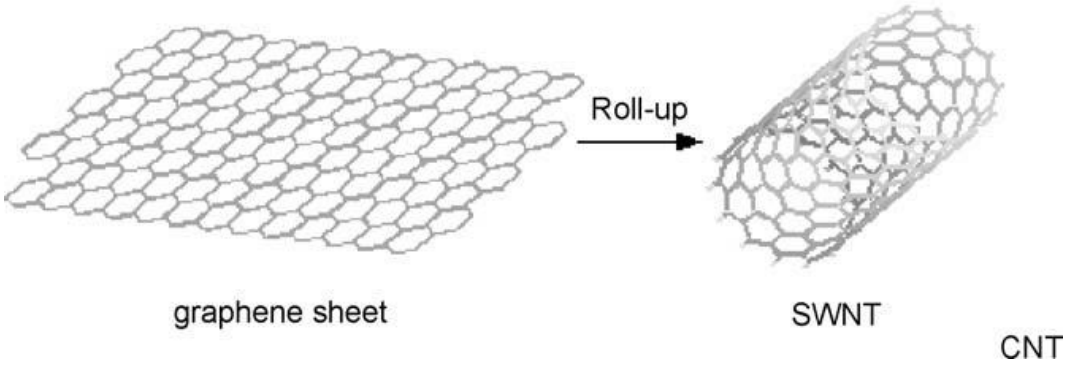

Fig 2.2 Schematic of the structure of a carbon nanotube (although note that the nanotube cannot actually be prepared by 'rolling up' a graphene sheet). (Ströbel, Garche et al. 2006)

According to the different synthesis techniques used (Roy 2012) for the formation of SWNTs, there are three different modalities (Fig 2.3): armchair, zigzag and chiral.

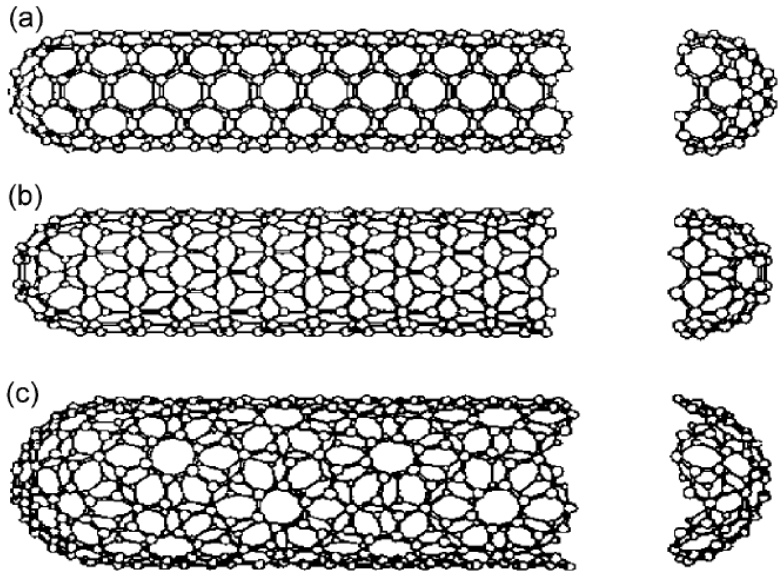

Fig 2.3 Three different SWNT structures: (a) armchair; (b) zigzag; (c) chiral (M. S. DRESSELHAUS 1995).

As potential hydrogen storage media, CNTs were considered to absorb hydrogen through physisorption and chemisorption (irreversible (Barghi, Tsotsis et al. 2014)). In physisorption, hydrogen is stored in the inner space of the tube via Van der Waals forces, and in chemisorption hydrogen can be adsorbed on the outer surface or the inner surface of the metal-doped carbon nanotubes(e.g. Li-doped CNTs or K-doped CNTs) via chemical bonding (Chen, Wu et al. 1999, Darkrim, Malbrunot et al. 2002).

The hydrogen storage capacity data of CNTs were summarized by Ströbel, Garche et al.in 2006, in which it shows that the high purity SWNT may absorb 8 wt. % hydrogen at 80 K under a pressure of 7 MPa (Y. Ye 1999), and high purity MWNT with acid treatment may absorb 13.8 wt. % hydrogen at 300 K under 10 bar (Chen, Shaw et al. 2001). After the CNTs were doped by Li or K, the hydrogen capacity of CNTs may reach 20 wt. % at higher temperature (473 K - 673 K and <313 K, respectively) under 0.1 MPa (Chen, Wu et al. 1999, Yang 2000). However, these data have not been repeated or obtained by other labs.

2.1.4 Carbon nanofibers (CNFs) and graphite nanofibers (GNFs)

CNFs are formed from carbon-containing gas and hydrogen or hydrocarbons with metal catalysts. Normally, CNFs are 5 to 100 μm in length, with a diameter of 5-100 nm (Ströbel, Garche et al. 2006).

The structures of CNFs are influenced by the shape of the metal catalyst and by the ratio of the mixture of hydrocarbons and hydrogen, leading to different types of morphology, crystallinity and shape. A carbon nanofiber consists of metal catalyst

particles and graphite platelets (Goodman, Kelley et al. 1980, Nakamura, Hirano et al. 1989). It was also found that the form of the graphite platelet depends on the shape of the small metal catalyst (1.0-2.0 m^2/g) (Fig 2.4).

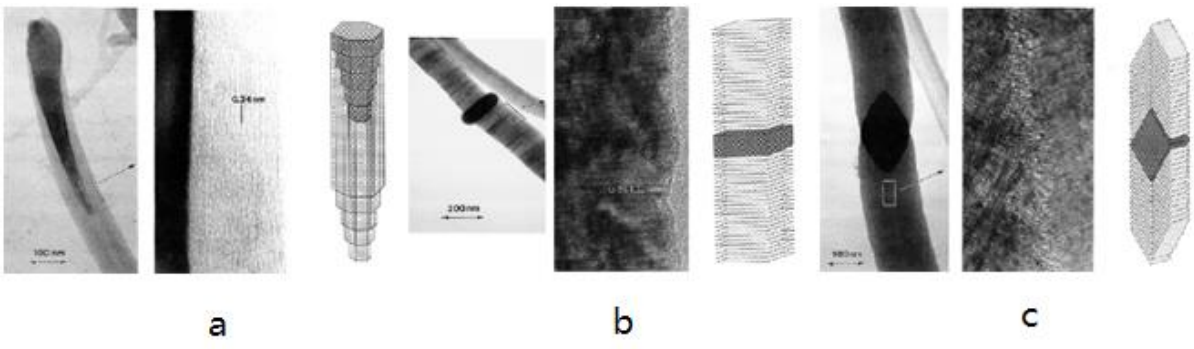

Figure 2.4 Scheme of three different structures of CNFs where the dark parts are the metal catalyst and the platelets are mainly formed of graphite. a: tubular structure, b: deck of cards structure and c: herringbone structure (Nelly M. Rodriguez 1995).

In terms of the hydrogen storage capacity of CNFs, it was deduced that high hydrogen pressure can expand the interlayer distance of graphite platelets, which means the hydrogen molecules or atoms can be stored inside the platelets (Park, Anderson et al. 1999).

Chambers (Chambers, Park et al. 1998) reported that they got 23.33 L/g hydrogen which is stored in herringbone GNFs and 12.98 L/g hydrogen stored in platelets structured GNFs. However, these results have not been reproduced in other labs (Ströbel, Garche et al. 2006), and it is widely agreed that these exceptionally high values are due to water contamination. Some other researchers also measured the hydrogen storage properties of CNFs/GNFs, and only found <0.1-1.6 wt. % hydrogen at room temperature under 10-12 MPa (Poirier, Chahine et al. 2001, Tibbetts,

Meisner et al. 2001, de la Casa-Lillo, Lamari-Darkrim et al. 2002, Hirscher and Becher 2003).

2.1.5 Graphite as a hydrogen storage material

Graphite has been investigated as an attractive medium for storing hydrogen because of its inexpensive cost and light weight (Ichikawa, Chen et al. 2004, Zhang 2009, Roy 2012). The interaction may be based on either physisorption or chemisorption.

In terms of the unique platelet structure of graphite, which contains multilayers and slit-shaped pores (Figure 2.5), the distance between the layers of a single-crystal graphite was measured as 3.35 Å (Aladekomo and Bragg 1990) for the distance between the slit-shaped pores, slightly wider than the dynamic diameter of hydrogen (2.89 Å) (Chambers, Park et al. 1998). Owing to the weak bonding between the platelets, hydrogen can be absorbed via multilayer formation when the expansion of the interlayer occurs.

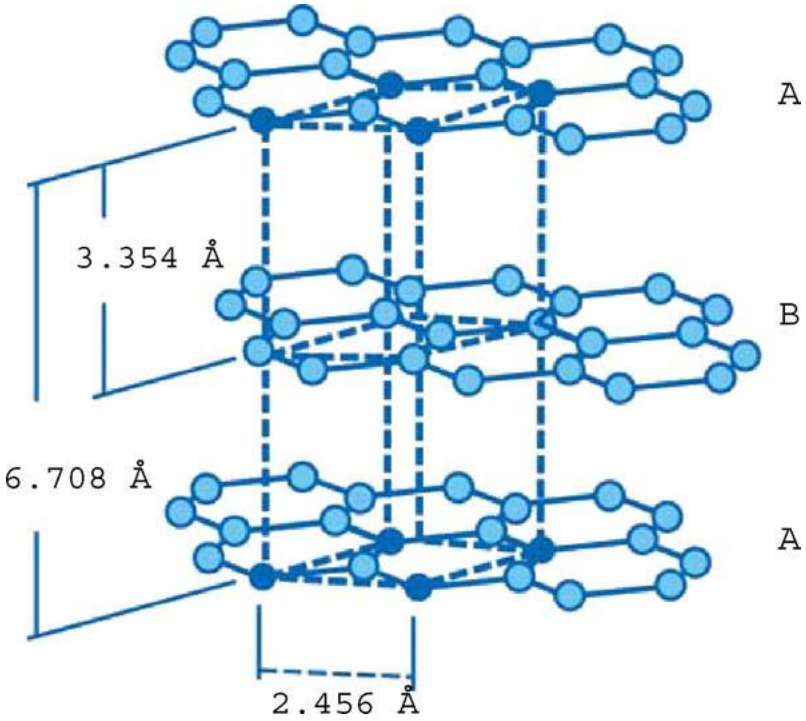

Figure 2.5 Graphite structure(Ströbel, Garche et al. 2006).

However, researchers found that ≤3.5 Å layer distance is not large enough for hydrogen molecules to be absorbed (Ströbel, Garche et al. 2006), and via simulation(Patchkovskii, Tse et al. 2005), nano-structured graphite with a 0.6-0.7 nm interlayer distance may absorb up to 5 wt. % hydrogen (250 K, 500 bar(external H_2 pressure)) under ambient condition (Patchkovskii, Tse et al. 2005).

2.2 Nano-structured graphite by ball milling

2.2.1 Effect of ball milling

Ball milling was reported as an effective method to enhance the hydrogen storage properties of graphite by modifying its structure (Chen, Fitz Gerald et al. 1999, Welham, Berbenni et al. 2003, Zhang and Book 2011). It was found that the surface area (BET Brunaer-Emmett-Teller area) of milled graphite under 300 kPa Ar can

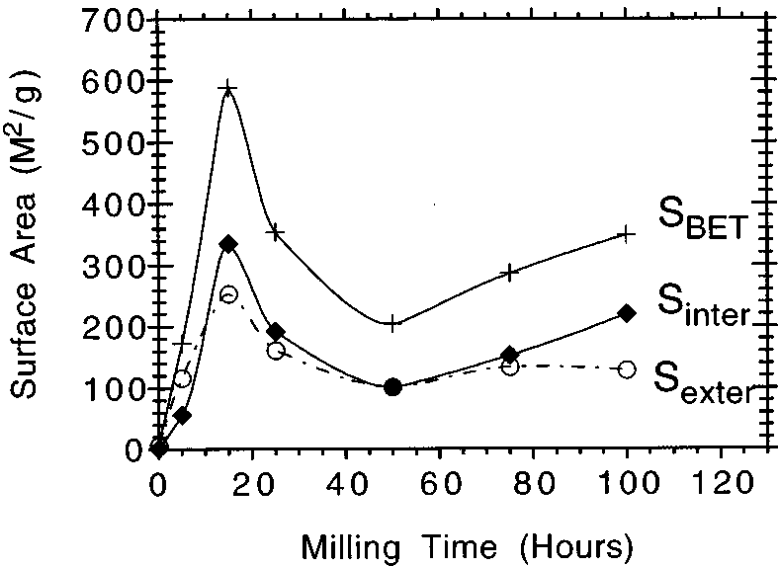

Figure 2.6 The variation trend of BET area, internal and external surface area changed with the increasing milling time of graphite powders, the graphite powders are milled using a Uniball mill under 300 kPa Ar (Chen, Fitz Gerald et al. 1999).

reach 589 $m^2\ g^{-1}$, which combines an external surface area 254 $m^2\ g^{-1}$ and internal surface area 335 $m^2\ g^{-1}$ (Chen, Fitz Gerald et al. 1999). Figure 2.6 gave the variation trend of BET area of graphite milled for different milling times, which shows that the external area decreased with the increasing of milling time while the trend of internal area went to the opposite side after 75 h milling. It is supported by the generation of nanopores inside the graphite (Chen, Fitz Gerald et al. 1999). However, as Figure 2.6 shows, the BET surface area of the graphite powder milled between 15-50 hours decreased, this is believed to be due to agglomeration of the powders (Chen, Fitz Gerald et al. 1999, Orimo, Majer et al. 1999).

XRD measurements were used to analyse the structural changes in milled graphite (Tidjani, Lachter et al. 1986, Shen, Ge et al. 1996, Chen, Fitz Gerald et al. 1999). The (002) reflection peaks observed from 4h/8h milled graphite (10 g pure graphite powder milled with a ball to powder weight ratio of 40, under dry Ar, planetary ball-mill with a rotation rate 720rpm) were found to be asymmetric and broadened (Shen, Ge et al. 1996). They were estimated as a combination of two components: d_{002}=0.340 nm was attributed to crystalline graphite, and d_{002}=0.370 nm to lattice defects (Tidjani, Lachter et al. 1986, Aladekomo and Bragg 1990).

The disordered graphite was also characterised using Raman Spectroscopy. In Figure 2.7 (left) two Raman peaks were observed for both the as received graphite (the initial graphite is not completely ordered) and the graphite milled under dry pure Ar for different milling times: the G peak (around 1580 cm^{-1}) is related to the typical crystal structure of graphite, and the D peak (around 1360 cm^{-1}) is due to defective graphite (Aladekomo and Bragg 1990, Welham and Williams 1998, Chen, Fitz Gerald et al. 1999, Reich and Thomsen 2004). The two peaks became broader when the samples were milled for longer, and the height of the 1360 cm^{-1} peak grows with increasing milling time due to the increasing quantity of lattice defects. Figure 2.7 (right) shows the change in particle size for the graphite (the graphite powder was milled with different milling times under 3 bar H_2) using SEM: it is shown that ball milling can reduce the particle size of the as-received graphite.

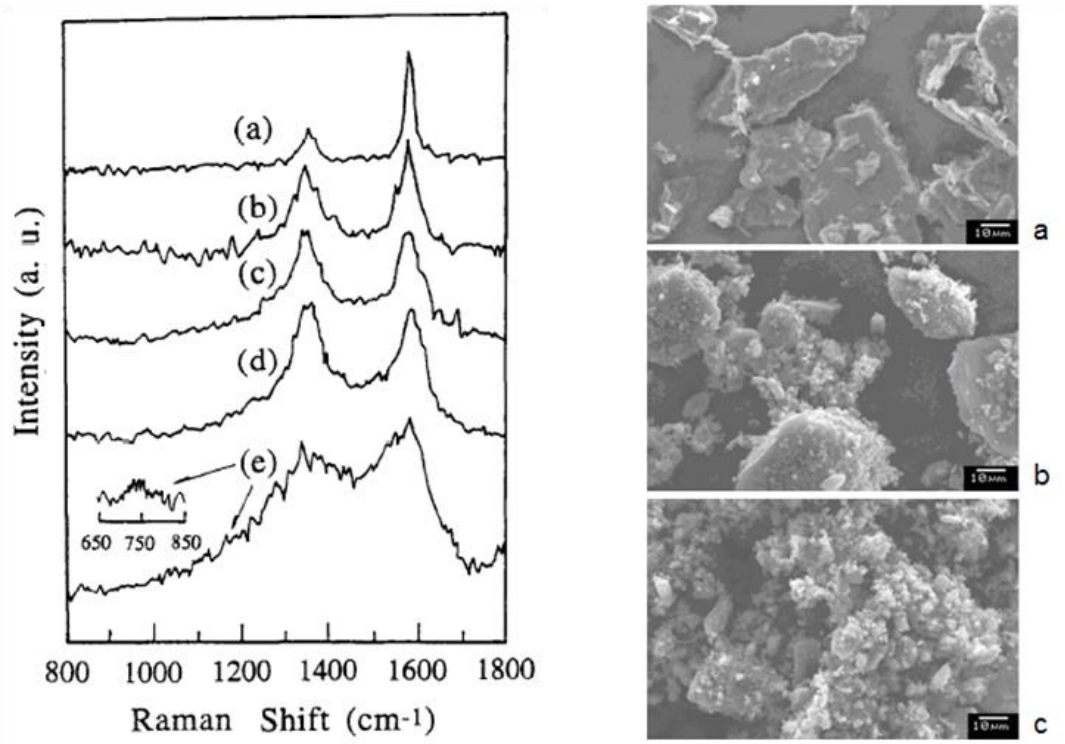

Figure 2.7 Figure 2.7 Diagram on left is the Raman Spectrum of graphite milled for (a) 0h, (b) 4h, (c) 8h, (d) 16h, (e) 40h (Shen, Ge et al. 1996); the one on the right is the SEM test of graphite: a as-received graphite, b 10h milled graphite under 3 bar H_2; c 40h milled graphite under 3 bar H_2 (Zhang 2009).

2.2.2 Hydrogen storage in milled graphite

It was reported that the graphite milled for 80 hours under 1 bar H_2 atmosphere, stored 7.4 wt. % hydrogen (measured by oxygen-combustion hydrogen analysis Elementar Vario-EL) (Orimo, Majer et al. 1999). The reason for this higher C-H ratio is considered to be the formation of dangling carbon bonds by ball milling (Fukunaga, Nagano et al. 1998, Chen, Fitz Gerald et al. 1999, Orimo, Majer et al. 1999).

When hydrogen is milled with graphite, two types of C-H bonding occurs (showed in Figure 2.8) with interatomic distances of 0.11 nm and 0.18 nm, respectively (Orimo, Majer et al. 1999, Orimo, Züttel et al. 2003). According to the peak around 0.18 nm, the interlayer distance of milled graphite under hydrogen atmosphere was calculated

as 0.36 nm, compared with the interlayer distance (0.34 nm) of graphite without deuterium, it showed the host interlayer distance was expanded nearly 6 % by adding hydrogen (Orimo, Majer et al. 1999).

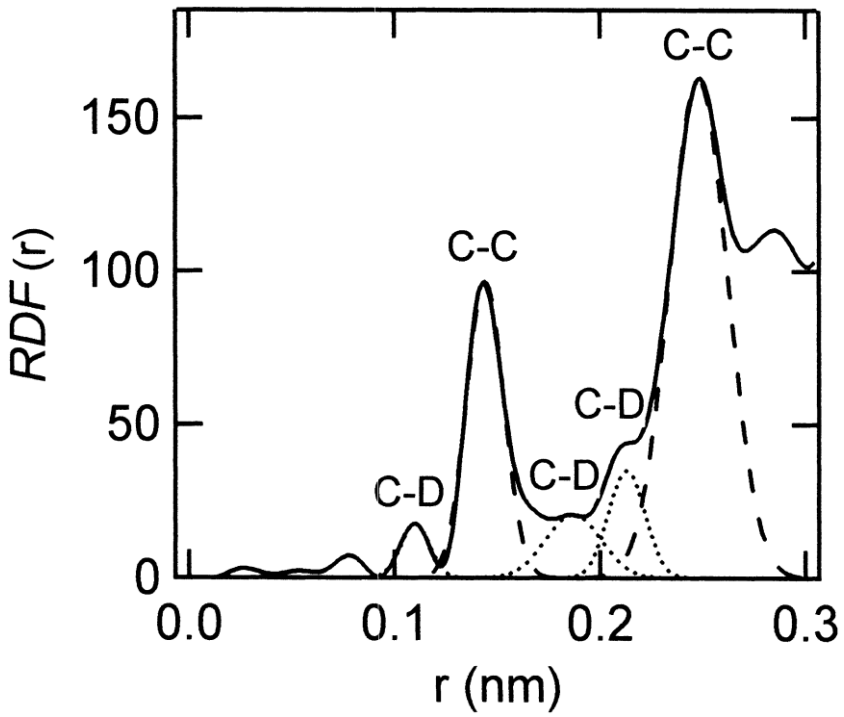

Figure 2.8 RDF (r) spectrum of ball-milled graphite C-D (Orimo, Majer et al. 1999)

Ball milling increases the ratio of sp^3 bonding to sp^2 bonding in milled graphite (Itoh, Miyahara et al. 2003). This is shown by the Raman spectra (Figure 2.9), with the intensity of the D peak (peak generated by sp^3 bonding) increasing and the G peak (peak generated by sp^2 bonding) decreasing, with increasing milling time. This has been explained in terms of the crystalline graphite structure transforming into disordered or amorphous phases during ball milling (Orimo, Majer et al. 1999). TEM has also been used to study microstructural changes during milling (Figure 2.10).

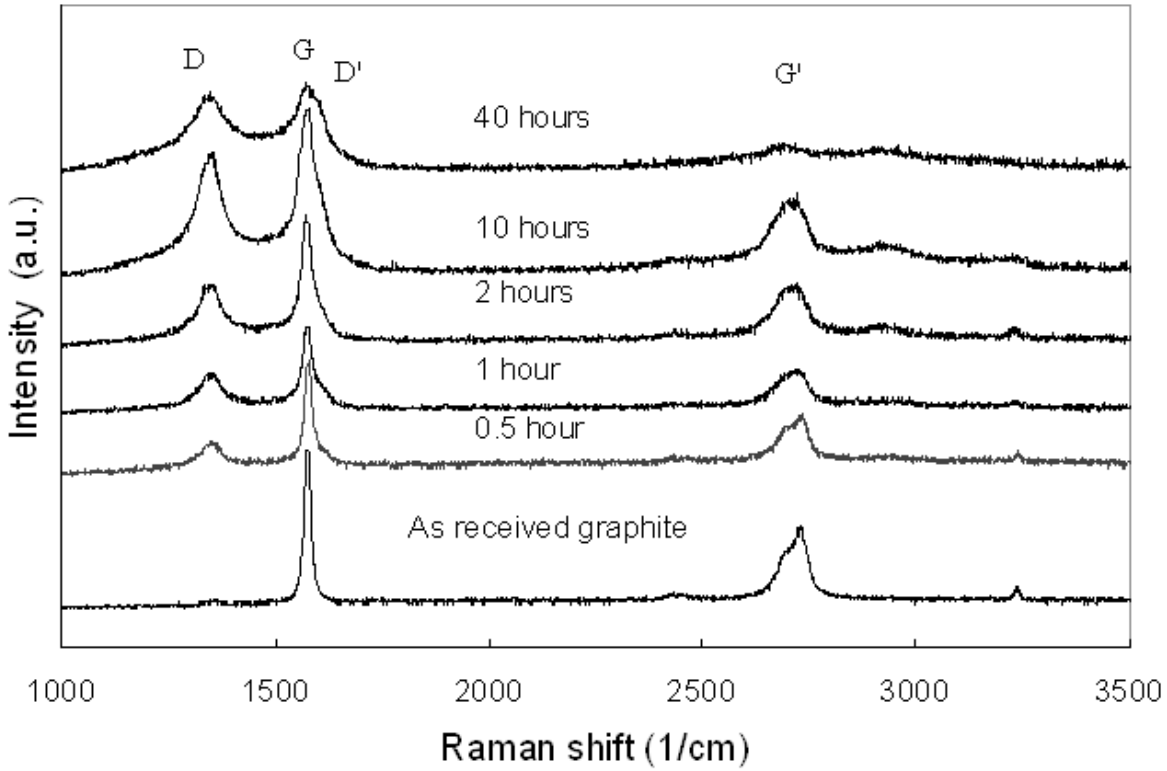

Figure 2.9 Raman spectrum of milled graphite by different milling time under 3 bar H_2 and 280 rpm milling speed (Zhang 2009).

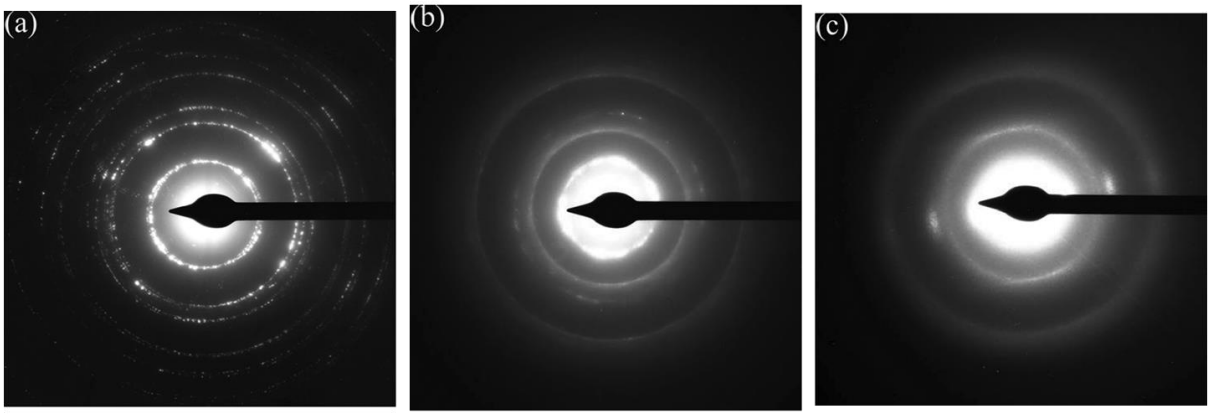

Figure 2.10 TEM patterns of (a) as-received graphite; milled graphite under 3 bar H_2 for (b) 10 hours; (c) milled graphite for 40 hours (Zhang and Book 2011). Graphite milled for 40 hours was more disordered than the one for 10 hours and the host graphite.

Zhang et al. milled graphite for different milling times under 3 bar H_2 and found that graphite milled for 10 hours desorbs the largest amount of hydrogen after heating to

990 °C (2 °C/min) in 0.5 bar flowing Ar (5.5 wt. %) without any other impurity gases (Zhang 2009, Zhang and Book 2011). However, if the graphite was milled over 10 hours, methane was detected in the desorbed gas (Zhang 2009). Other researchers also found that the microstructure of graphite and its hydrogen desorption properties can be influenced by milling time, milling atmosphere pressure, and milling mode (Orimo, Majer et al. 1999, Huang, Calka et al. 2007).

2.3 Hydrogen storage characterization of milled graphite by different milling conditions

2.3.1 Milling time

As seen in the previous discussion (Section 2.2) about the structural changes and phase transition, the longer the milling time for graphite (under dry pure Ar or H_2), the more disordered and/or amorphous phases appear. However, the specific surface area reduced when graphite was milled for more than 8 hours due to agglomeration (Orimo, Majer et al. 1999), see Figure 2.11. It should be noted that agglomeration occurs earlier in this sample which was milled under hydrogen (agglomeration comes out after 8 h milling), compared with the sample milled under Ar in Figure 2.6 (agglomeration occurs after 15 h milling), which is supposed to be influenced by different milling modes and sources of the as-received graphite.

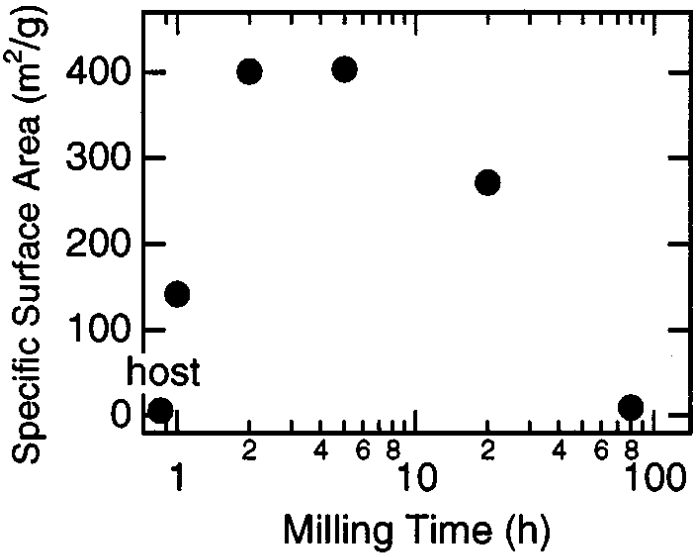

Figure 2.11 Specific surface area of milled graphite under 1 bar H_2 for different milling time (Orimo, Majer et al. 1999).

The hydrogen density in milled graphite increases with increasing milling time (Orimo, Majer et al. 1999) (Figure 2.12), but this does not necessarily mean that the longer milling time leads to an increased amount of desorbed hydrogen. Zhang and Book et al. found that 10 hours would be the best milling time for hydrogenated graphite by ball milling under 3 bar H_2, for the highest mass loss (5.5 wt. %) of hydrogen (Figure 2.13) without any methane release during heating to 990 °C (Zhang and Book 2011).

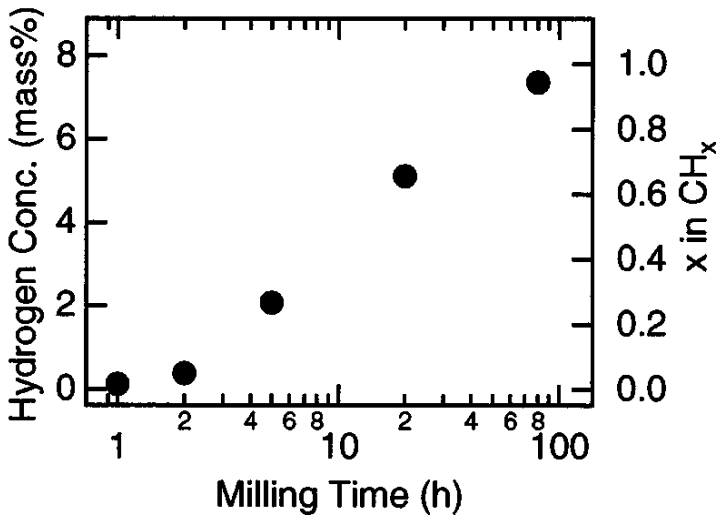

Figure 2.12 Hydrogen density in milled graphite, the milling undergoes a pressure of 1 bar H2 under different milling time (Orimo, Majer et al. 1999).

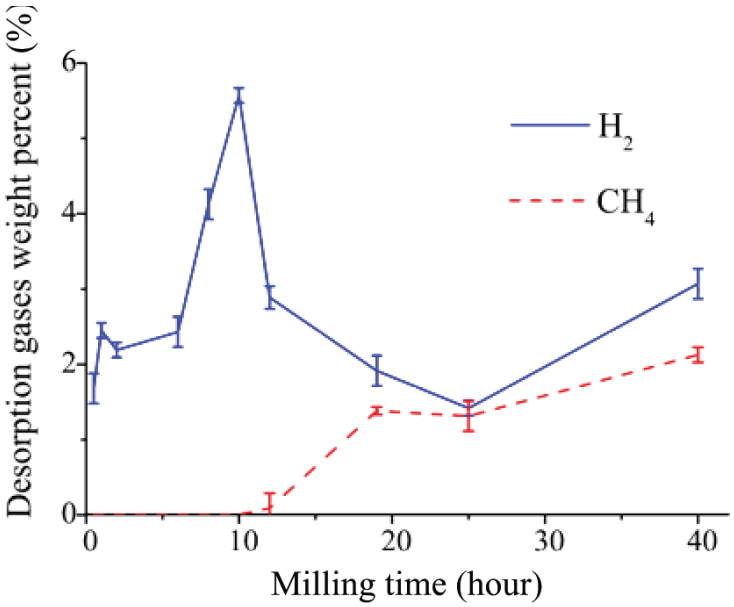

Figure 2.13 The total amount of gases (hydrogen and methane) released during heating in TGA-MS between 50-990 °C from milled graphite under 3 bar H_2 for different milling time (Zhang and Book 2011).

2.3.2 Milling pressure

The effect of hydrogen pressure during milling on the properties of milled graphite was investigated, and it was found that the intensity of the (002) XRD peak for

graphite (Figure 2.14 (a)) decreased and broadened with decreasing milling pressure. This suggested that the amounts of disordered graphite increased with the reduced hydrogen pressure during milling (Chen, Ichikawa et al. 2003, Ichikawa, Chen et al. 2004). This is shown in the Raman spectra, which are shown in Figure 2.14 (b). The peak around 1360 cm^{-1} is associated with the D peak (Section 2.2.2), and becomes more intense with decreased hydrogen milling pressure: therefore, more disordered phase was produced under a lower hydrogen milling pressure (Chen, Ichikawa et al. 2003).

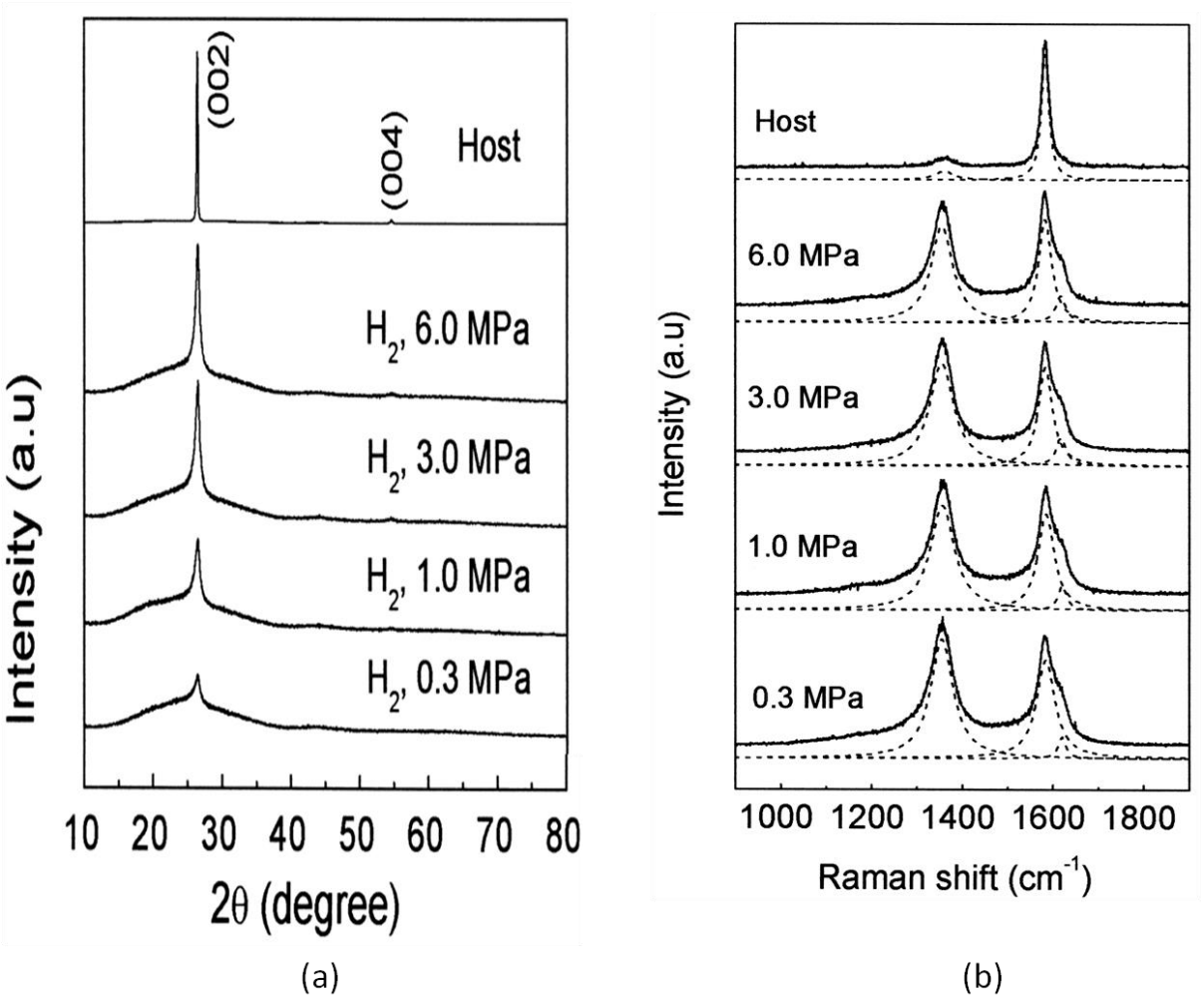

Figure 2.14 (a) XRD patterns and (b) Raman spectra of graphite milled for 2 hours under different hydrogen pressures (Chen, Ichikawa et al. 2003) .

2.3.3 Milling mode

It was reported (Huang, Calka et al. 2007) that the impact mode (Figure 2.15 (b)) of ball milling is more effective than shearing mode (Figure 2.15 (a)) for its higher-energy effect which was believed to create more defects in graphite.

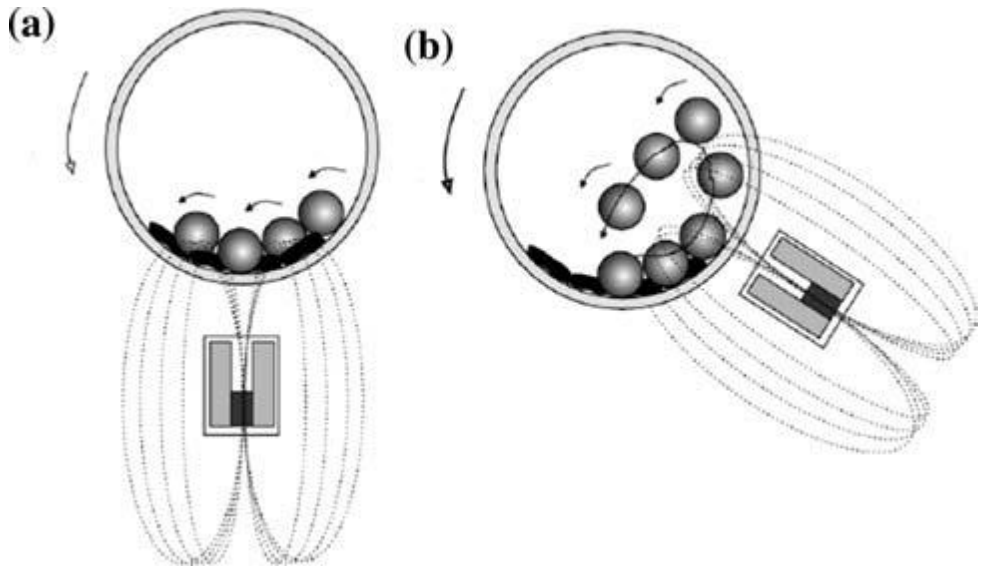

Figure 2.15 Ball-milled graphite under shearing mode (a) and impact mode (b) (Huang, Calka et al. 2007).

The graphite after ball-milling by shearing mode can only absorb 0.6 wt. % hydrogen, much smaller than the quantity of hydrogen (2.7 wt. %) absorbed by graphite milled using an impact mode (Huang, Calka et al. 2007). However, the high-energy mode also introduced contamination such as Fe or iron carbide (N. J.Welham 1998, Ichikawa, Chen et al. 2004, Huang, Calka et al. 2007). Therefore, the materials of the milling pot and milling balls should also be considered before experiments. Tungsten carbide (WC) milling pot and milling balls were found as a good milling device with less interference (Chen, Fitz Gerald et al. 1999, Zhang and Book 2011).

2.4 Addition of Li-based material in milled graphite

2.4.1 Milled graphite with the addition of LiH

Composites of graphite and LiH with the molar ratio of $C_{nano}H_x$: LiH (2:1), were prepared by ball milling (Ichikawa, Fujii et al. 2005). It was found that this composite could reversibly store hydrogen for at least the first 5 cycles (at 350 °C under 8 h vacuum (dehydrogenation) and 3 MPa H_2 (rehydrogenation)) (Figure 2.16) (Ichikawa, Fujii et al. 2005, Miyaoka, Ichikawa et al. 2009).

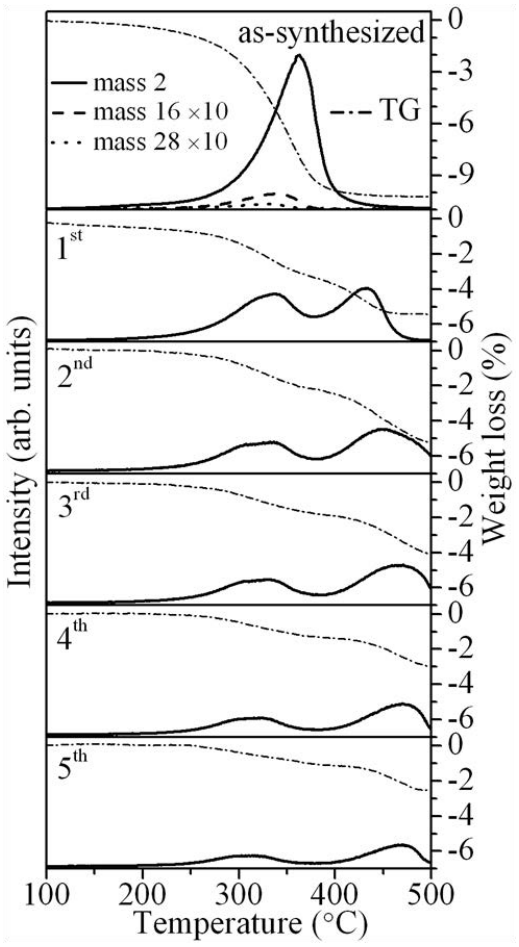

Figure 2.16 TDMS (dash line) and TG (dot line) test results of the composite of milled graphite and LiH after each hydrogenation/dehydrogenation cycle (Miyaoka, Ichikawa et al. 2009).

However, the composite was only able to absorb/desorb 5 wt. % hydrogen at the first two thermal treatments, the quantity of mass loss decreased with the increased number of cycling (Miyaoka, Ichikawa et al. 2009). The reversibility of composite graphite and LiH was attributed to the formation of Li_2C_2 during dehydrogenation

(Ichikawa, Fujii et al. 2005, Miyaoka, Ichikawa et al. 2007, Miyaoka, Ichikawa et al. 2009) as the XRD diffraction peaks of Li_2C_2 always disappeared after the composite was hydrogenated but appeared after the dehydrogenation process (Figure 2.17).

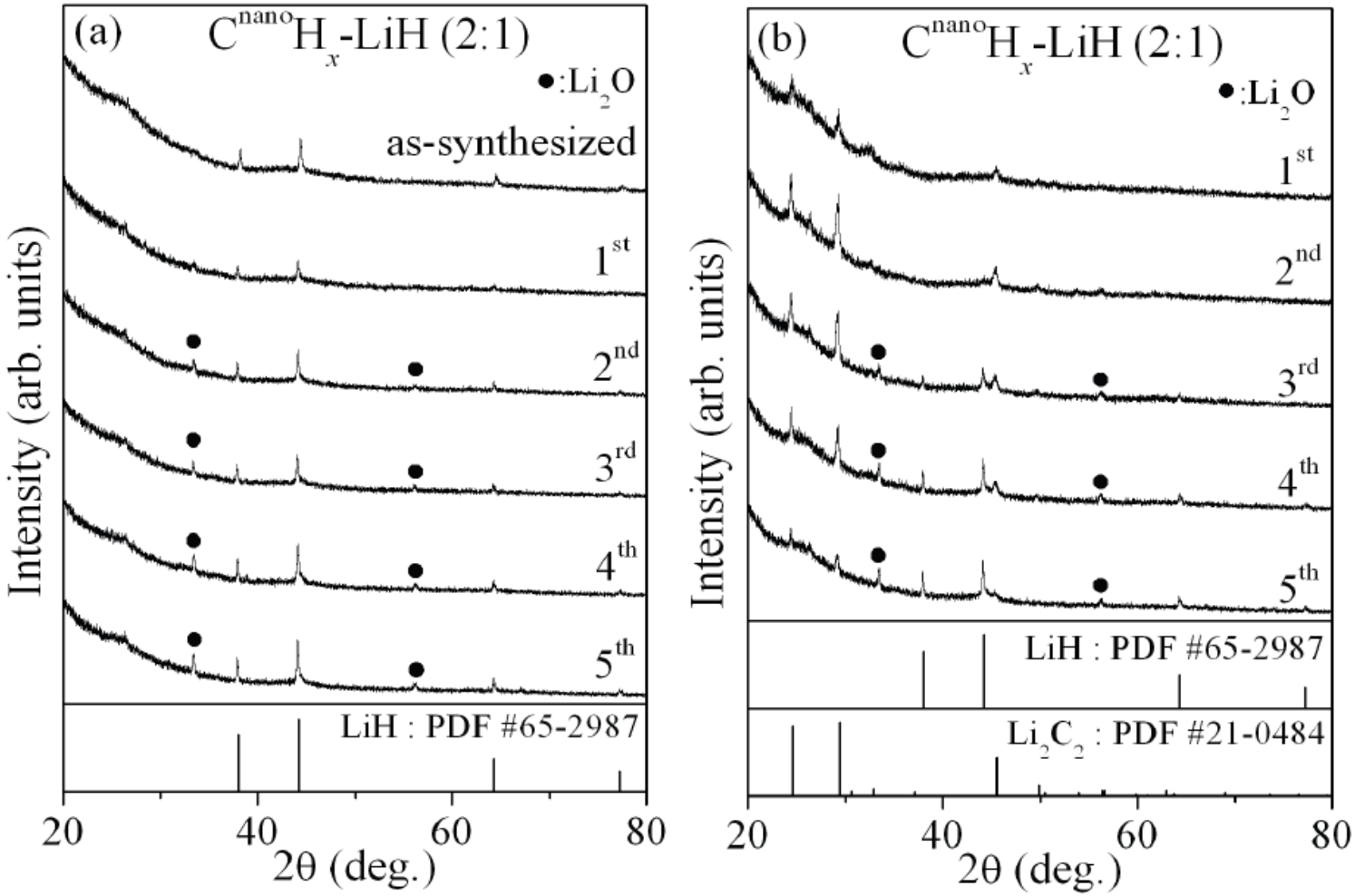

Figure 2.17 XRD patterns of $C_{nano}H_x$ and LiH composite after each hydrogenation (a) and dehydrogenation (b) process (Ichikawa, Miyaoka et al. 2011).

The limitation of the $C_{nano}H_x$: LiH composite is that methane was detected in every desorption cycle (Figure 2.18); it was thought that the methane was formed from the reaction of $C_{nano}H_x$ and the decomposed Li_2C_2 (Miyaoka, Ichikawa et al. 2009).

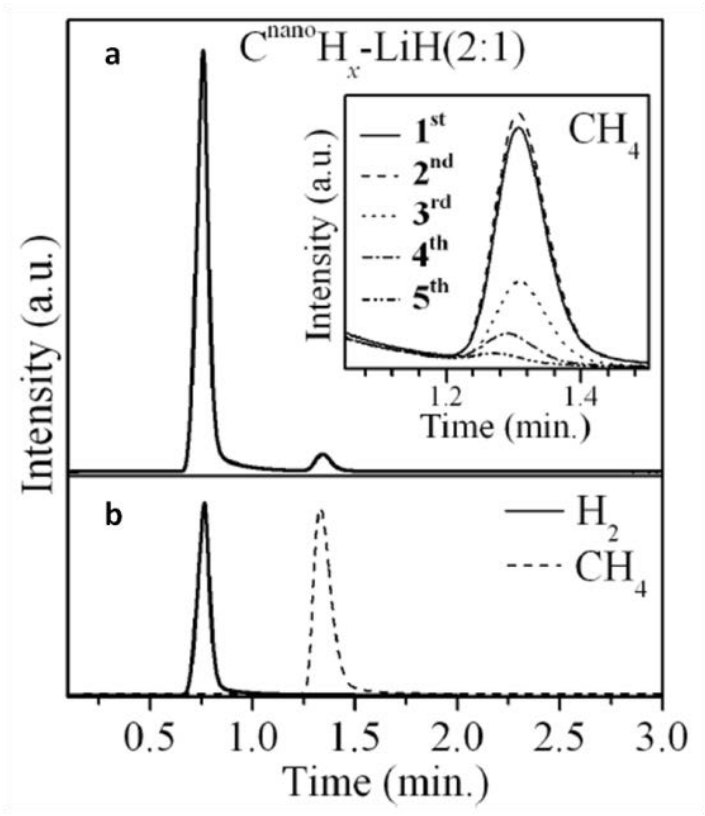

Figure 2.18 a: Gas chromatogram of the gases released during each rehydrogenation process of $C_{nano}H_x$ and LiH composite; b: the gas chromatogram of H_2 and methane from reference (Miyaoka, Ichikawa et al. 2009).

2.4.2 Milled graphite with the addition of $LiBH_4$

$LiBH_4$ was investigated as a suitable hydrogen storage material because it contains 18.3 wt. % of hydrogen. It was found that bulk $LiBH_4$ is relatively stable and a high temperature (>400 $^{\circ}$C) was required to decompose $LiBH_4$ into LiH, B and H_2 (Ngene, van Zwienen et al. 2010).

Zhang, Bevan et al found that the onset temperature for dehydrogenation can be reduced to 230 °C if they ball milled graphite and $LiBH_4$ (molar ratio: 2:1) for 2 h under 3 bar H_2, lower than the onset temperature of hydrogen desorption from both bulk $LiBH_4$ and as-milled graphite (over 350 °C) (Zhang 2009, Zhang, Bevan et al. 2012). In total, 9.3 wt. % hydrogen was released after heating the ball-milled graphite and $LiBH_4$ composite (Zhang, Bevan et al. 2012).

2.5 Li-N-H composites

2.5.1 Synthesis of $LiNH_2$ and LiH by reactive milling of Li_3N

Li_3N was reported to be a reversible hydrogen storage material (Ping. Chen 2002), with a 11.5 wt % theoretical gravimetric capacity of hydrogen. In practice, 9.3 wt. % hydrogen (Figure 2.19) is absorbed for a molar ratio of 4:1 for H : Li_3N=4:1 (Ping. Chen 2002, Gregory 2008), that follows the reaction:

$$\mathrm{Li_3N + 2H_2 \rightarrow Li_2NH + LiH + H_2 \leftrightarrow LiNH_2 + 2LiH} \qquad (1)$$

Li_3N exhibits two different structures, alpha-Li_3N and beta-Li_3N (Boukamp and Huggins 1976). When Li_3N is heated to 473 K, the beta phase undergoes an exothermal transition to the alpha (Beister, Haag et al. 1988). Although there was still a small amount (2.5 wt. %) of beta phase present at 673 K, as this process is not reversible after it was cooled down (Huq, Richardson et al. 2007), it was believed that beta phase Li_3N plays a significant role in the reaction of hydrogen absorbed by Li_3N (Beister, Haag et al. 1988, Huq, Richardson et al. 2007). However, the effect and mechanism of beta phase transition on hydrogen storage of Li_3N needs further studies to be confirmed.

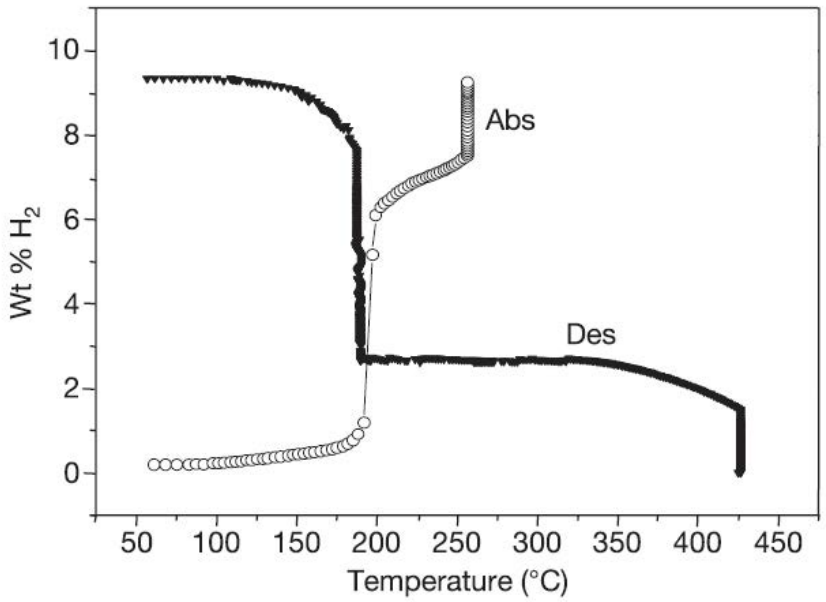

Figure 2.19 The weight changes of Li_3N during hydrogenation (Abs) and dehydrogenation (Des) processes; hydrogenation was carried out in 3 bar H_2 with heating from 50 °C to 255 °C at a heating rate 2 °C/min and maintained at 255 °C for 30 mins, in dehydrogenation process, the sample was cooled down to 50 °C before the sample chamber was vacuumed, and then heated up to 195 °C until no further mass loss was detected (Ping. Chen 2002).

It has been proposed that Equation (1) involves the following two steps (Ping. Chen 2002, Ichikawa, Isobe et al. 2004, Palumbo, Paolone et al. 2008):

$$Li_3N + H_2 \rightarrow Li_2NH + LiH \qquad \Delta H = -165\ kJ/molH2 \qquad (2)$$

$$Li_2NH + H_2 \leftrightarrow LiNH_2 + LiH \qquad \Delta H = -44.5\ kJ/molH2 \qquad (3)$$

It should be noted that the enthalpy change (ΔH) of Equation (2) (-165 kJ/mol H_2) is much higher than that for Equation (3) (-44.5 kJ/mol H_2), and it was shown that Equation (3) can absorb and desorb 6.5 wt. % of hydrogen (Ichikawa, Isobe et al. 2004, Pinkerton 2005, Gregory 2008). Therefore, Equation (3) has been considered to be of interest for hydrogen storage (Ichikawa, Isobe et al. 2004, Pinkerton 2005, Takayuki Ichikawa 2005, Gregory 2008, Palumbo, Paolone et al. 2008).

2.5.2 $LiNH_2$+LiH composite as a reversible hydrogen storage material

In the measurements of thermodynamic properties of a $LiNH_2$+LiH composite, ammonia was detected during heating (Ichikawa, Isobe et al. 2004, Pinkerton 2005). This shows that Equation (3) does not occur in a single reaction, but via a series of reactions.

2.5.2.1 Mechanism of $LiNH_2$ and LiH composite

In order to understand the mechanism of the reaction in Equation (3), Ichikawa, et al heated as-received $LiNH_2$ from 50 °C to 400 °C by TG and monitored the released gases during heating by MS, from which they found that ammonia desorbed with the onset temperature of 300 °C (Figure 2.20) with a small amount of hydrogen detected at the same time (Ichikawa, Isobe et al. 2004). XRD of $LiNH_2$ powder after heating to 500 °C (Figure 2.21), showed that Li_2NH was formed during heating (Leng, Ichikawa et al. 2005).

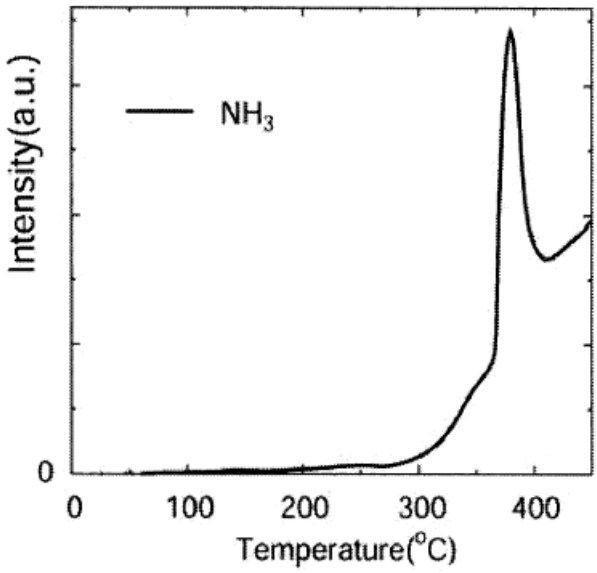

Figure 2.20 TG-TDMS of as-received $LiNH_2$ under a heating rate as 5 °C (Ichikawa, Isobe et al. 2004).

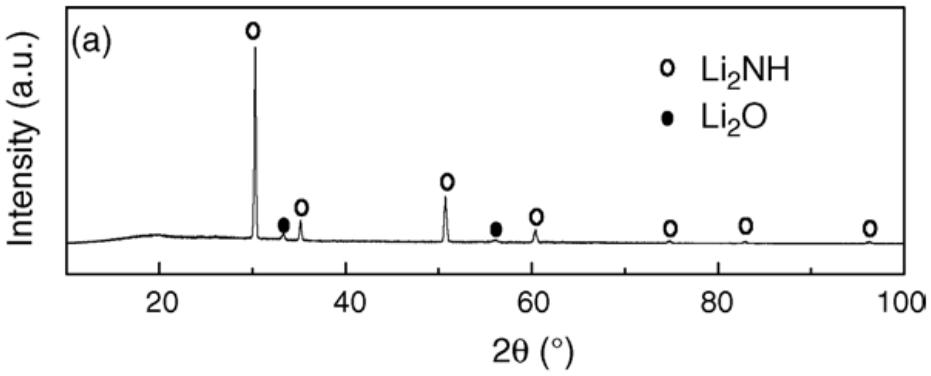

Figure 2.21 XRD pattern of $LiNH_2$ after heating to 500 °C in helium flow (Leng, Ichikawa et al. 2005)

According to the rapid reaction between LiH and ammonia (Equation (5)) (Ruckenstein 2006, Gregory 2008) and the decomposition of $LiNH_2$, the reaction in Equation (3) was proposed to occur in two steps (Ichikawa, Chen et al. 2004, Ichikawa, Hanada et al. 2004, Gregory 2008):

$$2LiNH_2 \rightarrow Li_2NH + NH_3 \qquad (4)$$

$$NH_3 + LiH \rightarrow LiNH_2 + H_2 \qquad (5)$$

i. Synthesis by ball-milling or powder-mixing

It was reported that in the reaction of Equation (5), the quantity of ammonia absorbed by LiH depends on the contact between the two elements (Ichikawa, Hanada et al. 2004, Shaw, Ren et al. 2008). Ball-milling was found to be an effective method to prepare the nano-structured $LiNH_2$+LiH composite. The high energy mechanical vibration reduced the particle size (Figure 2.22), changed the crystal structure of the composite and increased the BET surface area of the composite (Ichikawa, Hanada et al. 2004, Yao, Shang et al. 2007, Shaw, Ren et al. 2008, Varin, Jang et al. 2010).

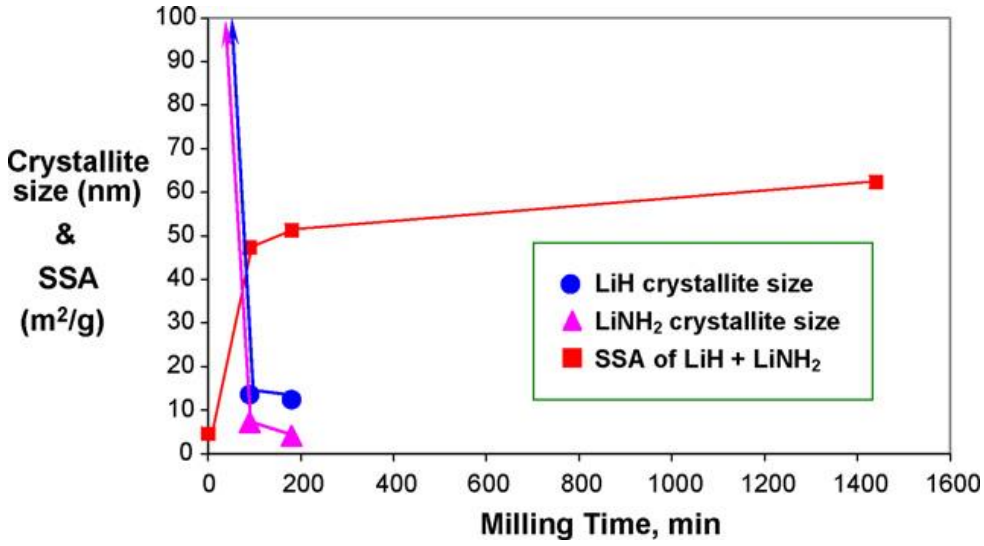

Figure 2.22 Crystallite sizes of $LiNH_2$ and LiH in the mixture by ball-milling and the BET area of the $LiNH_2$+LiH composite milled for different time (Shaw, Ren et al. 2008).

Figure 2.23 shows TGA and DSC for $LiNH_2$+LiH composites that were milled for different durations. The TGA diagram (Figure 2.23 (a)) shows that the milled sample has a lower mass loss (5.5 wt. %) than the sample without ball-milling (8.1 wt. %) (Shaw, Ren et al. 2008). However, the theoretical mass loss of hydrogen in Equation (3) is 6.5 wt. %, which means the 8.1 wt. % gases released from the un-milled sample included ammonia (Shaw, Ren et al. 2008). This was confirmed by DSC measurement, by which they found an endothermic peak of melting $LiNH_2$ at 360 °C (Figure 2.23(b)), with NH_3 released from the un-reacted $LiNH_2$ (Shaw, Ren et al. 2008, Varin, Jang et al. 2010).

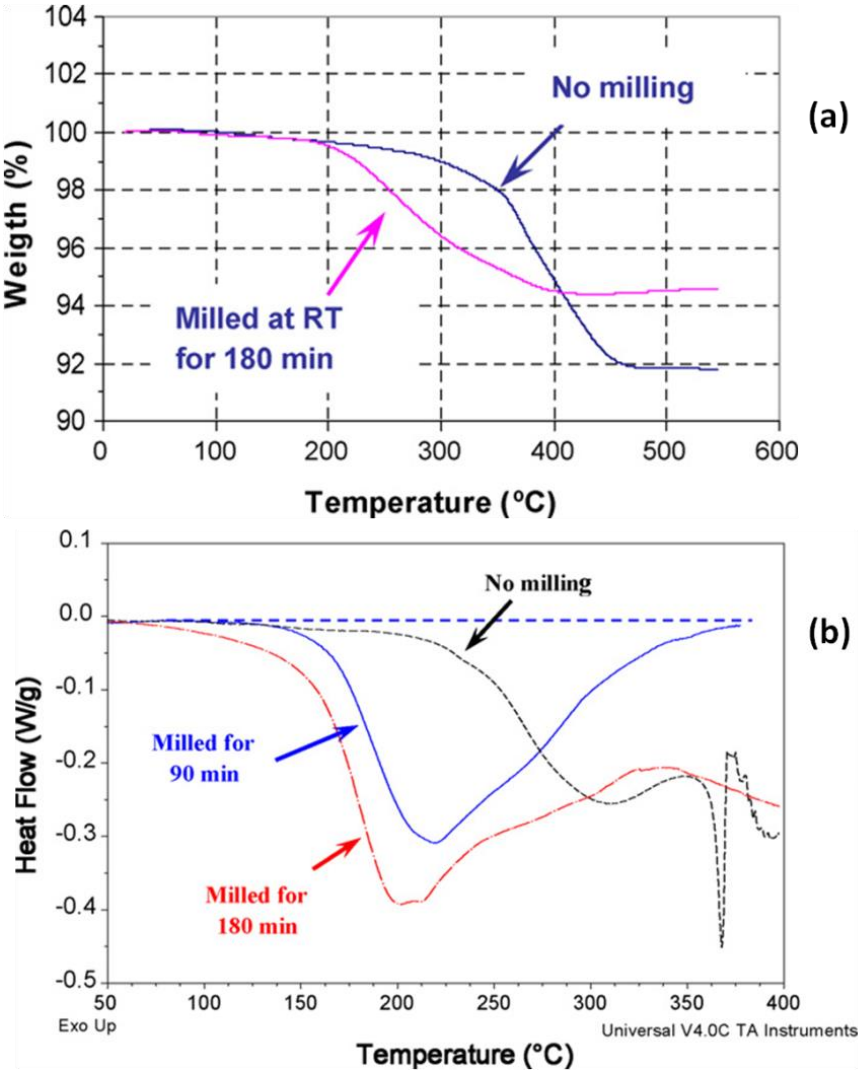

Figure 2.23 (a) The TGA analysis of milled and un-milled $LiNH_2$+LiH composite, heating rate is 10 °C/min; (b) DSC measurements on un-milled and milled $LiNH_2$+LiH composite, heating rate is 1 °C/min (Shaw, Ren et al. 2008).

Therefore, ball-milling is an effective method to enhance the hydrogen storage properties of $LiNH_2$+LiH composites.

ii. The effect of milling time

Ball-milling up to 25 h can increase the specific surface area (SSA) of the $LiNH_2$+LiH composite (Figure 2.24), however, afterwards the SSA decreased slightly which was considered to be due to agglomeration (Varin, Jang et al. 2010). As shown in Figure

2.25, at least 4 hours milling time is required for an acceptably low ammonia desorption level (Yao, Shang et al. 2007).

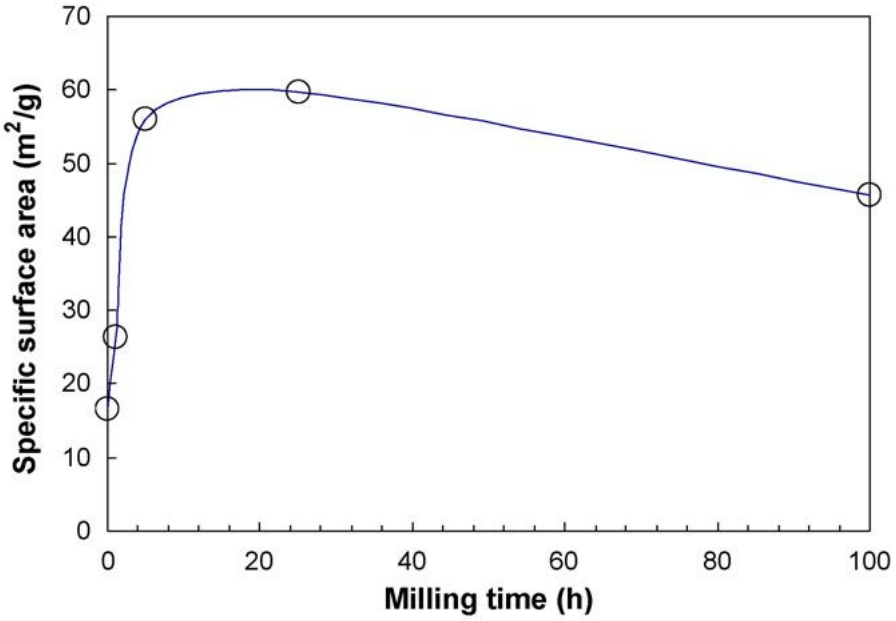

Figure 2.24 SSA (specific surface area) of the $LiNH_2$+LiH composite for different milling time (Varin, Jang et al. 2010).

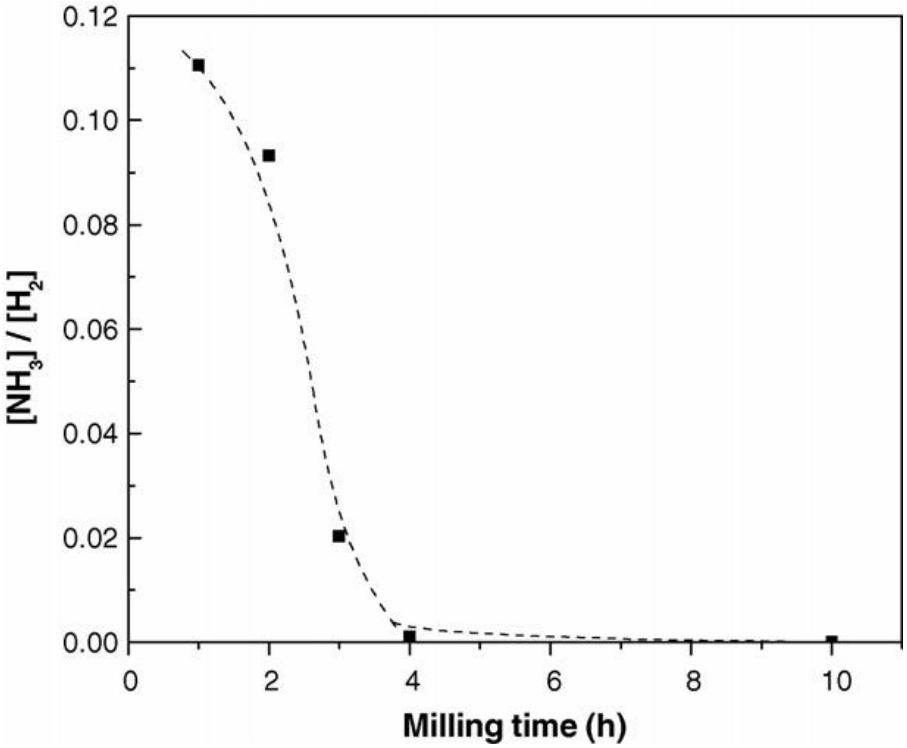

Figure 2.25 The ratio of the amounts of NH_3 to H_2 released from the $LiNH_2$+LiH composite milled for different milling time (Yao, Shang et al. 2007).

It was also found that the SSA of the composite did not change a lot when it was milled between 5 to 25 hours, and the same with the quantity of released ammonia (Yao, Shang et al. 2007, Varin, Jang et al. 2010).

iii. Synthesis at different molar ratios

In the early research on the composite of $LiNH_2$ and LiH, 1:1 was the popular ratio for the synthesis of the composite. However, ammonia still existed during the dehydrogenation process. Ichikawa, Isobe et al found that the molar ratio of $LiNH_2$ and LiH may influence the ammonia level, when more LiH was added in the composite, less ammonia was released during the dehydrogenation process (Ichikawa, Isobe et al. 2004).

1:1.2 was reported as the optimum molar ratio because it resulted in the lowest activated energy (Figure 2.26 (a)), lowest ammonia and highest hydrogen level during dehydrogenation (Figure 2.26 (b)) (Varin, Jang et al. 2010).

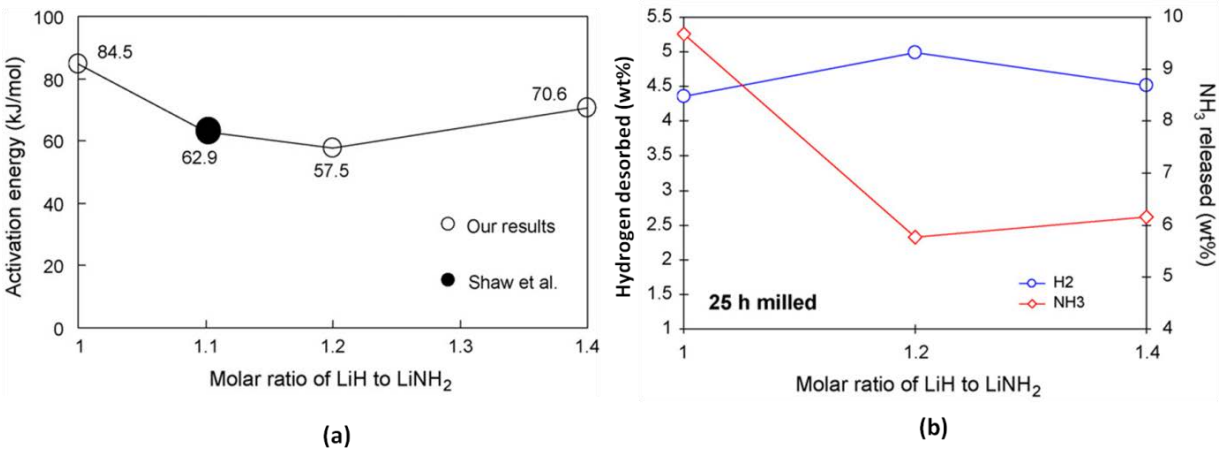

Figure 2.26 (a) The activation energy of the reaction of $LiNH_2$ and LiH (milled for 25 h) by various molar ratios; (b) The amounts of NH_3 and H_2 released from the 25 hours milled $LiNH_2$+LiH composite by different molar ratio (Varin, Jang et al. 2010).

3 Aims

This work will investigate the hydrogen storage properties of a ball-milled graphite+$LiNH_2$+LiH composite. In order to understand the hydrogen storage mechanism of this ternary composite, the reactions and hydrogen storage capacity of the binary composites will also be studied. Therefore, investigations of $LiNH_2$, ball-milled hydrogenated graphite and the composite graphite+$LiNH_2$, $LiNH_2$+LiH will be undertaken, in an attempt to understand what reactions occur between the different components. The hydrogen storage performances of these single material and binary composites may give the reaction evidences for the nature of three-phase composite. The study of these composites will also be undertaken under different molar ratio and O_2 content.

4 Experimental Methods

4.1 Sample preparation

High-purity (>99.99%) graphite powder was purchased from Alfa Aesar (-325 mesh powder size, synthetic, conducting grade). Lithium amide (purity 95%, hydrogen-storage grade) and lithium hydride (purity 95%, -30 mesh powder size) were purchased from Sigma Aldrich Ltd.

4.1.1 Milled graphite

A tungsten carbide (WC) milling pot (250 ml) (Figure 4.1), milling balls (10 mm diameter WC balls) and a Retsch PM400 Planetary Ball Mill (Figure 4.2) were used. Firstly, the as-received graphite was heated under vacuum (10^{-5} bar) in a furnace to 150 °C for more than 8 h. Then the dried graphite powder was loaded and sealed into the milling pot with milling balls (mass ratio of ball to graphite is 14:1) in an Ar-flowing glovebox. Milling was carried out in 3.0 bar hydrogen at 280 rpm. The samples were milled for 8 h, with intervals of 15 min milling and 15 min waiting (to allow cooling). The milling pot was recharged with H_2 whenever the pressure was below 2.75 bar.

Figure 4.1 250 ml WC milling pot

Figure 4.2 Retsch PM400 Planetary Ball Mill

4.1.2 Milled $LiNH_2$+1.2LiH

As-received $LiNH_2$ and as-received LiH were mixed in a molar ratio of 1:1.2. In order to mix the powder, it was loaded and sealed into the milling pot with milling balls (ball to powder ratio 14:1) in an argon flow glovebox. Milling was carried out in 1.0 bar Ar at 280 rpm. The powder was milled for two different milling times: 5 h and 3 h, both of them were milled with 5 min milling and 5 min waiting for cooling down.

4.1.3 Graphite and $LiNH_2$ (Li_3N)

As-received $LiNH_2$ (Li_3N) was mixed with 8-hour milled graphite at a molar ratio 1:2 and the mixture powder was loaded and sealed into the milling pot with milling balls (ball to powder ratio of 14:1) in an argon flow glovebox. Milling was carried out in 3.0 bar H_2 at 280 rpm. The sample was milled for 2 hours, with 15 min milling and 15 min rest to allow the sample to cool.

4.1.4 Composite $LiNH_2$+LiH+graphite

The milled $LiNH_2$+1.2LiH powder prepared (see section 4.1.2) was mixed with 8h milled graphite prepared (see section 4.1.1) at a molar ratio 1:2. The mixed powder was loaded and sealed into the milling pot with milling balls (ball to powder ratio of 14:1) in an argon flow glovebox. The sample was milled for 2 h with 15 min milling and 15 min rest (3.0 bar H_2, 280 rpm).

4.2 Sample characterization

4.2.1 X-Ray Diffraction (XRD)

X-Ray diffraction was used to study the composition and microstructure properties of blocks, powder or thin films, which is based on Bragg's law. During the operation, a monochromatic X-ray beam is firstly produced and struck on to the surface of the samples at a Bragg angle (θ), following the diffraction of the incident beam by the atomic planes of crystalline sample. Then the diffracted beam is received by a detector, which is moving at different angles (the reflections are observed only when n is an integer); the d-spacing can then be measured. This is deduced from the Bragg's equation:

$$n\lambda = 2d\sin\theta$$

where n is an integral number, λ is the wavelength of the incident X-ray beam, d is the inter-atomic spacing, θ is the Bragg angle which is the angle between the incident beam and the planes of the lattice.

X-ray diffraction (XRD, Bruker D8 with Cu Kα=0.154 nm) (Figure 4.3) was used to collect the diffraction data of as-materials and ball-milled samples over a range of 5-90^{o}.

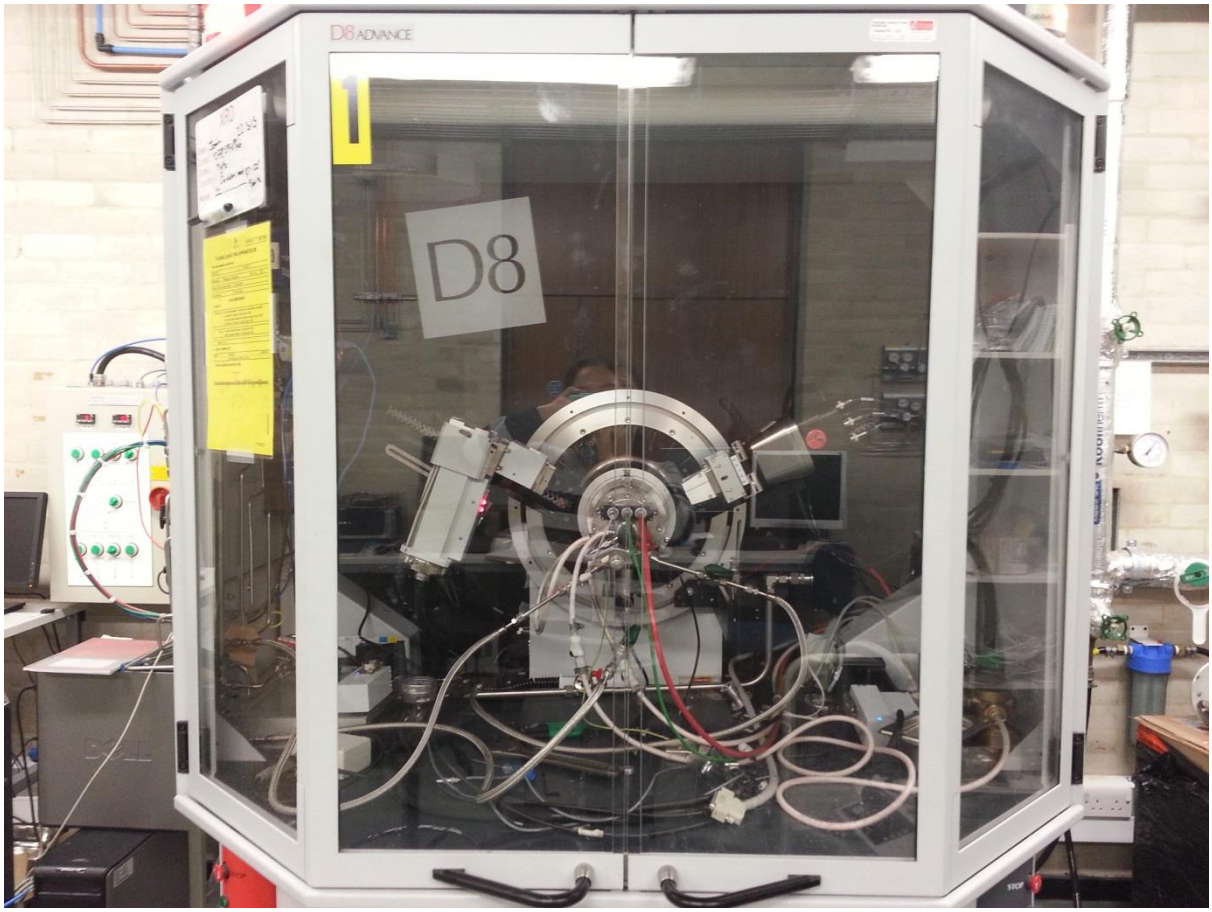

Figure 4.3 X-Ray Diffractometer (Bruker D8 with Cu Kα=0.154 nm)

For room temperature XRD detection, samples were loaded in an argon flow glovebox, onto a sample holder and then sealed by a transparent silica dome to avoid air contact.

In-situ XRD was used to study the compositional and microstructural changes with temperature. An Anton Paar XRK900 cell, in which the samples were heated to certain temperatures under helium flow (100 ml/min, 3.0 bar), was used. The diffraction pattern data was collected isothermally when the sample reached the target temperature.

4.2.2 Differential Scanning Calorimetry (DSC)

A Netzsch "*DSC 204 HP Phoenix*" high-pressure DSC was used to measure the thermodynamic properties of samples. In a heat-flux DSC, the reference and sample are heated at the same power, the ΔT (difference of temperature) between the reference and the sample is detected and converted to a ΔQ (difference of heat) value using a heat flux equation. From this, the relationship between the enthalpy change and the temperature and time can be represented. The apparatus is installed inside an argon flow glovebox, to try to prevent contact of the sample with air.

4.2.3 Raman Spectrometry

Raman Spectroscopy is used to analyse the bonding types within the samples by irradiating the sample with a monochromatic light from infrared to ultraviolet. The incident light, which is generated by a laser, can form a short-lived “virtual state” by exciting the electron cloud surrounding the nuclei. The “virtual state” is not a stable state and can decay back to ground state or vibrational state with the emission of a photon. Usually, there are two kinds of scattering depending on the difference of energy between the emitted and incident photon, which is elastic scattering (Rayleigh) and inelastic scattering (Raman). Raman scattering can also be divided into two different types: stokes scattering and anti-stokes scattering, according to the energy of the emitted photon. In stokes scattering, the emitted photon has less energy than the incident photon because it is from the excitation of the ground state. It is mostly observed at room temperature.

A Renishaw InVia Reflex Raman Spectrometer (Figure 4.4) was used to perform the measurements at a wavelength of 488 nm / 633 nm, the laser was focused through x20 objective with a power of 2 mW, supporting a spot size of 20 μm. Samples were loaded into an Instec HCS621V cell in an argon flow glovebox to try to prevent oxidation. All the Raman spectrum measurements were at room temperature.

Figure 4.4 Renishaw InVia Reflex Raman Spectrometer

4.2.4 Mass Spectrometry (MS)

Mass Spectrometry was used to analysis the released gases from the samples during heating in TGA. Mass Spectrometry works in four stages (ionisation, acceleration, separation and detection), and scans a range of mass to charge (m/z)

ratios. The specific m/z value can be monitored to analyse the relative quantity of given gases. A Hiden Analytical Mass Spectroscopy HAL VII was used for this measurement.

4.2.5 Thermal gravimetric analysis (TGA)

Thermal Gravimetric Analysis (TGA) monitors the change in sample mass with respect to temperature. Mass Spectrometry (MS) was used to monitor the gases desorbed from the sample during the experiment.

To account for the influences from the changes of temperature, gas buoyancy, convection currents in the reacting system, a baseline (with no sample) is measured before each measurement of samples. The baseline measurement is then subtracted from each sample measurement.

The Netzsch TG209 was used to monitor the mass loss of the samples during heating. Samples were heated from 30 °C to a pre-set temperature (400 °C, 650 °C or 950 °C) at 2 °C/min. The TGA is installed inside a glovebox with 1 bar argon flowing at 40 ml/min.

5 Results and Discussion

5.1 Milled graphite

5.1.1 Characterization

5.1.1.1 Room temperature Raman spectra of as-received and milled graphite

Figure 5.1 shows the Raman spectra of as-received graphite. There are two main peaks (G and G` band) at 1572 $cm^{-1}$ and 2709 $cm^{-1}$ which are typical for polycrystalline graphite (Tuinstra 1970, Zhang 2009). While the D and D` bands at 1352 cm^{-1} and 1615 cm^{-1}, are due to defects within the graphite as a result of milling. It is found that the intensity of the D band increases but the intensity of the G band decreases with increased milling time (comparison of spectra c and d) or higher milling speed (comparison of spectra b and c). This is because a longer milling time can introduce more defects into the graphite (Orimo, Majer et al. 1999). The results in Figure 5.1 (b and c) indicate that a higher milling speed can also lead to more defects being introduced into the graphite, which corresponds to the study of (Kano and Saito 1998).

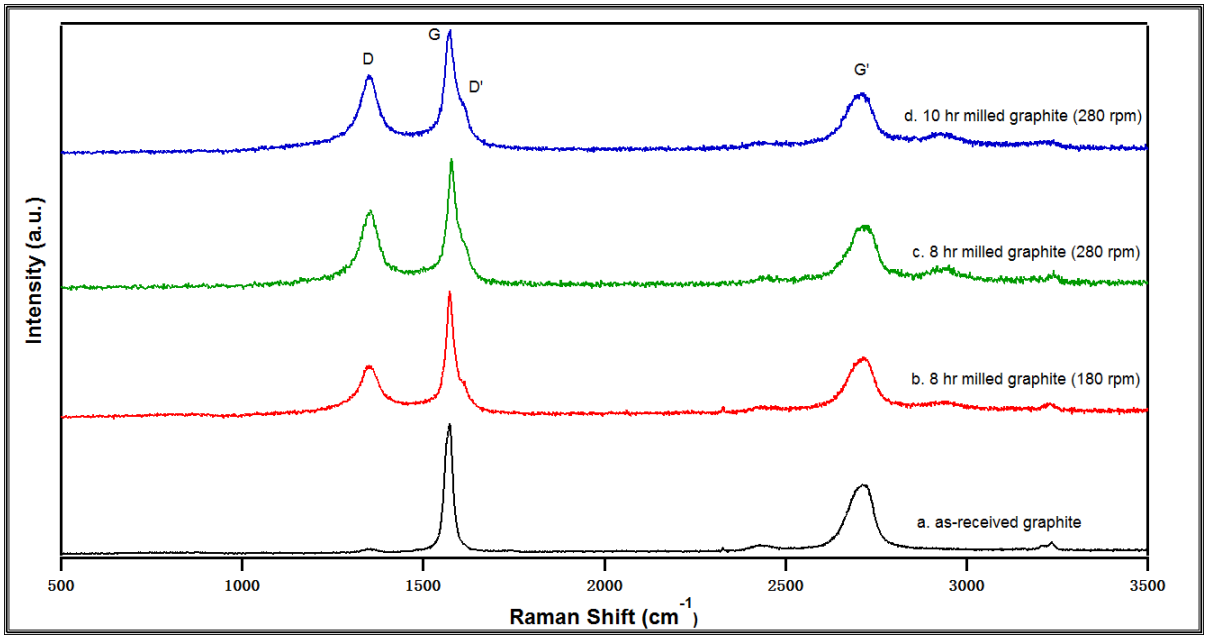

Figure 5.1 Raman Spectra of (a) as-received graphite; (b) and (c) 8 h milled graphite at a milling speed of 180 rpm and 280 rpm, respectively; (d) 10 h milled graphite; milling was under 3 bar hydrogen.

A method was introduced to analyze the crystalline size of graphite, which has been referred to as the La value (Ferrari and Robertson 2000). La is the in-plane correlation length of graphite and it can be estimated from the following equations:

$$\frac{I(D)}{I(G)} = \frac{C(\lambda)}{La} \qquad (La \geq 2\ nm) \qquad (1)$$

$$\frac{I(D)}{I(G)} = C`(\lambda) La^2 \qquad (La < 2\ nm) \qquad (2)$$

where I(D)/I(G) is the ratio of the intensities of the D and G Raman peaks, C(λ)=4.4 nm (λ=488 nm).

Table 5.1 In-plane crystalline size (La) of as-received graphite, graphite ball-milled for 8 h at 180 rpm and 280 rpm, and graphite ball-milled for 10 h (under 3 bar hydrogen).

	As-received graphite	8 h milled graphite 180 rpm	8 h milled graphite 280 rpm	10 h milled graphite 280 rpm
La (nm)	127.2	11.2	6.6	6.3

Table 5.1 shows the La value of as-received graphite, 8 h milled graphite at two speeds (180 and 280 rpm) and 10 h milled graphite. It is clear that a higher milling speed and longer milling time result in a smaller La value, which suggests more defects and a greater proportion of amorphous material. The obtained La value of as-received graphite is smaller than the previous literature report (La=275 nm for the as-received graphite) (Zhang and Book 2011), probably because the as-received graphite are from different companies. However, the values of the milled graphite are similar to the previously reported values (Zhang and Book 2011).

5.1.1.2 Room temperature XRD of as-received and milled graphite

Room temperature (RT) XRD was carried out on as-received and as-milled graphite samples. Figure 5.2 shows the XRD patterns of as-received graphite and graphite milled for 8 hours and 10 hours under 3 bar hydrogen at a milling speed of 280 rpm. The (002) inflection peak located at 26.44° is found in as-received graphite. With increased milling time, the (002) peak shifts position and becomes broader, which agrees with the reports of (Shen, Ge et al. 1996, Orimo, Majer et al. 1999).

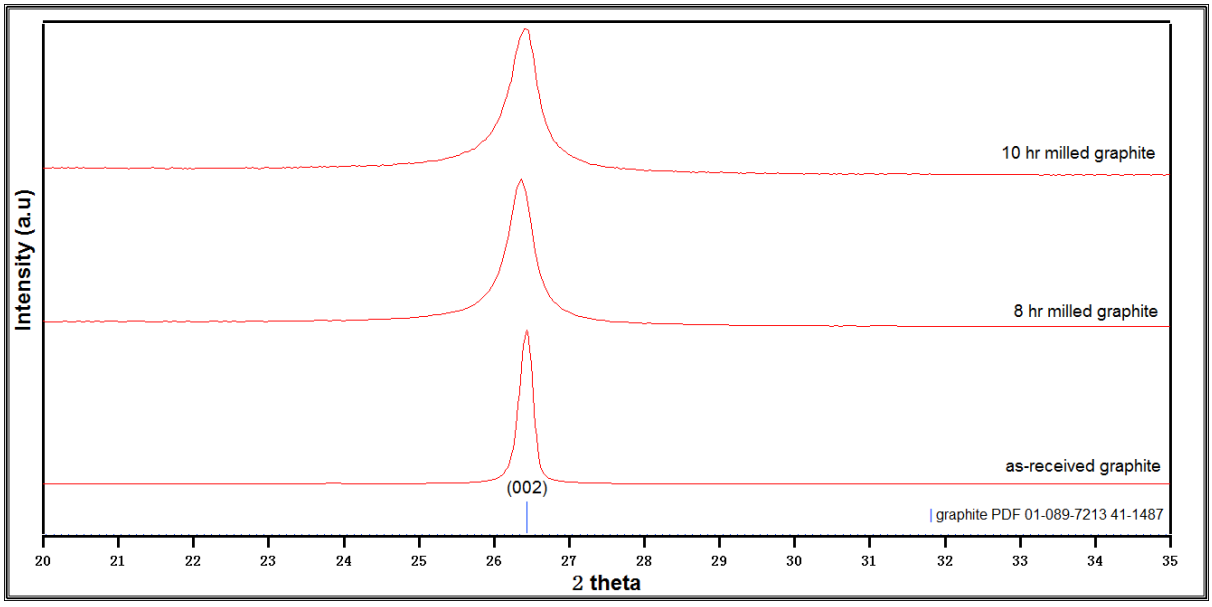

Figure 5.2 XRD patterns of as-received graphite and milled graphite for 8 & 10 hours (3 bar hydrogen, 280 rpm), all the measurements were performed at room temperature.

It was reported that the (002) peak can be influenced by two elements (Shen, Ge et al. 1996), one would be from the relatively ordered graphite crystal (corresponding to the G peak in a Raman spectrum) and another one would be introduced from defects of graphite (corresponding to the D peak in section 5.1.1.1). The (002) peak position shifted to 26.36° for the 8 h milled graphite, which is slightly lower than the peak position for as-received graphite. This indicates that the graphite interlayer has expanded during milling, which corresponds to the study of (Orimo, Majer et al. 1999).

5.1.2 Thermal Decomposition

In order to understand the thermal properties of the milled sample, the 10 h milled graphite under 3 bar hydrogen was heated from 30 °C to 950 °C at a heating rate of 2 °C/min with Ar flow in TGA and the released gases were detected by mass spectroscopy.

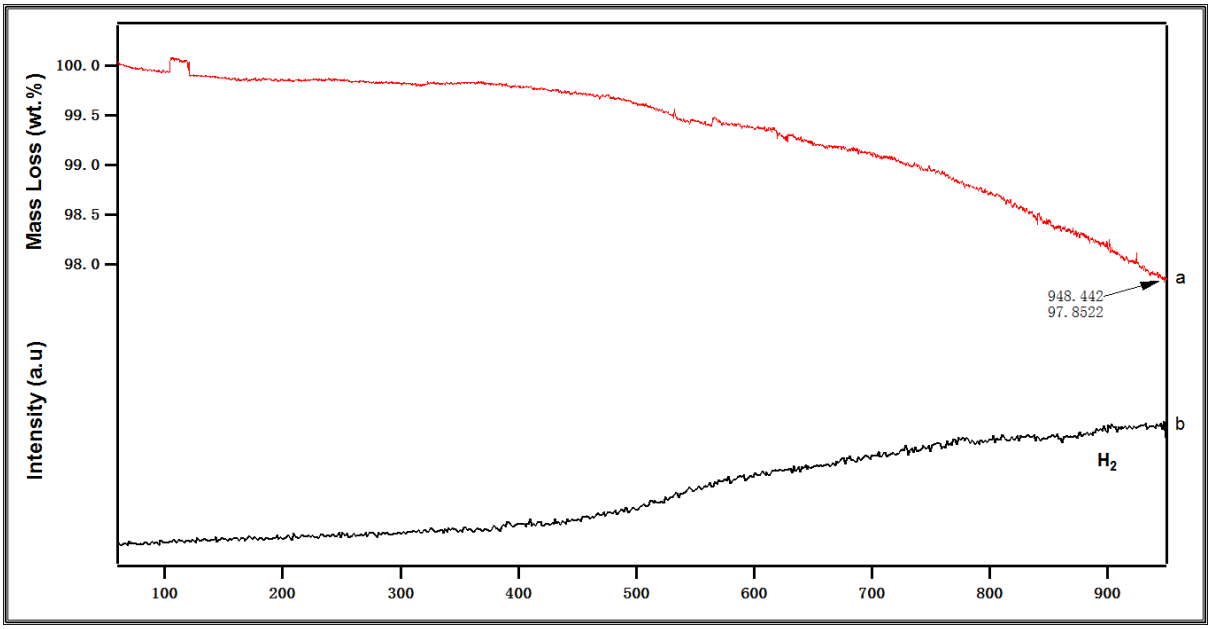

Figure 5.3 Mass Loss (a) and Mass Spectrum (b) of the 10 h milled graphite under 3 bar hydrogen, heated at 2 °C/min with an Ar flow (100 ml/min).

Figure 5.3 shows the desorption properties of 10 h milled graphite: nearly 2.15 wt. % mass loss was obtained at the end of heating process. From the mass spectrometry plot (black line b), only hydrogen was detected; no other gas was detected. This corresponds with the results of (Zhang and Book 2011), but the quantity of released hydrogen is much smaller than the previous result of 5.5 wt. %. This may be because of the different source for the graphite or the different milling conditions. The onset temperature of released hydrogen is over 350 °C, which is much higher than the temperature for physisorbed hydrogen. The intensity of hydrogen in the mass spectrum (black line b in Fig. 5.3) is still large until 950 °C, which indicates that some hydrogen is still stored in the milled graphite and so may release at an even higher temperature. Therefore, in fact, the hydrogen storage capacity of 10 h milled graphite could be more, higher than 2.15 wt. %. (There is a sharp rise between 102 °C to 121 °C in Figure 5.3 a, which is caused by equipment deviation).

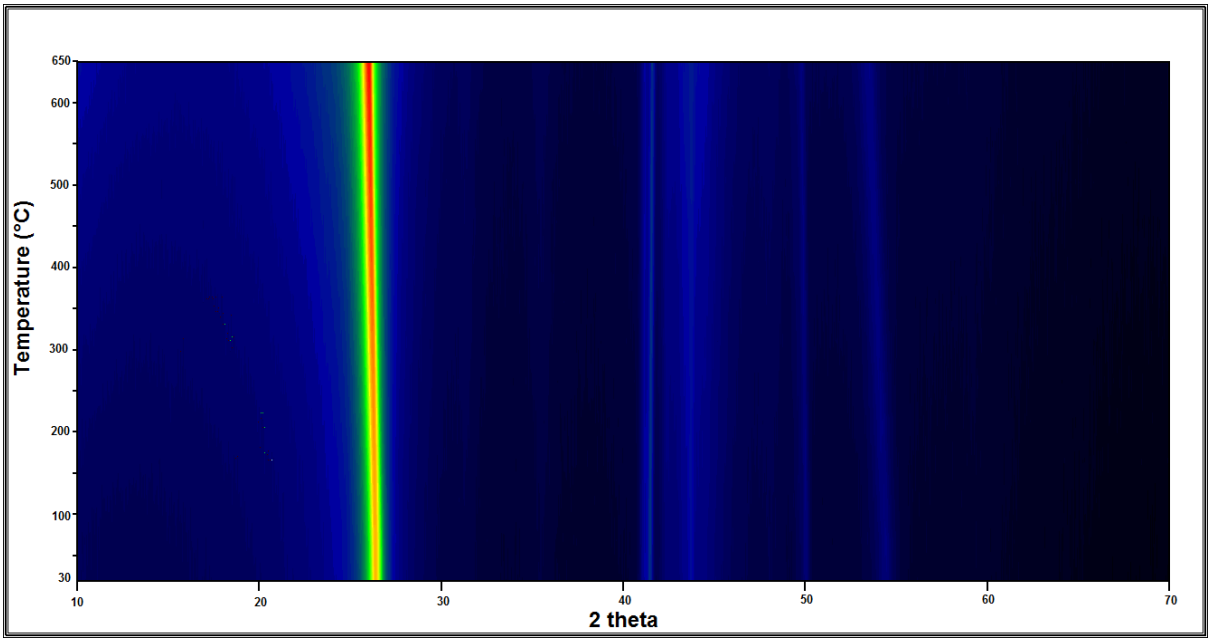

Figure 5.4 in-situ XRD of 10 h milled graphite heated to 650°C from 30°C with a heating rate of 2 °C/min under helium flow (100 ml/min); the colour is relative to the peak intensity, black means the minimum and red is the maximum.

In-situ XRD was also performed on 10 h milled graphite to find the lattice changes during heating, the sample was heated to 650 °C with a heating rate of 2 °C/min and helium flow. Figure 5.4 shows the in-situ XRD measurements of 10 h milled graphite from 30 °C to 650 °C, the peak located at 26.42° corresponding to the (002) peak of graphite, the peak position shifts continuously to lower 2θ degree until 26.03° after heating to 650 °C, which indicates that the graphite interlayer expanded. This is consistent with the jEdit-Topas analysis of the lattice parameters of the in-situ sample which is shown in Figure 5.5, where the lattice volume slightly increases with increasing temperature.

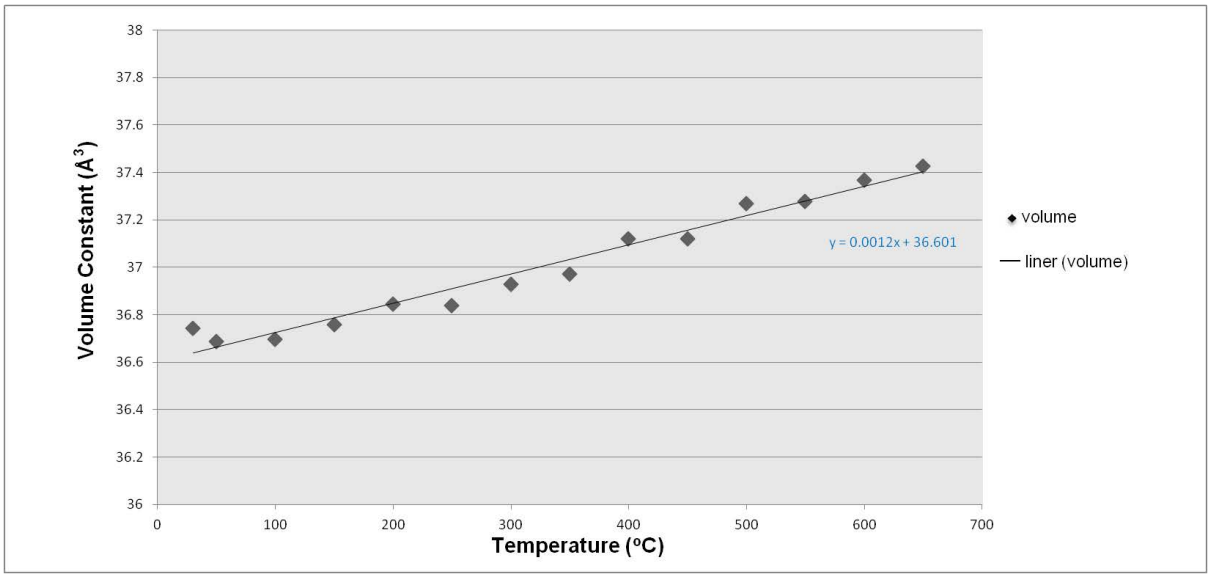

Figure 5.5 The variation of lattice volume (±0.01 A^3) of 10 h milled graphite during in-situ XRD measurements, heated up to 650 °C, 2 °C/min.

5.1.3 Discussion of the mechanism

According to (Zhang 2011), hydrogen atoms can combine with carbon atoms in four steps (C*+H*→CH*; CH*+H*→CH_2*; CH_2*+H*→CH_3*; CH_3*+H*→CH_4*). The first two steps were considered to be the formation of dangling bonds between hydrogen and carbon atoms, and the following two steps require a higher ball-milling input energy. For the graphite milled up to 10 hours, only the first two steps were proposed to occur, because only hydrogen was detected during heating (corresponding to Figure 5.3). The last two steps were reported to occur in graphite milled more than 10 hours for there was methane released with hydrogen.

Milling is an effective technique to produce amorphous or nanocrystalline phases within graphite. The increased ratio of D band to G band, shown in Figure 5.1, suggests an increased ratio of sp^3 to sp^2 bonding. This may be explained by hydrogen atoms being absorbed onto graphite edges and/or between the interlayers

of graphite (Chambers, Park et al. 1998, Zhang 2009). Combined with the results in Figure 5.2 showing the (002) peak shift after milling, this indicates that the interlayer distance of graphite has been expanded. This may indicate that hydrogen can be stored between graphite interlayers

From the results of the TGA-MS and in-situ XRD measurements (Figures 5.3, 5.4 and 5.5) the milled graphite desorbed hydrogen during heating with an increased lattice volume and extended interlayer distance. The possible reason for the expansion of interlayer would be thermal expansion. It may be that the hydrogen absorbed on the edge is easier to desorb than that absorbed between the layers, as less desorption energy would be required.

5.2 2Graphite + $LiNH_2$

In order to understand the hydrogenation or dehydrogenation mechanism(s) of a composite of $LiNH_2$+LiH+graphite, it is helpful to know the hydrogen storage properties of the as received materials and the mixture of $LiNH_2$+graphite, LiH+graphite and $LiNH_2$+LiH. As the properties of graphite+LiH composite were already discussed in Section 2.4.1, the dehydrogenation properties of graphite+$LiNH_2$ composite will now be investigated. The as-prepared graphite+$LiNH_2$ composite was milled for 2 h under 3 bar H_2 with a molar ratio of 2(8 h milled graphite) to 1($LiNH_2$).

5.2.1 Characterization

5.2.1.1 Raman Spectrum of as-received $LiNH_2$ and as-prepared graphite+$LiNH_2$ composite

Room temperature Raman spectroscopy was performed on as-received $LiNH_2$ and as-prepared graphite+$LiNH_2$. In Figure 5.6a, the D (1363 cm^{-1}) and G (1572 cm^{-1}) peaks, correspond to milled graphite (Section 5.1.1). Because the graphite used in the formation of the composite graphite+$LiNH_2$ (2:1) was first milled for 8 hours and then milled with $LiNH_2$ for 2 hours, the total milling time for the graphite in the composite is equivalent to 10 hours. This means that the influence of $LiNH_2$ on graphite can be studied by comparing the experimental data of the composite graphite+$LiNH_2$ with the data of 10 hours milled graphite. The La value the graphite+$LiNH_2$ (2:1) composite was calculated using Equation (1) to be 24 nm, which is much larger than the 6 nm value for 10 h milled graphite. This indicates that the amount of disordered phases in the graphite reduced after milling with $LiNH_2$ for two hours.

There is also a small peak at 1084 cm^{-1} in graphite+$LiNH_2$, which is not observed in either the as-received $LiNH_2$ or the 10 h milled graphite. It may be induced by oxides, but further analysis is needed to better understand this. A small peak appeared at 3655 cm^{-1} in graphite+$LiNH_2$, which is similar to the small peak at 3665 cm^{-1} in as-received $LiNH_2$: a 10 cm^{-1} shift in peak position is observed, but the reason for this is currently unknown (this might be because of milling/stress).

Figure 5.6b is a higher resolution of the 3000-3600 cm^{-1} section of Figure 5.6a, the three main peaks in as-received $LiNH_2$ at 3262, 3314 and 3324 cm^{-1} are not observed in the graphite+$LiNH_2$ composite. The Raman spectrum of $LiNH_2$ has been

reported to include peaks at around 3261, 3313 and 3326 cm^{-1} corresponding to the N-H stretching modes of the NH_2 ion (Bohger, Eßmann et al. 1995, Anderson, Chater et al. 2011).

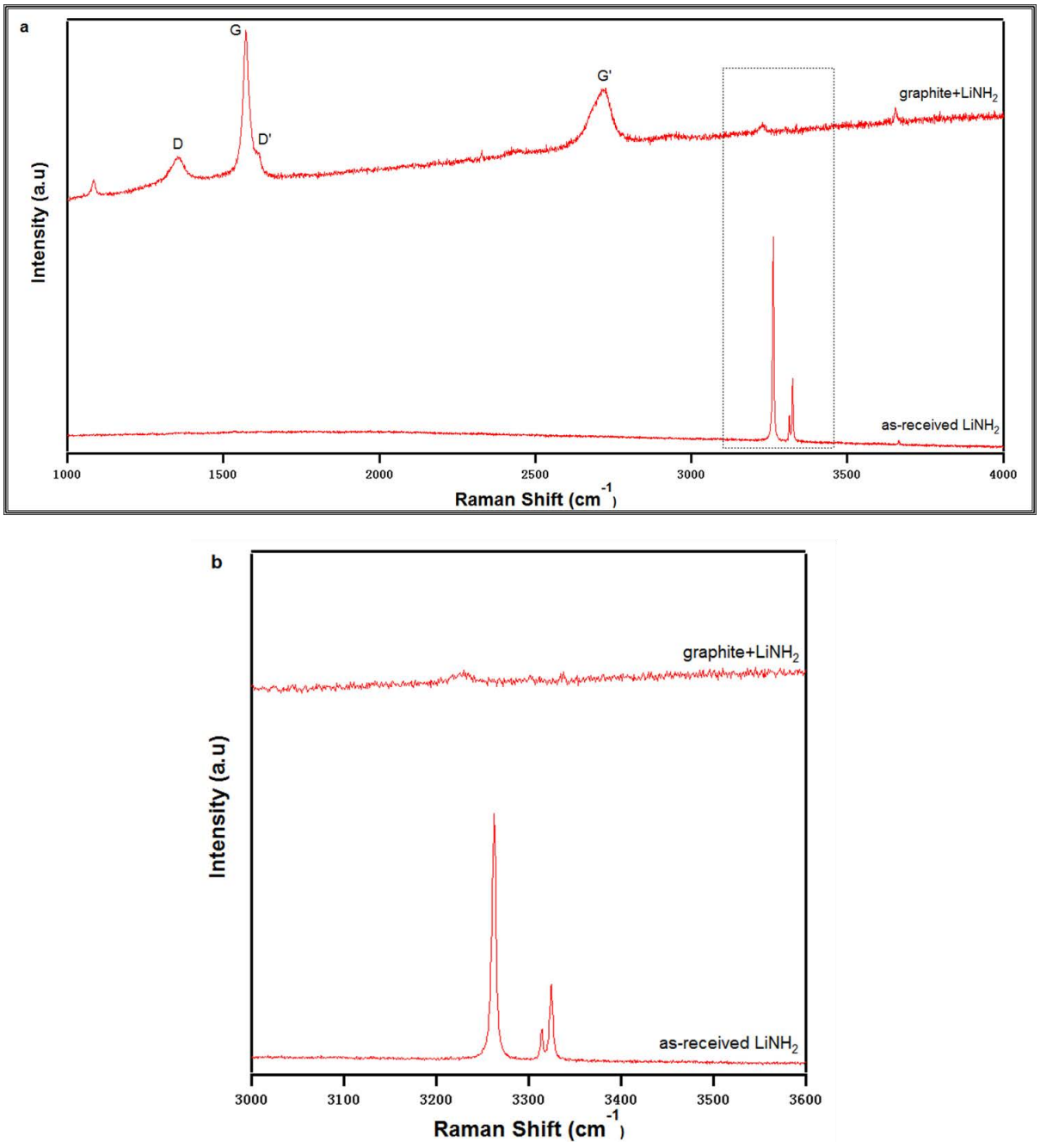

Figure 5.6 a: Room temperature Raman spectrum of as-received $LiNH_2$ and composite of graphite+$LiNH_2$; b: higher resolution of the 3000-3600 cm^{-1} section for as-received $LiNH_2$ and composite graphite+$LiNH_2$.

5.2.1.2 Room temperature XRD of as-received $LiNH_2$ and the composite of graphite+$LiNH_2$

XRD for the 2 h milled graphite+$LiNH_2$ sample (Figure 5.7) shows reflections corresponding to $LiNH_2$ and graphite. Except for a small peak at 33.7° which corresponds to Li_2O, no other peaks were observed. The appearance of Li_2O shows that the sample may be oxidized. The oxygen may have been introduced by the as-received materials or during sample transfer and hydrogen charging processes,.

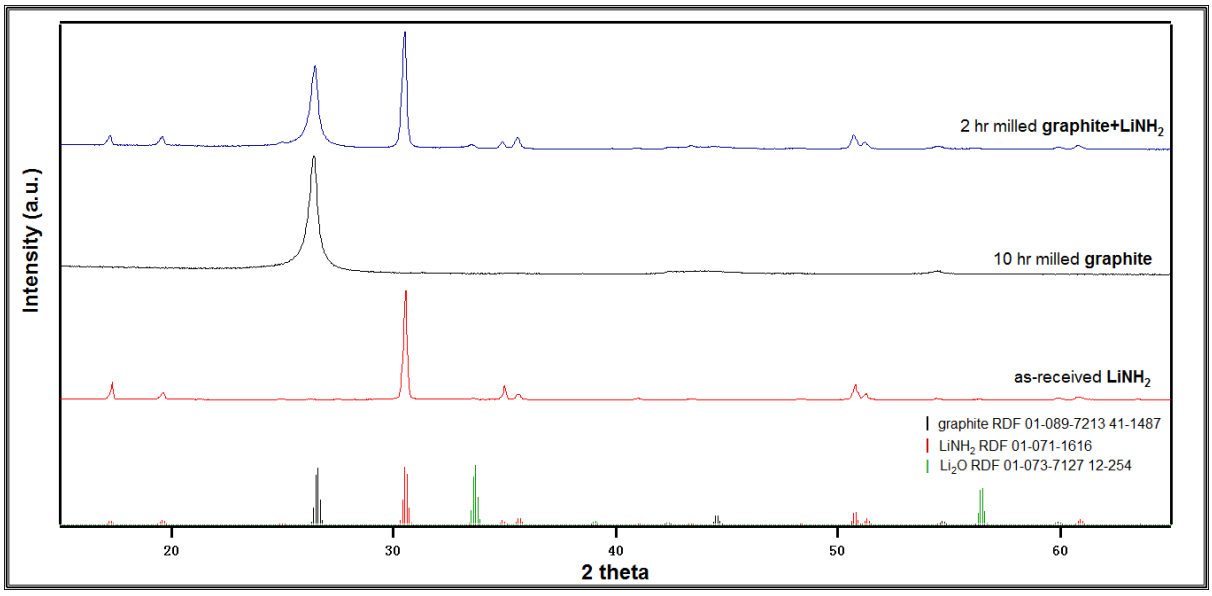

Figure 5.7 Room temperature XRD patterns of as-received $LiNH_2$, 10 hours milled graphite and 2 h milled composite graphite+$LiNH_2$.

5.2.2 Thermal Decomposition

The thermal decomposition of $LiNH_2$ is shown in Fig. 5.8. The effect of graphite addition was further investigated on the thermal decomposition of graphite+$LiNH_2$ (2:1) composite in Fig. 5.9. TGA-MS measurement was performed on as-received $LiNH_2$ with a heating rate of 2 ℃ /min under Ar flow (100 ml/min) (heating range

30 ℃ to 400 ℃). The composite of graphite+$LiNH_2$ (2:1) was measured under the same conditions.

5.2.2.1 TGA-MS measurement of as-received $LiNH_2$

Figure 5.8 gives the mass loss changes during heating in TGA (red line) and the signals introduced by the released gases (blue and black line). It is clear that a large signal of ammonia (blue line) is detected with an onset temperature at about 250 ℃ , which is consistent to the results of (Pinkerton 2005). The signal of ammonia firstly increases slightly until 340 °C and goes up dramatically to a peak temperature of 348.9 °C, following a short decline and then rising up again at 354.3 °C to 361.8 °C. A small amount of hydrogen with a peak temperature of 345.9 °C was also observed during heating which is shown as a black line in Figure 5.8. These results correspond to those of (Ichikawa, Isobe et al. 2004) which were reviewed in Section 2.5.2.1.

As mentioned in Section 2.5.2.1, ammonia is released from the decomposition of $LiNH_2$ with the formation of Li_2NH. The small amount of hydrogen may come from the decomposition of NH_3. In total, 14.5 wt. % mass loss is achieved after heating (Figure 5.8 red line), and mostly as ammonia. According to the research of (Varin, Jang et al. 2010), the decomposition of $LiNH_2$ during heating can be divided into two steps by the phase transition of $LiNH_2$ from solid state to liquid state. It is believed that NH_3 is released relatively slowly when $LiNH_2$ is in the solid state comparing with when $LiNH_2$ is in the liquid state. Therefore, under these conditions: the amount of hydrogen is not estimated as the MS signal peaks are too small; and 3.0 wt. % and 11.6 wt. % NH_3 is released from solid $LiNH_2$ and from liquid-state $LiNH_2$, respectively.

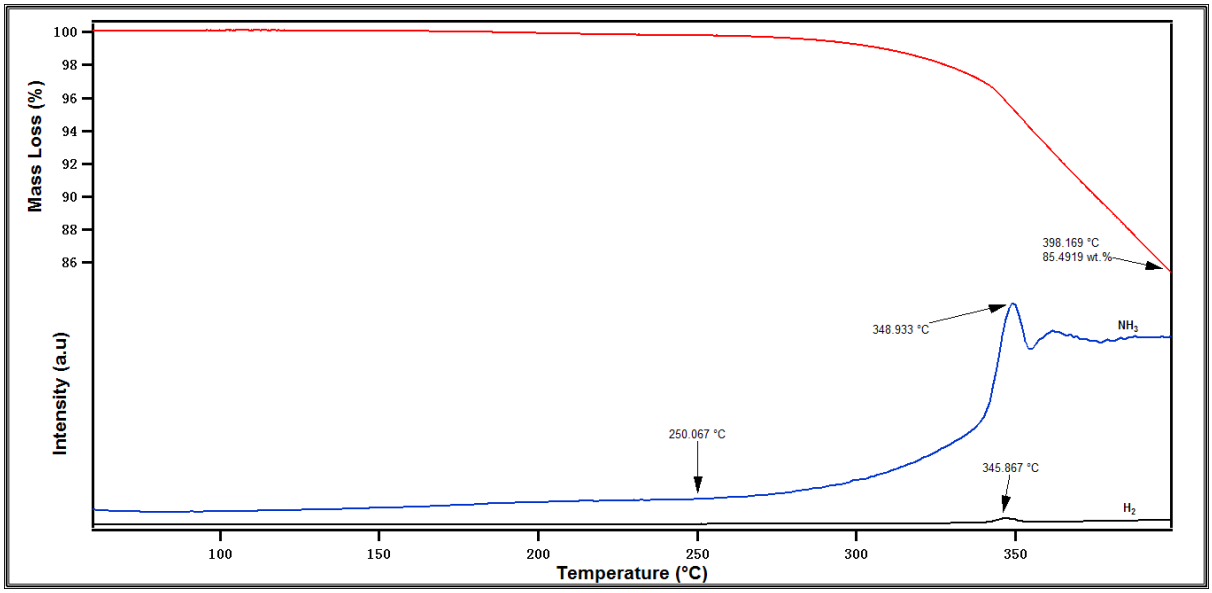

Figure 5.8 TGA-MS measurement of as-received $LiNH_2$, the sample was heated from 30 °C to 400 °C at 2 °C/min, Ar flow (100 ml/min).

5.2.2.2 DSC, TGA-MS measurement of composite of 2 h milled graphite+$LiNH_2$ (2:1)

From the TGA-MS plot in Figure 5.9, 12.7 wt. % gases are released from the graphite+$LiNH_2$ (2:1) composite, which are detected by MS to be NH_3, NH_2 and H_2. The NH_2 may be a fragment of the NH_3 mass spectrometry signal. By quantitative analysis of the MS peak area data, the released hydrogen contributes 4.6 wt. % and ammonia 8.0 wt. %.

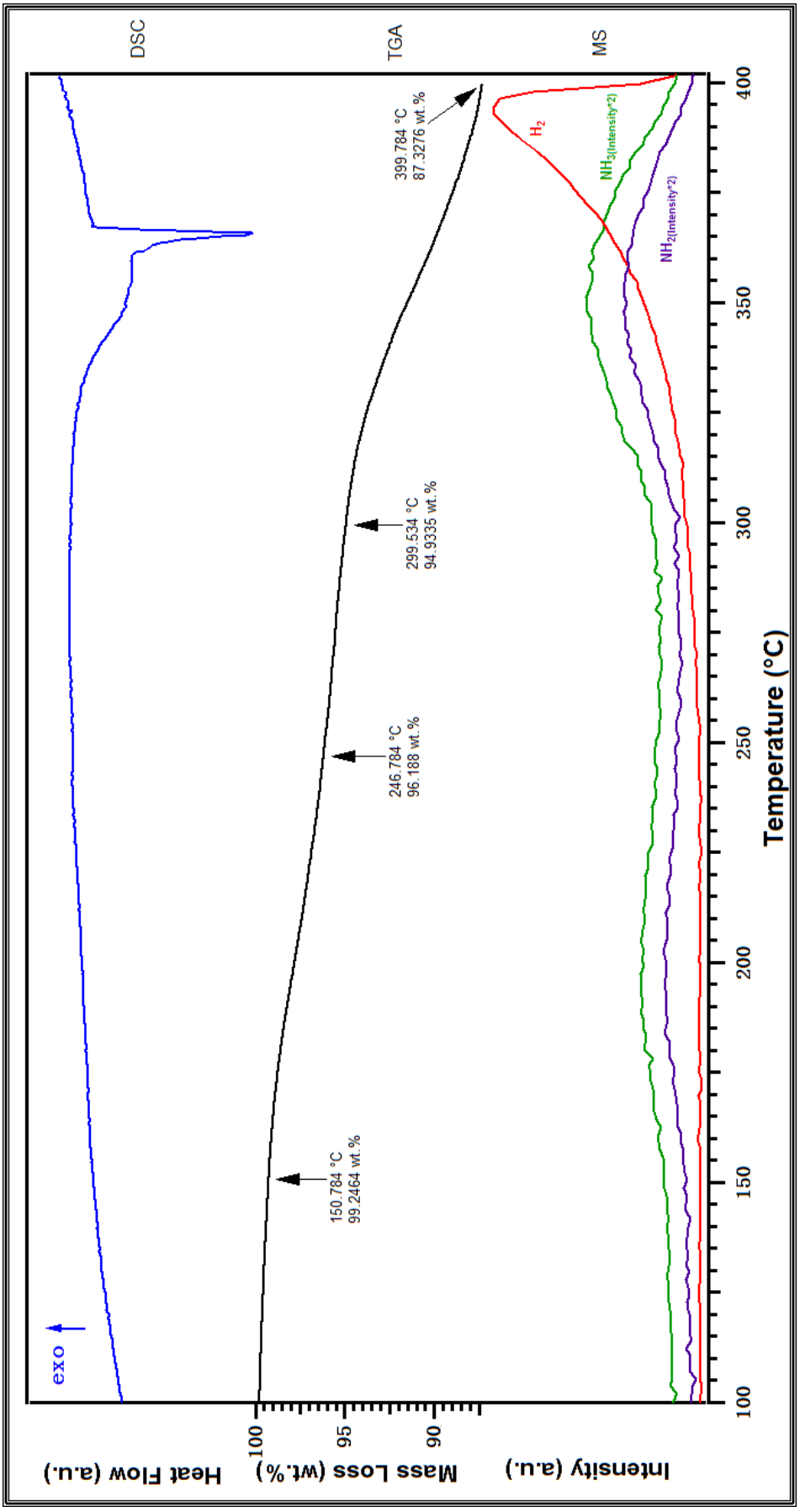

Figure 5.9 DSC, TGA and Mass Spectrometry (MS) measurements of 2 h milled graphite+$LiNH_2$ (2:1), the sample was heated from 30 °C to 400 °C with a heating rate of 2 °C/min under Ar flow (100 ml/min).

DSC was also used to measure the decomposition properties of the composite as shown in Figure 5.9. There is a broad peak at 352.2 °C with a sharp peak at 365.8 °C: this corresponds to the results of (Varin, Jang et al. 2010) which showed the melting of $LiNH_2$.

XRD was performed on dehydrogenated (dehydrogenation was carried out between room temperature to 400 °C) composite of graphite+$LiNH_2$ (2:1). From Figure 5.10, it can be seen that the sample was partially oxidized, by the appearance of LiOH and Li_2O. Apart from graphite, only LiH is found in this XRD pattern. This is quite different from the results of Leng, Ichikawa et al (Leng, Ichikawa et al. 2005) (shown in Figure 2.21), in which they measured the thermal decomposition of as received $LiNH_2$ and found that only Li_2NH was left in the solid state. This difference could be due to the addition of hydrogenated graphite and/or to the hydrogen stored in the milled graphite.

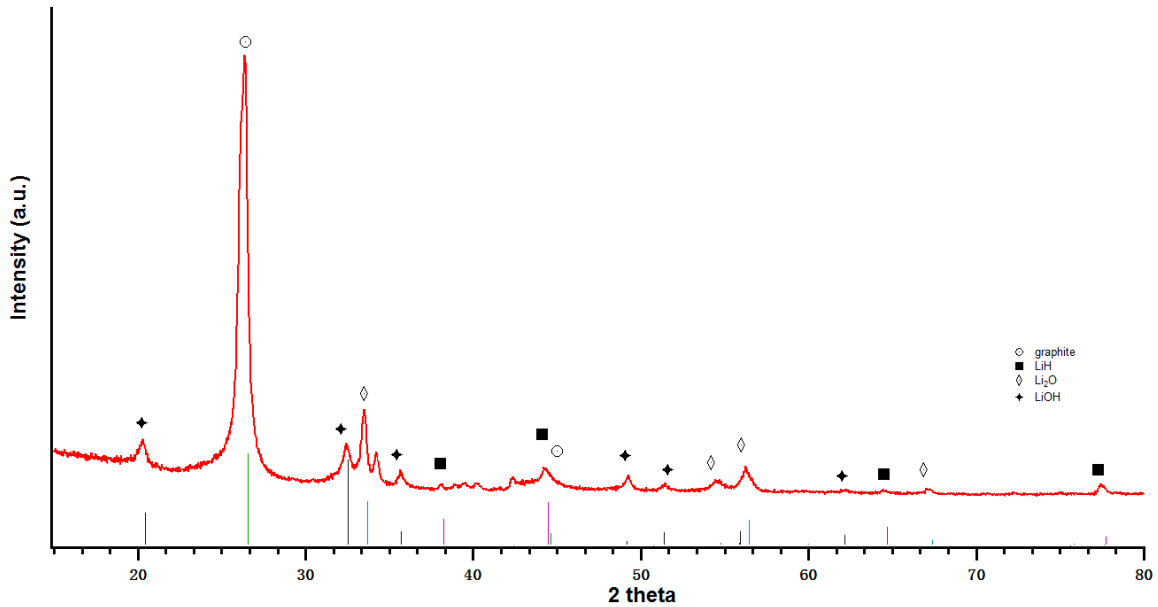

Figure 5.10 Room temperature XRD pattern of 2graphite+$LiNH_2$, after it was heated in an IGA from room temperature to 400 °C at 2 °C/min under vacuum.

As discussed above, the amount of NH_3 is reduced to 8.0 wt. % and hydrogen increased to 4.6 wt. % after graphite is added. There could be three explanations:

1. reaction of NH_3 and C. However, if the reaction $NH_3+C=HCN+H_2\uparrow$ occurred then HCN should be found in by XRD. But no HCN is observed in Figure 5.10.
2. hydrogen still remains in the hydrogenated heated graphite.
3. some $LiNH_2$ powders are covered by graphite powder during ball-milling, which reduces the activity of the $LiNH_2$. This can be supported by the Raman spectrum in Figure 5.6, no special peak for $LiNH_2$ is found in composite graphite+$LiNH_2$ (2:1), the total mass loss is also smaller than for as-received $LiNH_2$. However, this is not a perfect explanation because it cannot explain where the hydrogen comes from.

If the hydrogen is from the H atoms stored in the milled graphite, the mechanism of thermal decomposition of the composite of graphite+$LiNH_2$ (2:1) would potentially follow the reaction as below:

$$LiNH_2 + 6\ H_2\,(sol) \rightarrow LiH + NH_3\uparrow + 5\ H_2\uparrow$$

This equation is established according to the new substances which are found in the gas (Figure 5.9) and solid states (Figure 5.10).

As mentioned in Section 2.5.2.1, LiH can react with NH_3 very fast. But LiH still exists in the solid state after heating, and so it does not react with NH_3 to form Li_2NH. Further studies are needed to explain which reaction(s) is occurring.

5.2.3 Summary

The calculated La value shows that the interlayer distance of graphite is enlarged by milling with $LiNH_2$. No characteristic peak of $LiNH_2$ is found in the Raman spectrum (Figure 5.6), which indicates that there could be some structural changes during milling. However, no XRD evidence is found for the formation of new phases.

From the results of the thermal decomposition measurements, Li_2NH is not found after heating graphite+$LiNH_2$ (2:1). In the case that only $LiNH_2$ in the composite reacts during heating, Li_2NH should form after heating, but only LiH is found. This reveals a reverse reaction of the Equation (5) in Section 2.5.2.1. Graphite may take part in the reactions, but the mechanism is still not clear.

5.3 $LiNH_2$ + 1.2LiH

Composite $LiNH_2$+1.2LiH is prepared in the same manner as the composite graphite+$LiNH_2$ (2:1). The molar ratio of $LiNH_2$ to LiH (1:1.2) was selected for its low NH_3 emission which was discussed in Section 2.5.2.2. The $LiNH_2$+1.2LiH composite has already been studied as a potential hydrogen storage material by (Ichikawa, Hanada et al. 2004, Yao, Shang et al. 2007, Varin and Jang 2011) (Takayuki Ichikawa 2004, Yao, Shang et al. 2007, Varin and Jang 2011). However, the NH_3 emission occurring during the dehydrogenation process leads to poor prospects for reversibility in this system. The oxidation of LiH is also a barrier for the $LiNH_2$+LiH system and so for many other systems. It was reported (Varin and Jang 2011, Yoshida, Yoshimura et al. 2011) that the addition of graphite can improve the hydrogen storage property of the $LiNH_2$+LiH system, reduces the amounts of

released NH_3 and protect LiH from oxidation by covering the LiH as a coating. Here the hydrogen storage properties of the $LiNH_2$+1.2LiH composite are studied, followed by the characterization and thermal decomposition properties of the graphite-$LiNH_2$-LiH composite in the next section.

There are three types of $LiNH_2$+1.2LiH composite, which are prepared under different conditions. Two are milled for different milling times (3 and 5 hours) and as received LiH (6 wt. %) is used as starting material. The third composite is milled for 5 h but the starting material is changed to another batch of LiH which is less oxidised, in order to find out the influence of the composition of the as received LiH on the $LiNH_2$+1.2LiH system.

5.3.1 Characterization

5.3.1.1 Raman spectrum of $LiNH_2$+1.2LiH prepared by different milling time and starting material

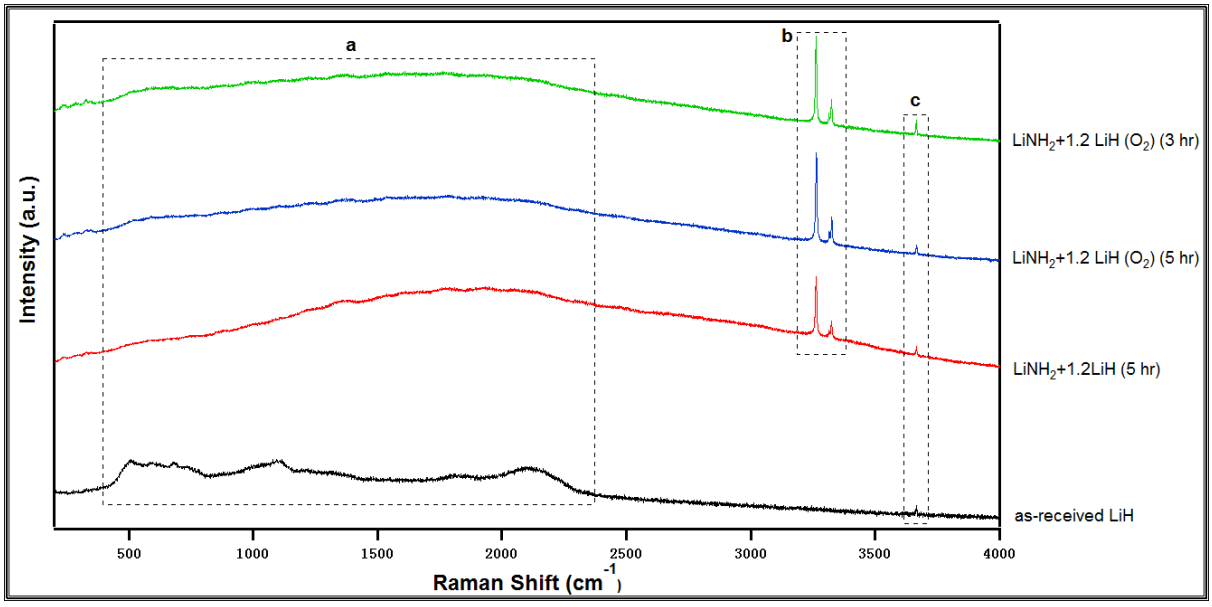

Figure 5.11 Room temperature Raman spectrum of as-received LiH (low oxidation) (black line) and $LiNH_2$+1.2LiH. Two samples are milled for 3 (green line) and 5 hours (blue line), and a higher oxidation level LiH is used as starting material which is shown as LiH (O_2), another sample uses a lower oxidation level LiH and the milling time is 5 hours (red line). The three ranges a, b, c indicate LiH, $LiNH_2$ and Li_2O bondings, respectively.

Room temperature Raman spectroscopy was performed on as-received LiH (low oxidation) and $LiNH_2$+1.2LiH composites prepared by different milling conditions. For as-received LiH, there is no obvious sharp peak in the Raman spectrum (Figure 5.11 black line) but a series of broad peaks are found in the range 390-2386 cm^{-1} (Figure 5.11 a). These broad peaks are also found in both $LiNH_2$+1.2LiH (O_2) (milled for 3 and 5 hours) and 5 h milled $LiNH_2$+1.2LiH. The three composites show peaks around 3263 cm^{-1}, 3315 cm^{-1} and 3325 cm^{-1}, as also observed in received $LiNH_2$ (Figure 5.6 b). These peaks correspond to the N-H stretching modes of the NH_2 ion (Figure 5.11 b).

A small unknown peak located in range c of Figure 5.11 is observed in all the samples. This could be the stretching mode for Li_2O, however no evidence has yet been found from the literature to support this.

The Raman spectra of all the $LiNH_2$+1.2LiH systems, suggest that no new phase is formed by milling. In terms of the influence of the milling conditions, there is not much difference between the 3 h and 5 h milled $LiNH_2$+1.2LiH samples, which indicates that milling time seems does not significantly affect the structure of the composite. Actually, according to (Shaw, Ren et al. 2008), the particle size of the $LiNH_2$+LiH composite increases or decreases dramatically when it is milled up to 150 min, but after 180 min the particle size remains the same (see Figure 2.22) (Shaw, Ren et al. 2008). Compare with the gently peak in range **a** of 5 h milled $LiNH_2$+1.2LiH (O_2), the shape of the peak in range **a** of the 5 h milled $LiNH_2$+1.2LiH which uses less oxidized LiH is more sharp. It seems O_2 may lead to some changes in the composite. However, further investigation is still needed.

5.3.1.2 Room temperature XRD measurements of $LiNH_2$+1.2LiH composites

i. The effect of milling time

As shown in Figure 5.12 (pink line), the as received $LiNH_2$ shows a sharp peak at 30.5°. A similar peak is also found in 3 h and 5 h milled $LiNH_2$+1.2LiH composites, but the peak positions shift to lower 2θ values of 30.4° and 30.4°, which indicates the graphite interlayer distance expanded after ball-milling. What is more, the peaks located at 50.7° and 51.2° become broader after 3 or 5 h milling, as mentioned in Section 2.3, which may suggest increased disorder and/or a reduced grain size.

However, the difference in peak position and peak width between 3 h and 5 h milled samples is not clear. This corresponds to the results of (Shaw, Ren et al. 2008).

ii. The effect of starting material

Two $LiNH_2$+1.2LiH composites are prepared under the same milling conditions, but one of them used oxidized LiH and another one used low oxidized LiH. In Figure 5.12, the XRD pattern of 5 h milled $LiNH_2$+1.2LiH (O_2) shows three substances: $LiNH_2$, LiH and Li_2O. However, Li_2O was not found in the 5 h milled $LiNH_2$+1.2LiH composite.

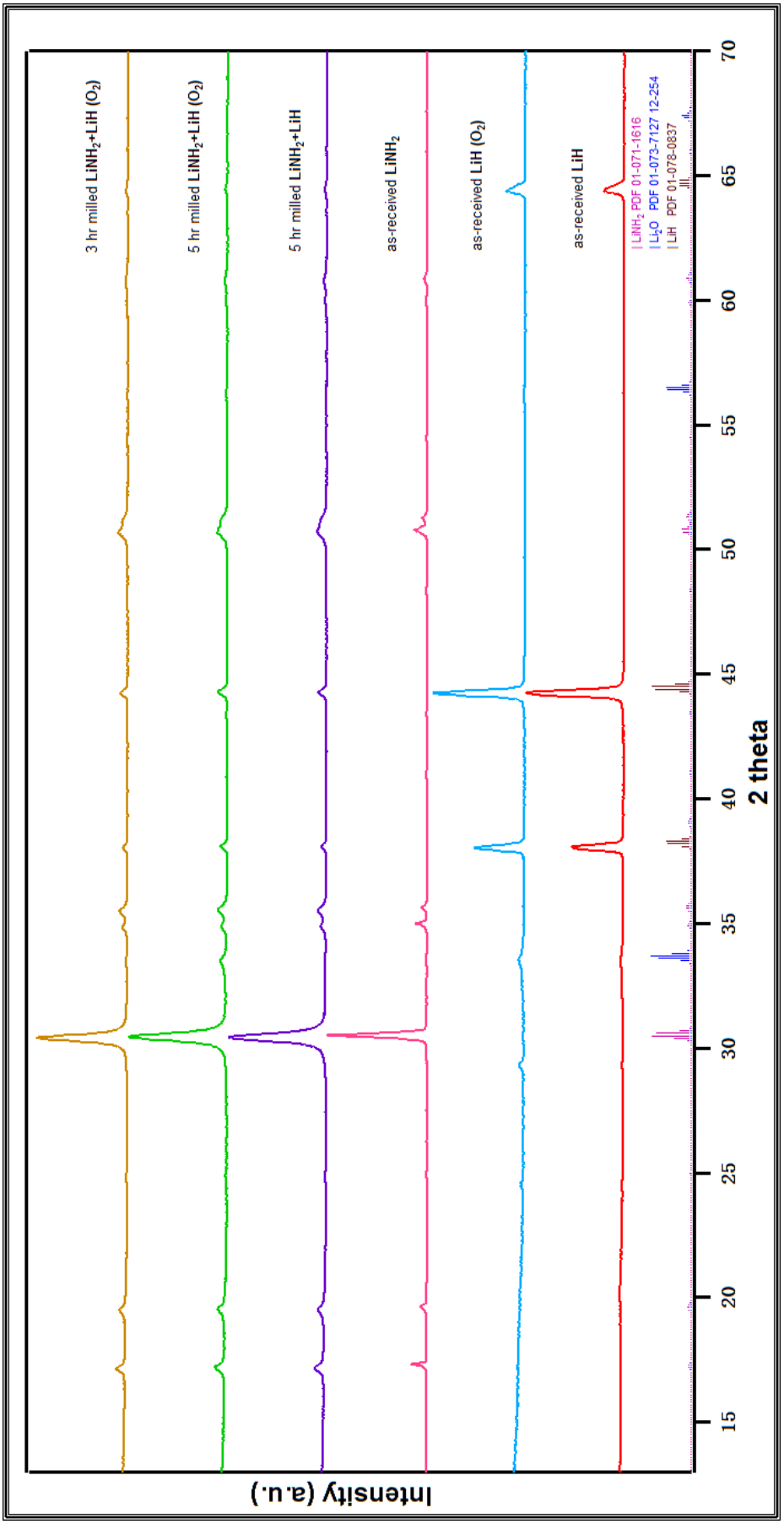

Figure 5.12 Room temperature XRD patterns of as-received LiH (blue line: higher oxidized LiH; red line: lower oxidized LiH), $LiNH_2$ (pink line), 3 and 5 h milled $LiNH_2$+1.2LiH (O_2) (yellow and green line, respectively), 5 h milled $LiNH_2$+1.2LiH (purple line).

5.3.2 Thermal decomposition

In order to study the thermal decomposition properties of the three samples, TGA-MS measurements were performed with the same heating rate (2 ℃ /min), heating range (30-400 °C) and Ar flow speed (100 ml/min).

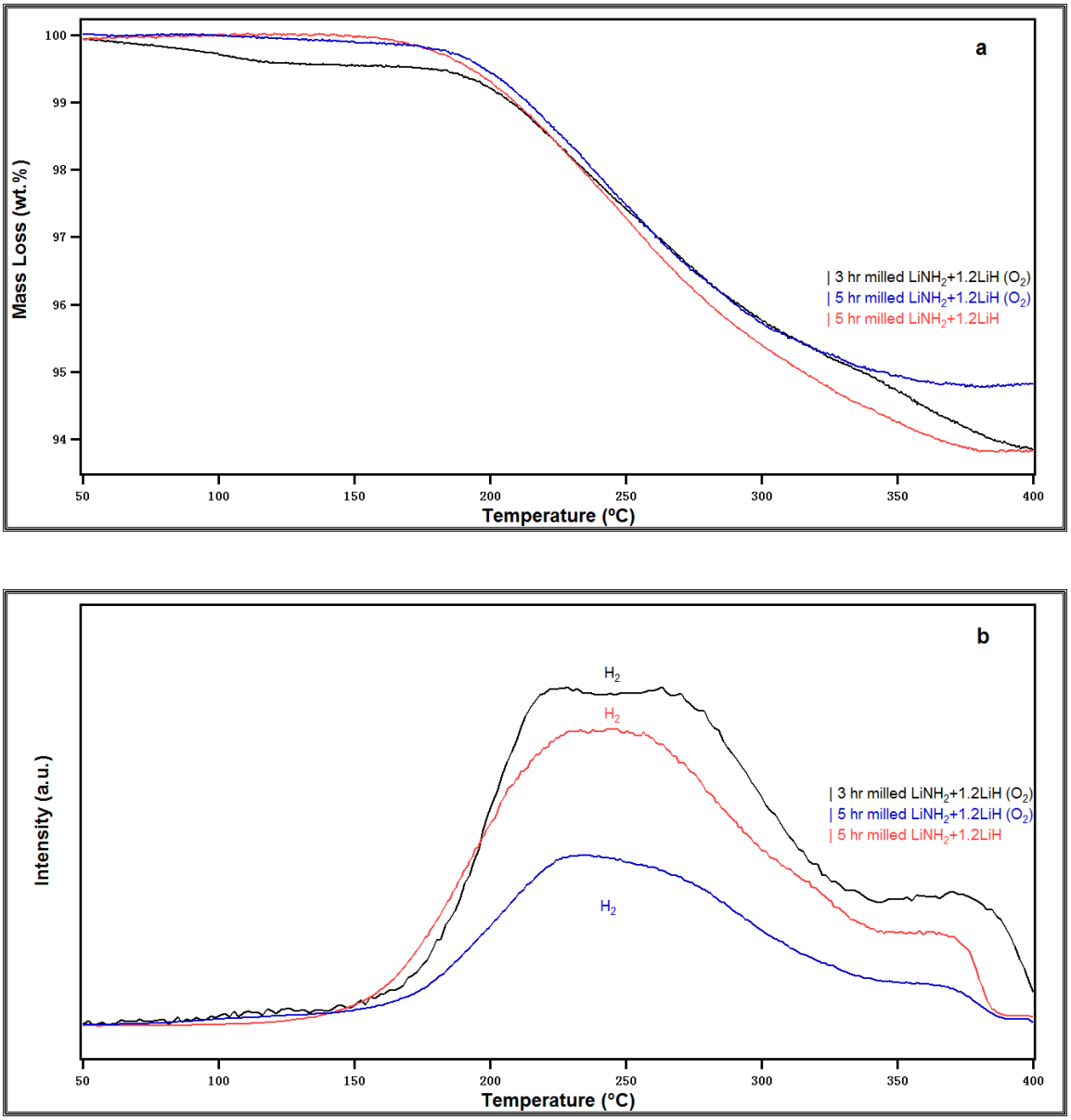

Figure 5.13 Thermal desorption profile (a) and mass spectrum (b) of 3 h and 5 h milled $LiNH_2$+1.2LiH (O_2), 5 h milled $LiNH_2$+1.2LiH when they were heated in TGA from 30 °C to 400 °C with a heating rate 2 °C/min under Ar flow (100 ml/min).

As shown in Figure 5.13b, only H_2 was detected by mass spectrometry for the three samples, which means that the mass loss observed in TGA is all contributed by hydrogen. Figure 5.13a gives the mass loss changes of the three samples during heating. In terms of the 3 h milled $LiNH_2$+1.2LiH (O_2), total 5.7 wt. % hydrogen released after heating to 400 °C. From the mass loss data (the black line) of 3 h milled $LiNH_2$+1.2LiH (O_2) in Figure 5.13a, the weight of the sample dropped dramatically from 100 °C to 260 °C following a gentle decrease until 300 °C and then a relative sharp decline between 300 °C to 400 °C. This is consistent with the MS (mass spectrometry) data shown in Figure 3.15b (the black line), the first H_2 peak was observed between 150 °C to 280 °C with a peak temperature at around 250 °C, and the second one appeared between 300 °C to 400 °C with a peak temperature at about 370 °C. In contrast, the 5 h milled samples displayed a similar desorption profile but with a shorter time for the release of the hydrogen. The 5 h milled samples stopped releasing at about 385 °C, but the one milled for 3 h released hydrogen even over 400 °C. This is consistent with the DSC measurements shown in Figure 5.14. As expected, the last endothermic peak of 3 h milled sample appeared 10 °C later than the one in 5 h milled $LiNH_2$+1.2LiH (O_2) and continued until 400 °C. However, the DSC data in Figure 5.14 showed that there are three endothermic peaks detected in both $LiNH_2$+1.2LiH (O_2) samples milled for 3 or 5 h. As marked in Figure 5.14, the samples milled for 3 and 5 hours have the same peak temperatures for the first two endothermic peaks. However, the peak combined by the first two peaks in 3 h milled sample is broader than in the 5 h milled composite, which corresponds to the results of (Varin, Jang et al. 2010) who reported that the broadening of the DSC peak in a $LiNH_2$+LiH composite reduced with increasing milling time.

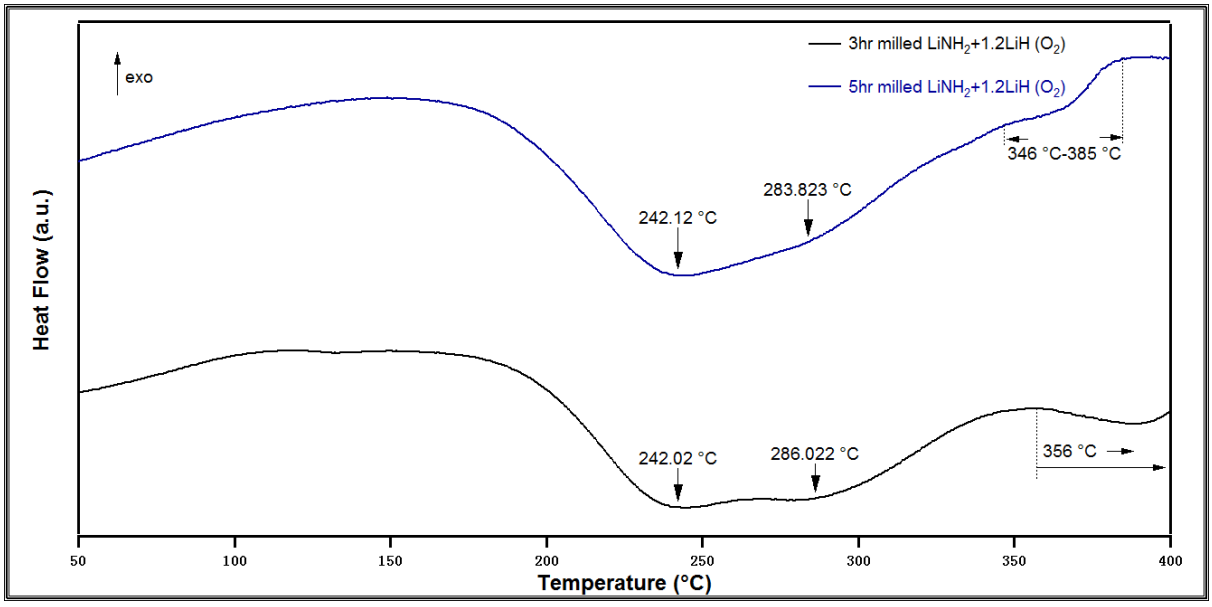

Figure 5.14 DSC profiles of 3 h milled $LiNH_2$+1.2LiH (O_2) (black line) and 5 h milled $LiNH_2$+1.2LiH (O_2) (blue line), heated at 2 °C/min with Ar flow (100 ml/min).

As discussed by (Ichikawa, Hanada et al. 2004, Hino, Ichikawa et al. 2005), there may be a two-step decomposition reaction. The first step is due to the decomposition of $LiNH_2$, Li_2NH and NH_3 are produced, and then the released NH_3 reacts with LiH very rapidly to form $LiNH_2$ and H_2. In the second step, the $LiNH_2$ produced in the first step decomposes to Li_2NH and NH_3, and the rapid reaction of emitted NH_3 and LiH occurs to produce Li_2NH and H_2. These two steps repeat successively until no active $LiNH_2$ and LiH phases remain.

In relation to the mass losses of the two 5 h milled $LiNH_2$+1.2LiH composites, 6.2 wt. % hydrogen was released from the composite containing less Li_2O, which is higher than the 5.3 wt. % obtained for the composite containing a larger amount of Li_2O ("5 h milled $LiNH_2$+1.2LiH (O_2)"). However, the sample with larger amount of Li_2O showed

a lower dehydrogenation onset temperature (80 °C) compared with the onset temperature of 100 °C (Figure 5.13a) for the sample without Li_2O (see Figure 5.12 purple line).

The presence of Li_2O in the 5 h milled sample reduced the amount of released hydrogen. This corresponds to the results of (Varin, Jang et al. 2010), who found that the existence of Li_2O in the $LiNH_2$+LiH system reduces the activation of LiH when it was reacted with NH_3 and weakened the decomposition process.

In-situ XRD was carried out on the composite of 5 h milled $LiNH_2$+1.2LiH, to investigate the reactions occurring during hydrogenation. XRD scans were collected at selected temperatures. The sample was heated from room temperature to 400 °C with a heating rate 2 ℃ /min under helium flow (100 ml/min). The XRD patterns detected at certain temperatures are displayed in Figure 5.15.

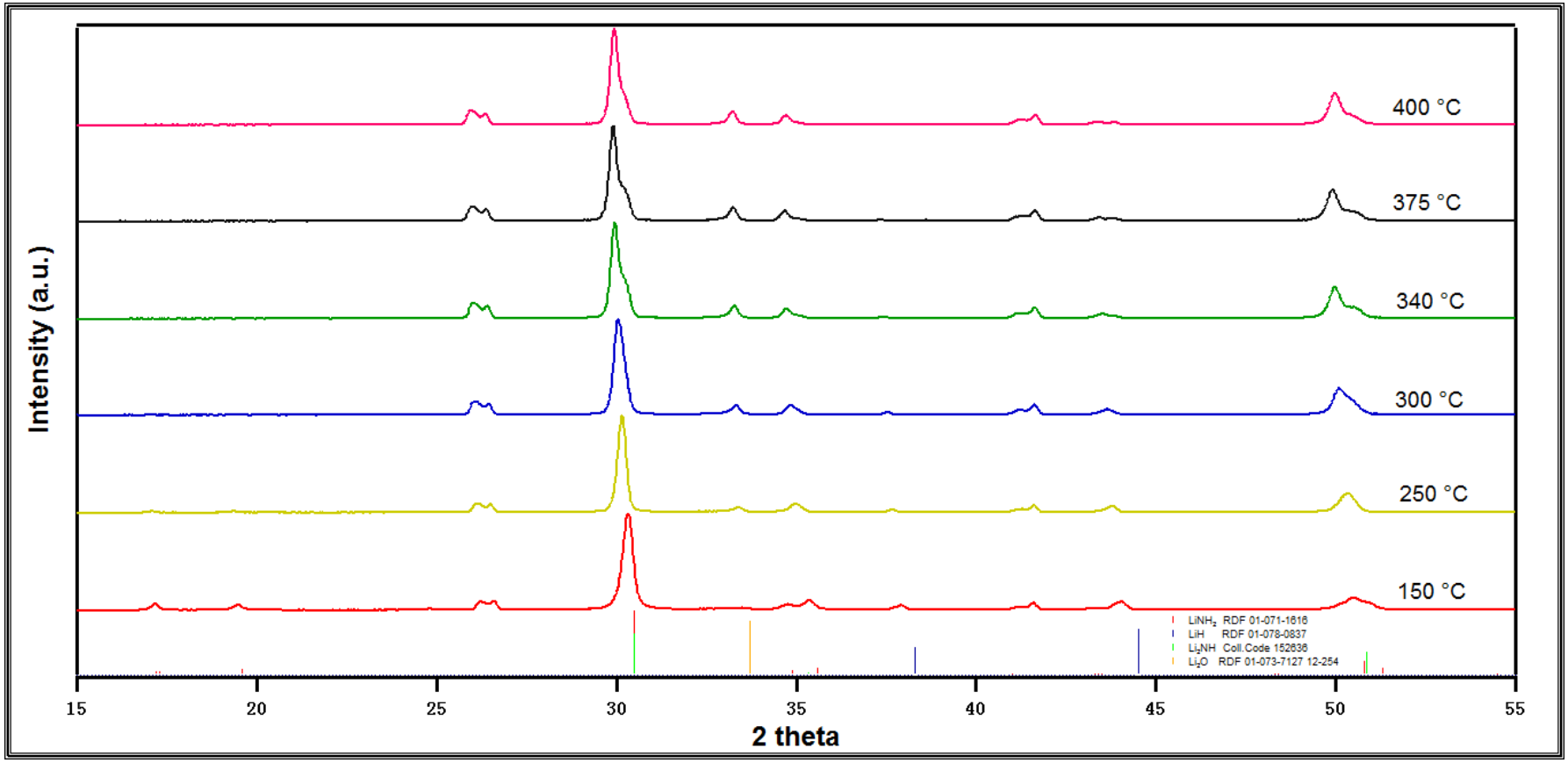

Figure 5.15 XRD patterns from in-situ XRD measurements of 5 h milled $LiNH_2$+1.2LiH composite at 150 °C, 250 °C, 300 °C, 340 °C, 375 °C and 400 °C. The heating is operated at 2 °C/min with helium flow (100 ml/min).

The main peaks introduced by $LiNH_2$ and LiH all shift to lower 2θ values with increasing temperature, which is due to the lattice thermal expansion. According to the XRD pattern observed at 340 °C, the peak located at around 30.2° develops into two peaks, and the same applies to the peak around 50.7°. This is known to be the formation of the Li_2NH phase (Varin, Jang et al. 2010, Varin and Jang 2011).

Actually, the new phase may appear earlier than 340 °C, based on the shape of the $LiNH_2$ peak located at about 50.7° already undergoing a slight change at 300 °C. It can be deduced that Li_2NH would be produced at the beginning of the reaction, but only single peaks are observed at 30.2° and 50.7°. It may be that the X-ray peaks for Li_2NH are quite close to those for $LiNH_2$ and that just small amounts of Li_2NH is formed before the temperature reaches 340 °C.

Two small peaks located at 26.1° and 26.5° are related to the sample holder which is used for the in-situ XRD measurement, because neither shape nor intensity of these peaks change.

5.3.3 Summary

As-received $LiNH_2$ decomposes into Li_2NH, NH_3 and a small amount of H_2 with a sharp decomposition peak of NH_3 starting at about 270 °C. The results indicate that the additional LiH may effectively react with the emitted NH_3 from $LiNH_2$ to form H_2. A two-step reaction between $LiNH_2$ and LiH was suggested to explain the mechanism

for the decomposition of the composite. Oxidation can be a significant barrier for the quantity of released hydrogen.

5.4 2Graphite + $LiNH_2$ +1.2LiH composites

$LiNH_2$+LiH composite and nano-structured graphite were both reported to be potential hydrogen storage materials (Orimo, Majer et al. 1999, Orimo, Züttel et al. 2003, Ichikawa, Hanada et al. 2004, Shaw, Ren et al. 2008), but they all have their own limitations. The major challenge of composite $LiNH_2$+LiH is oxidation (Yao, Shang et al. 2007), which "deactivates" the reaction between LiH and NH_3, reducing the tendency of the composite to decompose. The addition of graphite to $LiNH_2$+LiH was studied by (Varin and Jang 2011), and they found that graphite may prevent LiH from being oxidized by forming a coating on the surface of LiH. As graphite itself is also an effective hydrogen storage material, a graphite and $LiNH_2$+LiH composite may offer improved de/hydrogenation properties.

The $LiNH_2$+1.2LiH composite was investigated in two forms: oxidized LiH and non-oxidized LiH. $LiNH_2$+1.2LiH milled for 3 and 5 h which were studied in Section 5.4 are used to form the new composite with 8 h milled graphite.

For simplicity, these composites are named: 2 h milled LLG(O_2) (3+8), 2 h milled LLG(O_2) (5+8) and 2 h milled LLG (5+8). The first two samples used oxidized LiH, while the last one doesn't.

5.4.1 Characterization

5.4.1.1 Raman Spectra of $LiNH_2$+1.2LiH+2graphite composites

Figure 5.16 shows the room temperature Raman spectra of the three $LiNH_2$+1.2LiH+2graphite composites. Only Raman peaks for graphite appear in Figure 5.16. This could be because the $LiNH_2$ and LiH particles are covered by graphite during ball milling, which leads to a weak interaction with the laser.

As shown in Figure 5.16, the graphite Raman peaks for the G and G' bands, are observed at around 1582 cm^{-1} and 2663 cm^{-1}; D and D' bands at about 1326 cm^{-1} are induced by defects. Detailed data from these spectra are given in Table 5.2.

Table 5.2 Raman peak positions and calculated La values of the three $LiNH_2$+1.2LiH+2graphite composites.

	D band (cm^{-1})	D' band (cm^{-1})	G band (cm^{-1})	G' band (cm^{-1})	La value (nm)
2 h milled LLG (O_2) 3+8	1326.2	1618.7	1585.3	2663.3	3.0
2 h milled LLG (O_2) 5+8	1328.4	1616.2	1580.3	2662.4	3.8
2 h milled LLG 5+8	1326.2	1615.	1582.6	2661.8	3.1

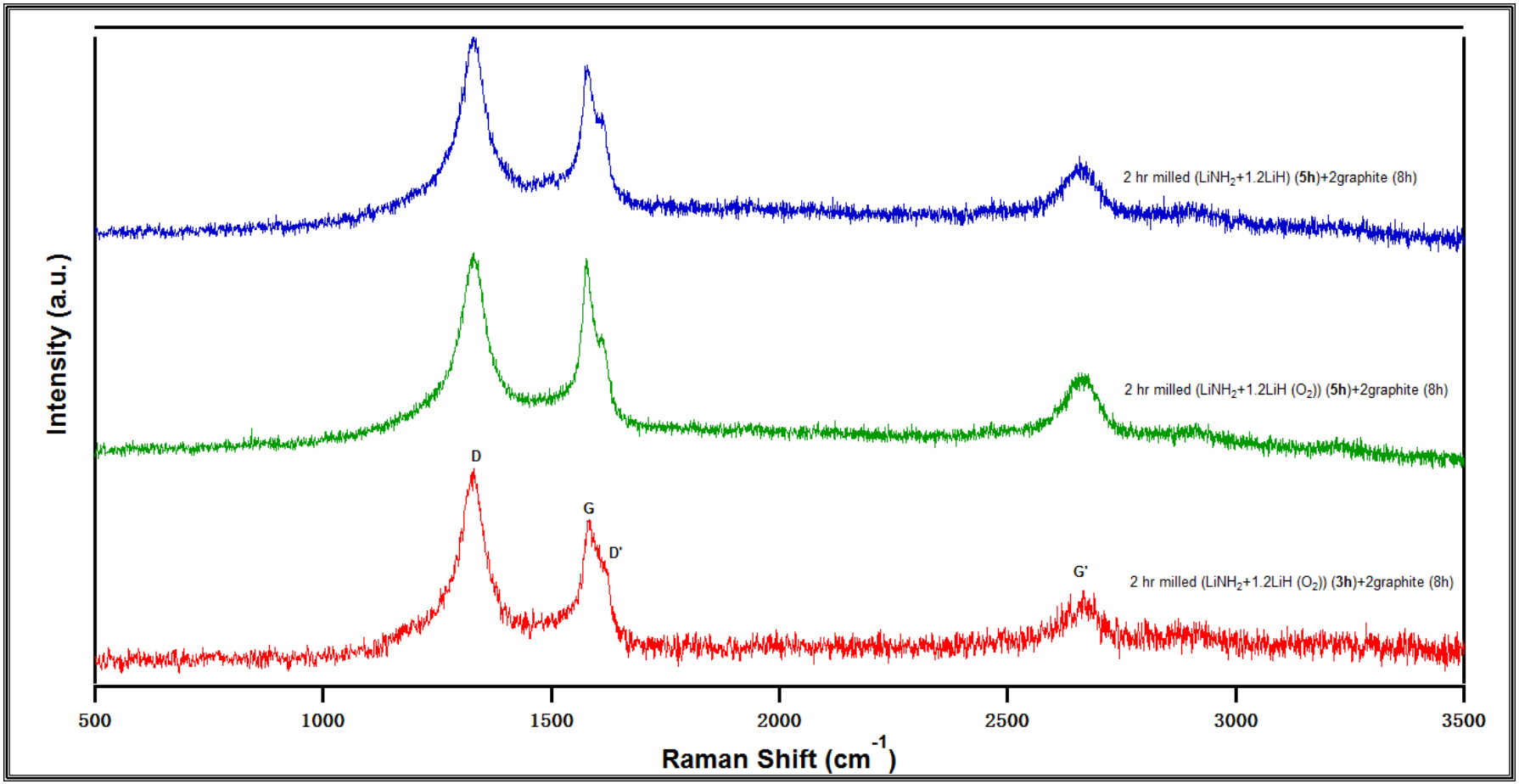

Figure 5.16 Room temperature Raman Spectrum of 2 h milled LLG (O_2) (3+8) (red line), 2 h milled LLG (O_2) (5+8) (green line) and 2 h milled LLG (5+8) (blue line).

There are not many differences in peak positions between the three samples. The La values (Section 5.1.1.1) for these samples are also listed in Table 5.2. For the samples which used LiH (O_2), LLG (O_2) 3+8 shows a lower La value than for the LLG (O_2) 5+8. This indicates that in-plane correlation length of LLG (O_2) 3+8 is smaller than that for LLG (O_2) 5+8. According to previous research on milled $LiNH_2$+LiH composites, the crystalline sizes of $LiNH_2$ and LiH in the composite reduce dramatically during the first 180 min and then tend to gently decline (Ichikawa, Hanada et al. 2004, Shaw, Ren et al. 2008, Varin, Jang et al. 2010). For graphite, it was reported that the particle size decreases just a small amount after milling for 2 h to 10 h (Zhang 2011, Zhang and Book 2011). However, agglomeration can also occur if the particle size is small enough, the larger particle size of 2 h milled LLG (O_2) 5+8 would be the agglomeration of the particles.

Actually, the total milling time for graphite in the three composites is 10 h, which includes 8 hours milling with hydrogen and 2 hours milling the $LiNH_2$+1.2LiH composite in hydrogen. This means its La value can be compared with 10 h milled graphite to see the effect of the addition of $LiNH_2$+1.2LiH. As shown in Table 5.1, the La value of 10 h milled graphite is 6.3 nm, much larger than the La values of these three samples. This demonstrates that there is a significant decrease in the in-plane crystalline size of the graphite, after the addition of $LiNH_2$+1.2LiH.

5.4.1.2 XRD measurements of $LiNH_2$+1.2LiH+2graphite composites

According to the room temperature XRD measurements shown in Figure 5.17, the X-ray peaks for the starting materials $LiNH_2$, LiH and graphite are all found in the three

XRD patterns. It can be seen that there is a small peak for Li_2O at 33.4° in 2 h milled LLG (O_2) 5+8 (red line in Figure 5.17). Topas analysis estimates that the weight percent of Li_2O in 2 h milled LLG (O_2) 5+8 is 2.5 wt. % and it is 0 in 2 h milled LLG 5+8. The amount of Li_2O in 2 h milled LLG (O_2) 3+8 is less than 2.5 wt. %.

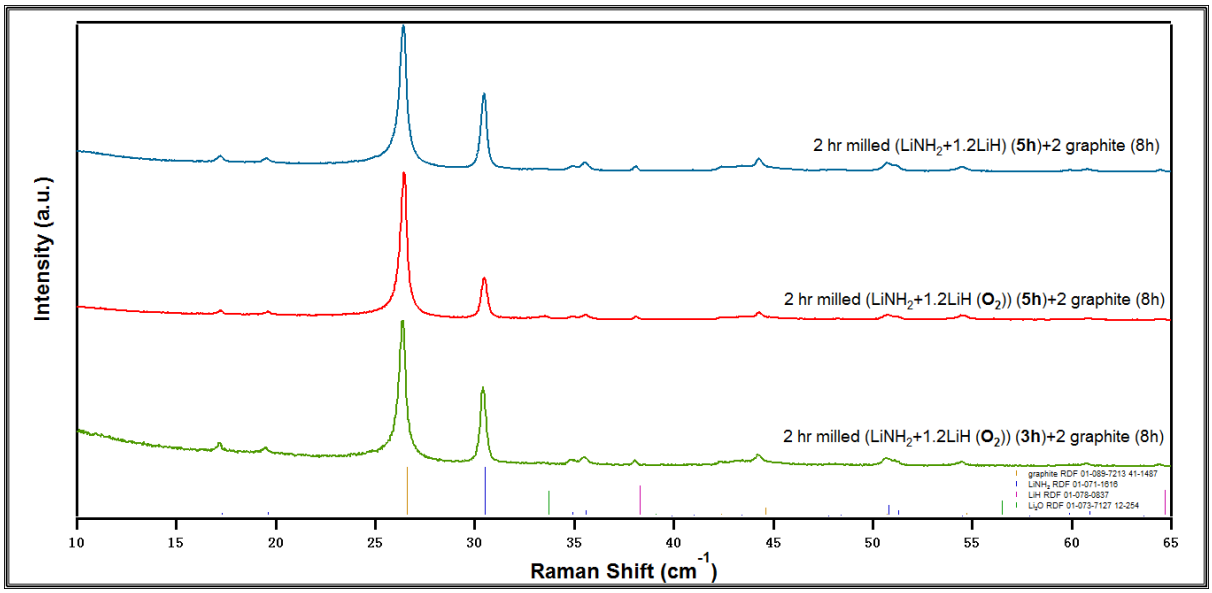

Figure 5.17 Room temperature XRD measurements of the as-prepared 2 h milled LLG (O_2) 3+8 (green line), 2 h milled LLG (O_2) 5+8 (red line) and 2 h milled LLG 5+8 (blue line).

5.4.2 Thermal decomposition

In this section, the thermal decomposition properties of the three samples will be presented, and then discussed in two parts: the effect of milling time and the influence of oxidation.

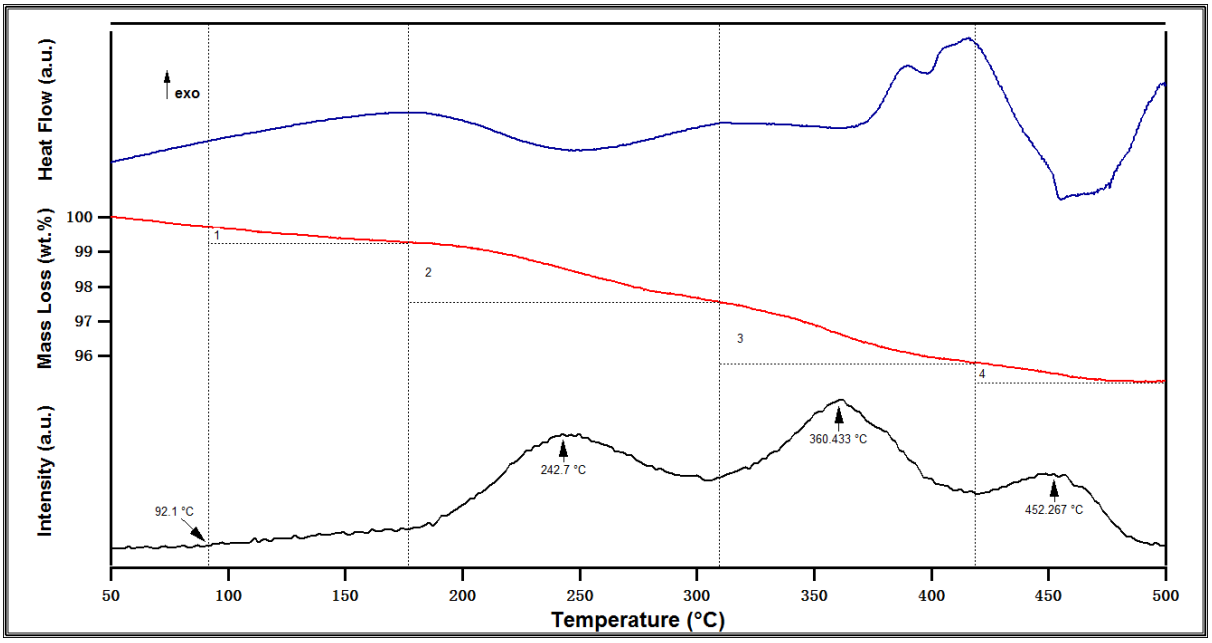

Figure 5.18 Scheme of TGA-MS and DSC measurements of 2 h milled LLG (O_2) 3+8; sample was heated from 30 °C to 500 °C at a heating rate of 2 °C/min with Ar flow (100 ml/min) in all the measurements.

Mass spectrometry shows (black line in Figure 5.18) that the onset temperature for releasing hydrogen is around 92 °C, following four hydrogen decomposition processes which are marked as 1, 2, 3 and 4 in Figure 5.18. At the first stage, only 0.5 wt. % hydrogen was detected by TGA (red line in Figure 5.18), and there is no distinct endothermic peak in DSC (blue line in Figure 5.18). The mass loss in the following three steps is 1.7 wt. %, 1.8 wt. % and 0.5 wt. %, respectively. The total mass loss of 2 h milled LLG (O_2) 3+8 is 4.5 wt. %. The second decomposition step occurs between 170 °C and 310 °C with a peak temperature at 242 °C, corresponding to a broad endothermic peak observed by DSC (Figure 5.18 blue line). This is consistent with the first hydrogen decomposition peak in the composite $LiNH_2$+1.2LiH, shown in Figures 5.13b and 5.14. Therefore, it seems that the hydrogen release during this step is from the reaction of $LiNH_2$ and LiH (Ichikawa, Hanada et al. 2004).

The third decomposition step observed between 310 °C and 420 °C shows a peak temperature at 360 °C. However, at this stage two endothermic DSC peaks are detected (Figure 5.18 blue line), which suggests that two reactions took place in the composite. The second endothermic peak in this stage is probably due to the melting of $LiNH_2$ as the temperature corresponds to the melting point of $LiNH_2$ (380 °C). However, the mechanism of the reaction at 360 °C is still unclear.

The fourth decomposition stage is observed after 420 °C with a peak temperature at 452 °C. Because it was found that no hydrogen was released after 400 °C in the previous research (Section 5.3) for $LiNH_2$+1.2LiH, so this stage could be induced by the reaction of graphite with the generated products from the previous steps.

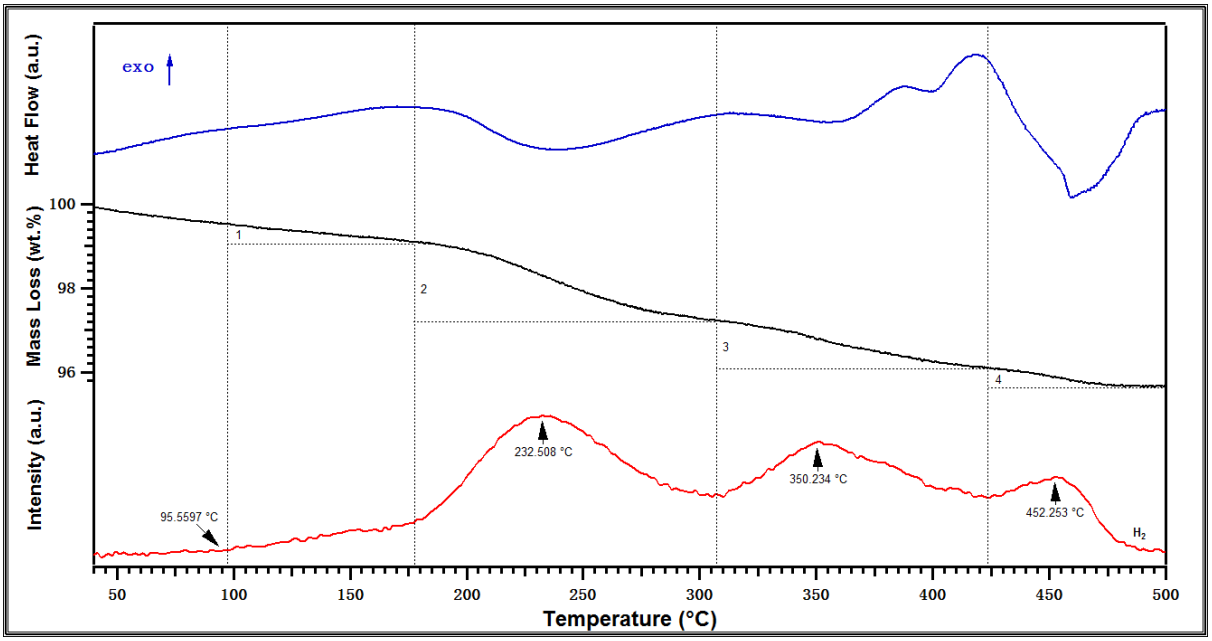

Figure 5.19 Scheme of TGA-MS and DSC measurements of 2 h milled LLG (O_2) 5+8. All the measurements were carried out from 30 °C to 500 °C with a heating rate of 2 °C/min under Ar flow (100 ml/min).

2 h milled LLG (O_2) 5+8 shows a similar thermal decomposition process to 2 h milled LLG (O_2) 3+8: four decomposition processes are observed by TGA-MS, as shown in Figure 5.19. These four stages started with an onset temperature of 95.5 °C. The peak temperatures of the following two steps are both 10 °C lower than the ones in 2 h milled LLG (O_2) 3+8. This might be influenced by a longer milling time, which would increase particle time. However, the total amount of desorbed hydrogen is 3.9 wt. %, which is lower than for 2 h milled LLG (O_2) 3+8. 1.9 wt. % and 1.1 wt. % hydrogen was released in the 2nd and 3rd stage, respectively. Less hydrogen was released in the 3rd stage, compared with the LLG (O_2) 3+8 sample. Therefore, the two reactions during the 3rd stage appear to be affected by milling time.

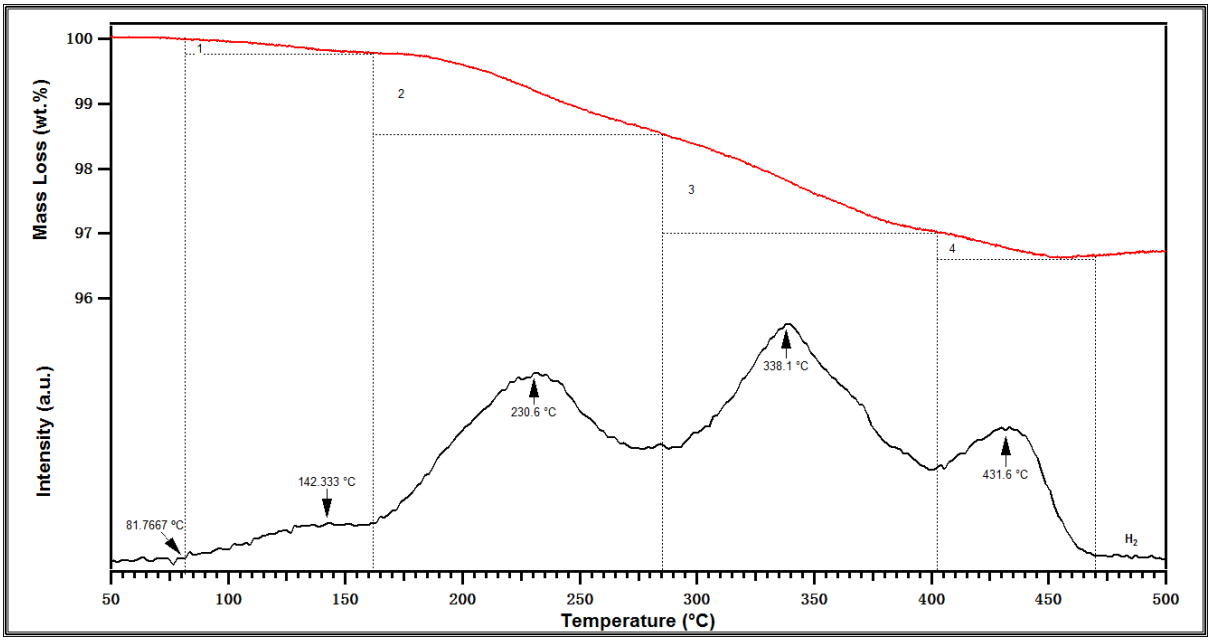

Figure 5.20 TGA-MS measurements of 2 h milled LLG 5+8. The sample was heated from 30 °C to 500 °C with a heating rate of 2 °C/min under Ar flow (100 ml/min).

Figure 5.20 shows the TGA-MS data for the 2 h milled LLG 5+8 composite, which consists of four hydrogen decomposition processes. A 14 °C lower onset

temperature is observed in the TGA data, shown in Figure 5.20. There is the same peak temperature in the 2nd stage for 2 h milled LLG (O_2) 5+8, but a 12 °C lower peak in the 3rd stage. As discussed before, the reaction in stage 2 is probably the reaction of $LiNH_2$ and LiH. One of the reactions is probably the melting of $LiNH_2$, and the other is unknown. Therefore, it seems that oxidation retards a number of the reactions, especially during the third stage, which leads to a higher reaction temperature and dehydrogenation onset temperature. However, only 3.4 wt. % H_2 was obtained after heating, which is less than the 3.9 wt. % for the oxidized sample.

Figure 5.21 shows the in-situ XRD measurements of the 2 h milled LLG 5+8 composite. At around 350 °C, the intensity of the main X-ray peaks of $LiNH_2$ and LiH disappeared; meanwhile, some other new peaks appeared which are identified as Li_2NCN. According to this, the whole heating process can be discussed in two parts.

The first part is between 25 °C and 350 °C. The intensity of the main X-ray peaks of LiH disappear at around 300 °C, followed by $LiNH_2$, whose intensity disappears at around 350 °C. This shows that the $LiNH_2$ and LiH in the composite are already reacted completely. The intensity of the X-ray peaks of graphite do not change much, which indicates that the amount of graphite in the heated composite is not decreased when the temperature is lower than 350 °C. Considering the TGA results shown in Figure 5.20, graphite probably does not undergo any reaction below 350 °C. During this range, only the reaction of $LiNH_2$ and LiH takes place. In Figure 5.20, the 3rd stage of hydrogen release contains two stages: the first is below 350 °C and is the reaction of $LiNH_2$ and LiH or the melting of $LiNH_2$ (because LiH disappeared earlier

than $LiNH_2$, so some more accurate measurements are still needed to confirm the reaction); and the second is above 350 °C and is the reaction of graphite with Li-N material, because no $LiNH_2$ and LiH remains.

In the second part, the temperature between 350 °C and 500 °C, it is clear to see that the intensity of the Li_2NCN X-ray peaks increased, and the position of the graphite X-ray peaks shifted to a lower angle. The formation of Li_2NCN shows that carbon takes part in the dehydrogenation reaction with Li-N material. If the reaction $LiNH_2+LiH=Li_2NH+H_2\uparrow$ occurs, then Li_2NCN would come from the reaction of carbon and Li_2NH. However, the origin of the –CN bonding is quite complicated. Also, the evidence for the presence of Li_2NH is difficult to find in the in-situ XRD patterns, as its main X-ray peaks are overlap with the X-ray peaks for $LiNH_2$. Therefore, more evidence to understand these reactions is still needed.

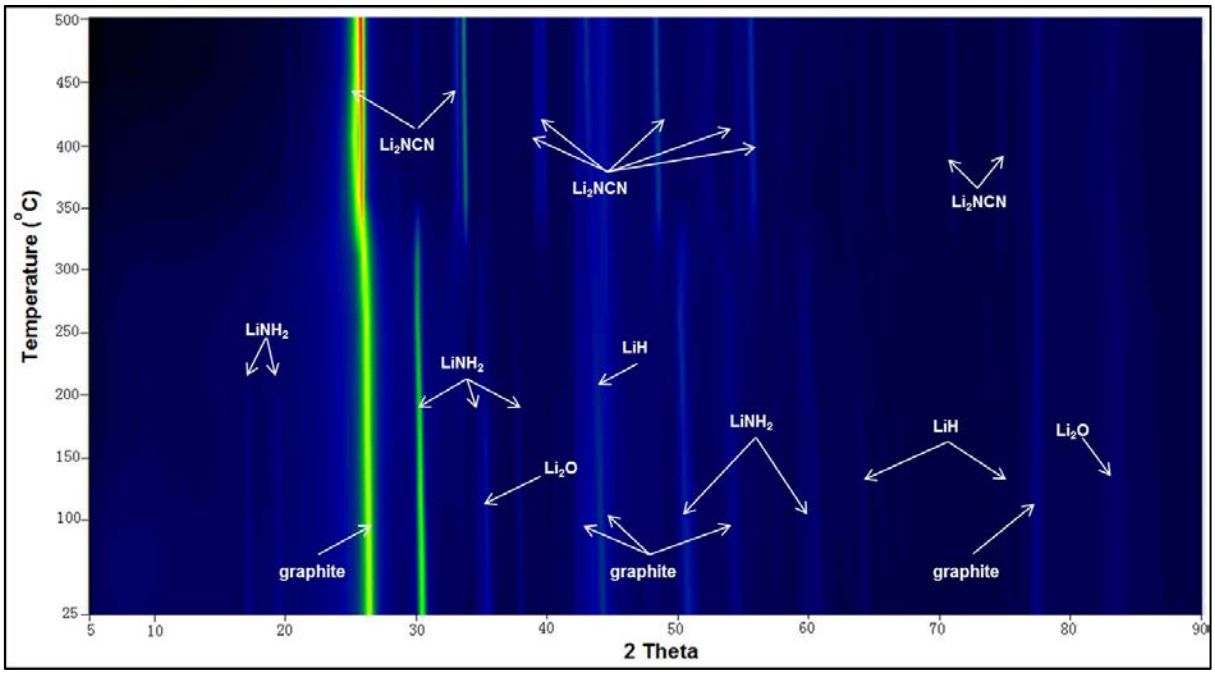

Figure 5.21 In-situ XRD measurements of 2 h milled LLG 5+8. The sample was heated at 2 °C/min under helium (100 ml/min); the colour is relative to the peak intensity, black means the minimum and red is the maximum.

5.4.3 Summary

According to the results presented in this section, the detailed dehydrogenation reactions for the 2graphite+$LiNH_2$+1.2LiH composite are still not clearly understood. Therefore, further studies are needed.

However, it can be said that the four stages of hydrogen release can be divided into two stages: the reactions of $LiNH_2$ and LiH first, followed by the decomposition of hydrogenated graphite and the reaction of carbon and the Li-N material. Oxidation may influence the dehydrogenation processes, but the exact reaction(s) are unclear.

The reactions occurring during dehydrogenation are quite complicated, with the formation of Li_2NCN which is known to be toxic (Down, Haley et al. 1978). It is difficult to control the complicated reactions during dehydrogenation of these composite samples, and there may be safety issues associated with dealing with Li_2NCN.

6 Conclusions

This work shows that the ternary composite of graphite+$LiNH_2$+LiH can contribute max 4.5 wt. % of released hydrogen, which is lower than the 6.2 wt. % for $LiNH_2$+LiH. The new phase Li_2NCN formed during the decomposition of graphite+$LiNH_2$+LiH is known from the literature to be toxic, and so which may result in safety issues were it to be used as a hydrogen storage medium.

Graphite was ball-milled under 3 bar H_2 for 8 h (two samples, milled at 180 rpm and 280 rpm, separately) and 10 h. Room temperature XRD and Raman scattering showed that the longer milling time and higher milling rotation speed created defects and amorphous phases in the graphite. Thermal decomposition measurements suggest the presence of C-H dangling bonds, as the onset temperature for hydrogen release is over 350 °C, which is much higher than the decomposition temperature for hydrogen adsorbed via physisorption. This supports the results of Zhang and Book et al (2011) (Zhang and Book 2011). Graphite milled for 10 h (3 bar H_2, 280 rpm) released 2.15 wt. % H_2 when the sample was heated from 30 °C to 950 °C at 2 °C/min, no other gases were detected.

8 h ball-milled graphite under 3 bar H_2 was added to $LiNH_2$ in a molar ratio of 2:1 (graphite:$LiNH_2$) and then milled for a further 2 h. TGA-MS showed that 4.6 wt. % of hydrogen was released, with 8.0 wt. % of NH_3, when the composite was heated to 400 °C. LiH, graphite, Li_2O and LiOH were detected by XRD after this measurement. However, the gases released during the decomposition of as-received $LiNH_2$ are

almost only NH_3. Therefore, this suggests that the release of hydrogen contained within the hydrogenated ball-milled graphite reduces the quantity of released NH_3. However, further in situ measurements are needed in order to elucidate the reaction pathway(s), leading to the formation of LiH and the emission of NH_3 and H_2.

$LiNH_2$+1.2LiH was ball-milled under 1 bar Ar for either 3 h or 5 h. Broadening of the X-ray peaks with increased milling, suggests a significant decrease in the grain size of the $LiNH_2$. Three stages of decomposition during heating were shown by DSC: melting of $LiNH_2$; decomposition of $LiNH_2$; and the reaction between NH_3 and LiH. This is consistent with studies by (Ichikawa, Hanada et al. 2004). In-situ XRD measurements were performed to understand the decomposition pathway(s). Li_2NH was found at 340 °C, which is the onset temperature of the third endothermic DSC peak. However, NH_3 was not detected by TGA-MS, and H_2 release dramatically increased above 150 °C. For the $LiNH_2$+1.2LiH (less oxidation) composite milled for 5 h, 6.2 wt. % of H_2 released when it was heated from 30 °C to 400 °C, with no NH_3 detected.

8 h ball-milled graphite was then mixed with $LiNH_2$+1.2LiH at a molar ratio of 2:1 (graphite:powder), and milled for a further 2 h under 3 bar H_2. TGA-MS showed a hydrogen release of 3.4 wt. % to 4.5 wt. % during heating to 500 °C. In-situ XRD showed the formation of Li_2NCN, and the disappearance of $LiNH_2$ and LiH, when the composite was heated to 350 °C. The expected decomposition products (Ichikawa, Hanada et al. 2004, Miyaoka, Ichikawa et al. 2009) of the binary composites studied previously, are LiH, Li_2C_2 and Li_2NH. However, this work shows that graphite, $LiNH_2$

and LiH in the form of a ternary composite, exhibits different decomposition behaviour. The DSC measurements of $LiNH_2$+1.2LiH and 2graphite+$LiNH_2$+1.2LiH showed the same endothermic peak at around 240 °C, which indicates that this should be a reaction involving $LiNH_2$ and LiH. For 2graphite+$LiNH_2$+1.2LiH, two hydrogen TGA-MS peaks correspond with three endothermic DSC peaks, suggesting that Li_2NCN forms in different stages. However, it is not clear in detail, what reactions occur between 350 °C and 500 °C.

In terms of the effect of oxidation, it was found that composites containing oxidized LiH (LLG (O_2) 5+8) released a larger quantity of H_2 in, but at a 10 °C higher onset temperature (compared to LLG 5+8). Therefore, it is not clear whether the effects of oxygen contamination in the LiH component are beneficial to the hydrogen storage properties of the composite or not.

7 Future Work

It is still necessary to understand the mechanism of the reactions between hydrogenated graphite and $LiNH_2$. This may be identified if isotopic exchange (D for H) was carried out for the hydrogen absorbed into the milled graphite.

To determine the viability of the graphite+$LiNH_2$+LiH composite as a potential hydrogen storage material, its reversibility will also need to be investigated. IGA or Sieverts-PCT measurements could be carried out to test the dehydrogenation and rehydrogenation performance of the composite.

Finally, it is quite necessary to understand the mechanism of the formation of Li_2NCN during decomposition. Further in situ XRD, Raman and FT-IT measurements could be useful in trying to elucidate the reaction pathways.

8 References

Ahluwalia, R. K., T. Q. Hua, J. K. Peng, S. Lasher, K. McKenney, J. Sinha and M. Gardiner (2010). "Technical assessment of cryo-compressed hydrogen storage tank systems for automotive applications." International Journal of Hydrogen Energy **35**(9): 4171-4184.

Ahluwalia, R. K., Hua, T.Q., Peng, J-K., Roh, H.S. (2013). "System Level Analysis of Hydrogen Storage Options" Proceedings of the 2013 US DOE Hydrogen and Fuel Cells Program Annual Merit Review. Crystal City. Arlington, VA.

Aladekomo, J. B. and R. H. Bragg (1990). "Structural transformations induced in graphite by grinding: Analysis of 002 X-ray diffraction line profiles." Carbon **28**(6): 897-906.

Anderson, P. A., P. A. Chater, D. R. Hewett and P. R. Slater (2011). "Hydrogen storage and ionic mobility in amide-halide systems." Faraday Discussions **151**(0): 271-284.

Barghi, S. H., T. T. Tsotsis and M. Sahimi (2014). "Chemisorption, physisorption and hysteresis during hydrogen storage in carbon nanotubes." International Journal of Hydrogen Energy **39**(3): 1390-1397.

Beister, H. J., S. Haag, R. Kniep, K. Strössner and K. Syassen (1988). "Phase Transformations of Lithium Nitride under Pressure." Angewandte Chemie International Edition in English **27**(8): 1101-1103.

Bohger, J. P. O., R. R. Eßmann and H. Jacobs (1995). "Infrared and Raman studies on the internal modes of lithium amide." Journal of Molecular Structure **348**(0): 325-328.

Boukamp, B. A. and R. A. Huggins (1976). "Lithium ion conductivity in lithium nitride." Physics Letters A **58**(4): 231-233.

Chambers, A., C. Park, R. T. K. Baker and N. M. Rodriguez (1998). "Hydrogen Storage in Graphite Nanofibers." The Journal of Physical Chemistry B **102**(22): 4253-4256.

Chen, D. M., T. Ichikawa, H. Fujii, N. Ogita, M. Udagawa, Y. Kitano and E. Tanabe (2003). "Unusual hydrogen absorption properties in graphite mechanically milled under various hydrogen pressures up to 6 MPa." Journal of Alloys and Compounds **354**(1–2): L5-L9.

Chen, P., X. Wu, J. Lin and K. L. Tan (1999). "High H2 Uptake by Alkali-Doped Carbon Nanotubes Under Ambient Pressure and Moderate Temperatures." Science **285**(5424): 91-93.

Chen, Y., J. Fitz Gerald, L. T. Chadderton and L. Chaffron (1999). "Nanoporous carbon produced by ball milling." Applied Physics Letters **74**(19): 2782-2784.

Chen, Y., D. T. Shaw, X. D. Bai, E. G. Wang, C. Lund, W. M. Lu and D. D. L. Chung (2001). "Hydrogen storage in aligned carbon nanotubes." Applied Physics Letters **78**(15): 2128-2130.

Darkrim, F. L., P. Malbrunot and G. P. Tartaglia (2002). "Review of hydrogen storage by adsorption in carbon nanotubes." International Journal of Hydrogen Energy **27**(2): 193-202.

de la Casa-Lillo, M. A., F. Lamari-Darkrim, D. Cazorla-Amorós and A. Linares-Solano (2002). "Hydrogen Storage in Activated Carbons and Activated Carbon Fibers." The Journal of Physical Chemistry B **106**(42): 10930-10934.

Dillon, A. C. and M. J. Heben (2001). "Hydrogen storage using carbon adsorbents: past, present and future." Applied Physics A Materials Science & Processing **72**(2): 133-142.

Down, M. G., M. J. Haley, P. Hubberstey, R. J. Pulham and A. E. Thunder (1978). "Synthesis of the dilithium salt of cyanamide in liquid lithium; X-ray crystal structure of Li2NCN." Journal of the Chemical Society, Chemical Communications(2): 52.

Durbin, D. J. and C. Malardier-Jugroot (2013). "Review of hydrogen storage techniques for on board vehicle applications." International Journal of Hydrogen Energy(0).

Edwards, P. P., V. L. Kuznetsov and W. I. David (2007). "Hydrogen energy." Philos Trans A Math Phys Eng Sci **365**(1853): 1043-1056.

Felderhoff, M., C. Weidenthaler, R. von Helmolt and U. Eberle (2007). "Hydrogen storage: the remaining scientific and technological challenges." Phys Chem Chem Phys **9**(21): 2643-2653.

Ferrari, A. C. and J. Robertson (2000). "Interpretation of Raman spectra of disordered and amorphous carbon." Physical Review B **61**(20): 14095-14107.

Fukunaga, T., K. Nagano, U. Mizutani, H. Wakayama and Y. Fukushima (1998). "Structural change of graphite subjected to mechanical milling." Journal of Non-Crystalline Solids **232–234**(0): 416-420.

Goodman, D. W., R. D. Kelley, T. E. Madey and J. T. Yates Jr (1980). "Kinetics of the hydrogenation of CO over a single crystal nickel catalyst." Journal of Catalysis **63**(1): 226-234.

Graetz, J. (2009). "New approaches to hydrogen storage." Chem Soc Rev **38**(1): 73-82.

Gregory, D. H. (2008). "Lithium nitrides, imides and amides as lightweight, reversible hydrogen stores." Journal of Materials Chemistry **18**(20): 2321.

Grochala, W. and P. P. Edwards (2004). "Thermal Decomposition of the Non-Interstitial Hydrides for the Storage and Production of Hydrogen." Chemical Reviews **104**(3): 1283-1316.

H. Marsh, F. R.-R. (2005). Activated Carbon, Elsevier.

Henderson, C. C., C. McMichael Rohlfing and P. A. Cahill (1993). "Theoretical studies of selected C60H2 and C70H2 isomers." Chemical Physics Letters **213**(3–4): 383-388.

Hino, S., T. Ichikawa, N. Ogita, M. Udagawa and H. Fujii (2005). "Quantitative estimation of NH3 partial pressure in H2 desorbed from the Li-N-H system by Raman spectroscopy." Chem Commun (Camb)(24): 3038-3040.

Hirscher, M. and M. Becher (2003). "Hydrogen Storage in Carbon Nanotubes." Journal of Nanoscience and Nanotechnology **3**(1-2): 3-17.

Huang, Z., A. Calka and H. Liu (2007). "Effects of milling conditions on hydrogen storage properties of graphite." Journal of Materials Science **42**(14): 5437-5441.

Huq, A., J. W. Richardson, E. R. Maxey, D. Chandra and W.-M. Chien (2007). "Structural studies of Li3N using neutron powder diffraction." Journal of Alloys and Compounds **436**(1–2): 256-260.

Ichikawa, T., D. M. Chen, S. Isobe, E. Gomibuchi and H. Fujii (2004). "Hydrogen storage properties on mechanically milled graphite." Materials Science and Engineering: B **108**(1-2): 138-142.

Ichikawa, T., H. Fujii, S. Isobe and K. Nabeta (2005). "Rechargeable hydrogen storage in nanostructured mixtures of hydrogenated carbon and lithium hydride." Applied Physics Letters **86**(24): 241914.

Ichikawa, T., N. Hanada, S. Isobe, H. Leng and H. Fujii (2004). "Mechanism of Novel Reaction from LiNH2 and LiH to Li2NH and H2 as a Promising Hydrogen Storage System." The Journal of Physical Chemistry B **108**(23): 7887-7892.

Ichikawa, T., S. Isobe, N. Hanada and H. Fujii (2004). "Lithium nitride for reversible hydrogen storage." Journal of Alloys and Compounds **365**(1-2): 271-276.

Ichikawa, T., H. Miyaoka and Y. Kojima (2011). Hydrogen Storage Properties of Hydrogenated Graphite and Lithium Hydride Nanocomposite. Advances in Diverse Industrial Applications of Nanocomposites. D. B. Reddy, InTech.

Iijima., S. (1991). "Helical microtubules of graphitic carbon." Nature **354**: 56-58.

Imamura, H., K. Masanari, M. Kusuhara, H. Katsumoto, T. Sumi and Y. Sakata (2005). "High hydrogen storage capacity of nanosized magnesium synthesized by high energy ball-milling." Journal of Alloys and Compounds **386**(1–2): 211-216.

Itoh, K., Y. Miyahara, S.-i. Orimo, H. Fujii, T. Kamiyama and T. Fukunaga (2003). "The local structure of hydrogen storage nanocrystalline graphite by neutron scattering." Journal of Alloys and Compounds **356–357**(0): 608-611.

Kano, J. and F. Saito (1998). "Correlation of powder characteristics of talc during Planetary Ball Milling with the impact energy of the balls simulated by the Particle Element Method." Powder Technology **98**(2): 166-170.

Leng, H. Y., T. Ichikawa, S. Isobe, S. Hino, N. Hanada and H. Fujii (2005). "Desorption behaviours from metal–N–H systems synthesized by ball milling." Journal of Alloys and Compounds **404-406**: 443-447.

M. S. DRESSELHAUS, G. D., and R. SAITO (1995). "Physics of carbon nanotubes." Carbon **33**(7): 883-891.

Miyaoka, H., T. Ichikawa and H. Fujii (2007). "Thermodynamic and structural properties of ball-milled mixtures composed of nano-structural graphite and alkali(-earth) metal hydride." Journal of Alloys and Compounds **432**(1–2): 303-307.

Miyaoka, H., T. Ichikawa and Y. Kojima (2009). "The reaction process of hydrogen absorption and desorption on the nanocomposite of hydrogenated graphite and lithium hydride." Nanotechnology **20**(20): 204021.

N. J.Welham, a. J. S. W. (1998). "EXTENDED MILLING OF GRAPHITE AND ACTIVATED CARBON." **36**: 1309–1315.

Nakamura, J., H. Hirano, M. Xie, I. Matsuo, T. Yamada and K.-i. Tanaka (1989). "Formation of a hybrid surface of carbide and graphite layers on Ni(100) but no hybrid surface on Ni(111)." Surface Science Letters **222**(1): L809-L817.

Nellis, W. J. (2006). "Dynamic compression of materials: metallization of fluid hydrogen at high pressures." Reports on Progress in Physics **69**(5): 1479-1580.

Nelly M. Rodriguez, A. C., and R. Terry K. Baker (1995). "Catalytic Engineering of Carbon Nanostructures." Langmuir **11**(10): 3863-3866.

Ngene, P., M. van Zwienen and P. E. de Jongh (2010). "Reversibility of the hydrogen desorption from LiBH4: a synergetic effect of nanoconfinement and Ni addition." Chemical Communications **46**(43): 8201-8203.

Niemann, M. U., S. S. Srinivasan, A. R. Phani, A. Kumar, D. Y. Goswami and E. K. Stefanakos (2008). "Nanomaterials for Hydrogen Storage Applications: A Review." Journal of Nanomaterials **2008**: 1-9.

O'Malley, K., G. Ordaz, J. Adams, K. Randolph, C. C. Ahn and N. T. Stetson (2014). "Applied hydrogen storage research and development: A perspective from the U.S. Department of Energy." Journal of Alloys and Compounds(0).

Ordaz, S. M. a. G. (2013). Onboard Type IV Compressed Hydrogen Storage Systems -Current Performance and Cost. DOE.

Orimo, S.-i., Y. Nakamori, J. R. Eliseo, A. Züttel and C. M. Jensen (2007). "Complex Hydrides for Hydrogen Storage." Chemical Reviews **107**(10): 4111-4132.

Orimo, S., G. Majer, T. Fukunaga, A. Zuttel, L. Schlapbach and H. Fujii (1999). "Hydrogen in the mechanically prepared nanostructured graphite." Applied Physics Letters **75**(20): 3093-3095.

Orimo, S., A. Züttel, L. Schlapbach, G. Majer, T. Fukunaga and H. Fujii (2003). "Hydrogen interaction with carbon nanostructures: current situation and future prospects." Journal of Alloys and Compounds **356–357**(0): 716-719.

Palumbo, O., A. Paolone, R. Cantelli and D. Chandra (2008). "Lithium nitride as hydrogen storage material." International Journal of Hydrogen Energy **33**(12): 3107-3110.

Park, C., P. E. Anderson, A. Chambers, C. D. Tan, R. Hidalgo and N. M. Rodriguez (1999). "Further Studies of the Interaction of Hydrogen with Graphite Nanofibers." The Journal of Physical Chemistry B **103**(48): 10572-10581.

Patchkovskii, S., J. S. Tse, S. N. Yurchenko, L. Zhechkov, T. Heine and G. Seifert (2005). "Graphene nanostructures as tunable storage media for molecular hydrogen." Proceedings of the National Academy of Sciences of the United States of America **102**(30): 10439-10444.

Patchkovskii, S., J. S. Tse, S. N. Yurchenko, L. Zhechkov, T. Heine and G. Seifert (2005). "Graphene nanostructures as tunable storage media for molecular hydrogen." Proc Natl Acad Sci U S A **102**(30): 10439-10444.

Ping. Chen, Z. X., Jizhong. Luo, Jianyi. Lin & Kuang Lee Tan (2002). "Interaction of hydrogen with metal nitrides and imides." Nature **420**(6913): 302-304.

Pinkerton, F. E. (2005). "Decomposition kinetics of lithium amide for hydrogen storage materials." Journal of Alloys and Compounds **400**(1-2): 76-82.

Pinkerton, F. E. (2005). "Decomposition kinetics of lithium amide for hydrogen storage materials." Journal of Alloys and Compounds **400**(1–2): 76-82.

Poirier, E., R. Chahine and T. K. Bose (2001). "Hydrogen adsorption in carbon nanostructures." International Journal of Hydrogen Energy **26**(8): 831-835.

Pukazhselvan, D., B. K. Gupta, A. Srivastava and O. N. Srivastava (2005). "Investigations on hydrogen storage behavior of CNT doped NaAlH4." Journal of Alloys and Compounds **403**(1–2): 312-317.

Reich, S. and C. Thomsen (2004). "Raman spectroscopy of graphite." Philos Trans A Math Phys Eng Sci **362**(1824): 2271-2288.

Roy, M. (2012). 17 - Nanocrystalline and Disordered Carbon Materials. Functional Materials. S. Banerjee and A. K. Tyagi. London, Elsevier**:** 675-706.

Ruckenstein, Y. H. H. a. E. (2006). "Hydrogen Storage of Li_2NH Prepared by Reacting Li with NH_3." Ind. Eng. Chem. Res. **45**: 182-186.

Sakintuna, B., F. Lamari-Darkrim and M. Hirscher (2007). "Metal hydride materials for solid hydrogen storage: A review." International Journal of Hydrogen Energy **32**(9): 1121-1140.

Shashikala, K. (2012). "Hydrogen Storage Materials." 607-637.

Shaw, L. L., R. Ren, T. Markmaitree and W. Osborn (2008). "Effects of mechanical activation on dehydrogenation of the lithium amide and lithium hydride system." Journal of Alloys and Compounds **448**(1-2): 263-271.

Shen, T. D., W. Q. Ge, K. Y. Wang, M. X. Quan, J. T. Wang, W. D. Wei and C. C. Koch (1996). "Structural disorder and phase transformation in graphite produced by ball milling." Nanostructured Materials **7**(4): 393-399.

Steinfeld, A. (2002). "Solar hydrogen production via a two-step water-splitting thermochemical cycle based on Zn/ZnO redox reactions." International Journal of Hydrogen Energy **27**(6): 611-619.

Ströbel, R., J. Garche, P. T. Moseley, L. Jörissen and G. Wolf (2006). "Hydrogen storage by carbon materials." Journal of Power Sources **159**(2): 781-801.

Takayuki Ichikawa, † Nobuko Hanada,‡ Shigehito Isobe,‡ Haiyan Leng,‡ and Hironobu Fujii† (2004). "Mechanism of Novel Reaction from LiNH2 and LiH to Li2NH and H2 as a Promising Hydrogen Storage System." J. Phys. Chem. B **108**: 7887-7892.

Takayuki Ichikawa, N. H., Shigehito Isobe, Haiyan Leng and Hironobu Fujii (2005). "Composite Materials based on Light Elements for Hydrogen Storage." Materials Transactions **46**: 1-14.

Tan, C., K. Tan, Y. Ong, A. Mohamed, S. Zein and S. Tan (2012). Carbon Nanotubes Applications: Solar and Fuel Cells, Hydrogen Storage, Lithium Batteries, Supercapacitors, Nanocomposites, Gas, Pathogens, Dyes, Heavy Metals and Pesticides. Environmental Chemistry for a Sustainable World. E. Lichtfouse, J. Schwarzbauer and D. Robert, Springer Netherlands**:** 3-46.

Tibbetts, G. G., G. P. Meisner and C. H. Olk (2001). "Hydrogen storage capacity of carbon nanotubes, filaments, and vapor-grown fibers." Carbon **39**(15): 2291-2301.

Tidjani, M., J. Lachter, T. S. Kabre and R. H. Bragg (1986). "Structural disorder induced in graphite by grinding." Carbon **24**(4): 447-449.

Tuinstra, F. (1970). "Raman Spectrum of Graphite." The Journal of Chemical Physics **53**(3): 1126.

Varin, R. A. and M. Jang (2011). "The effects of graphite on the reversible hydrogen storage of nanostructured lithium amide and lithium hydride (LiNH2+1.2LiH) system." Journal of Alloys and Compounds **509**(25): 7143-7151.

Varin, R. A., M. Jang and M. Polanski (2010). "The effects of ball milling and molar ratio of LiH on the hydrogen storage properties of nanocrystalline lithium amide and lithium hydride (LiNH2+LiH) system." Journal of Alloys and Compounds **491**(1-2): 658-667.

Welham, N. and J. Williams (1998). "Extended milling of graphite and activated carbon." Carbon **36**(9): 1309-1315.

Welham, N. J., V. Berbenni and P. G. Chapman (2003). "Effect of extended ball milling on graphite." Journal of Alloys and Compounds **349**(1–2): 255-263.

Y. Ye, C. C. A., C. Witham, B. Fultz, J. Liu, A. G. Rinzler, D. Colbert, K. A. Smith, and R. E. Smalley (1999). "Hydrogen adsorption and cohesive energy of single-walled carbon nanotubes." Applied Physics Letters **74**(16): 2307.

Yang, R. T. (2000). "Hydrogen storage by alkali-doped carbon nanotubes–revisited." Carbon **38**(4): 623-626.

Yao, J. H., C. Shang, K. F. Aguey-Zinsou and Z. X. Guo (2007). "Desorption characteristics of mechanically and chemically modified LiNH2 and (LiNH2+LiH)." Journal of Alloys and Compounds **432**(1-2): 277-282.

Yoshida, A., H. Yoshimura, T. Terada, Y. Nakayama, H. Kuno, T. Miyao and S. Naito (2011). "Preparation of graphite supported Li–N–H hydrogen storage material from Li-graphite intercalation compound and their unique hydrogen release property." International Journal of Hydrogen Energy **36**(11): 6751-6755.

Züttel, A. (2003). "Materials for hydrogen storage." Materials Today **6**(9): 24-33.

Züttel, A. (2004). "Hydrogen storage methods." Naturwissenschaften **91**(4): 157-172.

Zaluska, A., L. Zaluski and J. O. Ström-Olsen (2001). "Structure, catalysis and atomic reactions on the nano-scale: a systematic approach to metal hydrides for hydrogen storage." Applied Physics A **72**(2): 157-165.

Zhang, Y. (2011). Hydrogen Storage In Nanostructrued Carbon-Based Materials. Doctor of Philosophy, University of Birmingham.

Zhang, Y., A. Bevan and D. Book (2012). "Hydrogen desorption behaviour of a ball-milled graphite - LiBH4 composite." MRS Online Proceedings Library **1386**: null-null.

Zhang, Y. and D. Book (2011). "Effect of Milling Conditions on the Purity of Hydrogen Desorbed from Ball-Milled Graphite." The Journal of Physical Chemistry C **115**(51): 25285-25289.

Zhang, Y. M., V.; Reed, D.; Walton, A.; Harris, I.R.; Book, D. (2009). Hydrogen storage properties of nanostructured graphite-based materials. Sustainable Power Generation and Supply, 2009. SUPERGEN '09. International Conference**:** 1-4.

Zuttel, A. (2004). "Hydrogen storage methods." Naturwissenschaften **91**(4): 157-172.